

①

ROBUST RATE CONTROL SYSTEM DESIGNS FOR A SUBMERSIBLE

by

Lawrence John Dreher

B.S., Rensselaer Polytechnic Institute  
(1977)

*N66314-70-A-0073*

SUBMITTED TO THE DEPARTMENTS OF OCEAN ENGINEERING  
AND MECHANICAL ENGINEERING IN PARTIAL FULFILLMENT  
OF THE REQUIREMENTS FOR THE DEGREE OF  
OCEAN ENGINEER AND MASTER OF SCIENCE IN  
MECHANICAL ENGINEERING

at the

MASSACHUSETTS INSTITUTE OF TECHNOLOGY

May 1984

© Lawrence John Dreher, 1984

Signature of Author *[Signature]*  
Departments of Ocean Engineering and  
Mechanical Engineering, May 11, 1984

Certified by \_\_\_\_\_  
Lena Valavani  
Thesis Supervisor

Certified by *Damon E. Cummings*  
Damon E. Cummings  
Thesis Co-Supervisor

Certified by \_\_\_\_\_  
Paul Houpt  
Thesis Co-Supervisor

Accepted by *A. Douglas Cornwell*  
Chairman, Ocean Engineering  
Departmental Graduate Committee

Accepted by *M. Rehman*  
Chairman,  
Mechanical Engineering Graduate Committee

This document has been approved  
for public release and sale; its  
distribution is unlimited.

DTIC  
ELECTE  
S AUG 24 1984 D  
E

**BEST**

**AVAILABLE**

**COPY**

ROBUST RATE CONTROL SYSTEM DESIGNS  
FOR A SUBMERSIBLE

by

Lawrence J. Dreher

Submitted to the Departments of Ocean Engineering and Mechanical Engineering in the Partial Fulfillment of the Requirements for the Degree of Ocean Engineer and Master of Science in Mechanical Engineering.

ABSTRACT

Two robust rate control system designs are carried out for a submersible (modeled by the NSRDC 2510 equations) in a turn using the Linear Quadratic Gaussian approach with Loop Transfer Recovery. Separate command channels allow the submersible to maneuver independently in the horizontal and vertical planes; the vehicle operator controls the bearing rate and depth rates through a joystick-like device. The fin configuration is the conventional cruciform stern without differential control.

The first compensator design, called the  $r - \theta$  controller in this thesis, directly controls two vehicle state variables: pitch ( $\theta$ ) and the vehicle angular velocity,  $r$ , about the z-axis. The other system, called the  $\dot{\psi} - \dot{z}$  controller, controls yaw (or heading) rate ( $\dot{\psi}$ ) and depth rate ( $\dot{z}$ ) directly. However, this design relies on linearized equations of yaw and depth rate to be employed by the compensator for state reconstruction.

A tool for Kalman Filter loop shaping is developed in which state variables are scaled to provide good loop shapes and then recovered to get controllers that are robust. Both controllers are compared on the basis of performance in a nonlinear simulation. A robustness comparison is also conducted.

Based on limited simulation data, this thesis concludes that the  $\dot{\psi} - \dot{z}$  controller provides better control of depth rate than the  $r - \theta$  controller. Bearing rate performance is essentially equal in both designs; however, the  $\dot{\psi} - \dot{z}$  controller appears less robust in certain frequency ranges.

THESIS SUPERVISOR: Dr. L. Valavani, Research Scientist,  
Laboratory for Information and Decision Systems

ACKNOWLEDGEMENTS

I would like to express my sincerest thanks to my thesis advisor, Lena Valavani, for her support and guidance through the summer months and into the school year. Special thanks to William Bonnice of The Charles Stark Draper Laboratory, Inc. who generously provided his own time to do much of the computer programming needed to accomplish this thesis.

The Charles Stark Draper Laboratory, Inc., has provided the facilities and financial resources required to complete this thesis. Publication of this thesis, however, does not constitute approval by the Charles Stark Draper Laboratory, Inc., of the findings or conclusions contained herein. It is published solely for the stimulation and exchange of ideas.

I hereby assign my copyright of this thesis to The Charles Stark Draper Laboratory, Inc., Cambridge, Massachusetts.

  
Lawrence J. Dreher

Permission is hereby granted by The Charles Stark Draper Laboratory, Inc., to the Massachusetts Institute of Technology and the United States Government and its agencies to reproduce and to distribute copies of this thesis document in whole or in part.

Accession For	
NTIS GRA&I	<input checked="" type="checkbox"/>
DTIC TAB	<input type="checkbox"/>
Unannounced	<input type="checkbox"/>
Justification	<i>form 50 per</i>
By	
Distribution/	
Availability Codes	
Dist	Avail and/or Special
<i>A-1</i>	



To Cindy, Jeffrey, and Alison.

## TABLE OF CONTENTS

<u>Chapter</u>		<u>Page</u>
	ABSTRACT.....	2
	ACKNOWLEDGMENT.....	3
	LIST OF FIGURES.....	7
	LIST OF TABLES.....	10
1	INTRODUCTION.....	11
	1.1 Background.....	11
	1.2 Outline of Thesis.....	12
2	THE SUBMARINE MODEL.....	14
	2.1 Introduction to Submersible Modeling.....	14
	2.2 The Nonlinear Computer Model.....	17
	2.3 Linear Modeling.....	19
	2.3.1 Equations of Motion.....	19
	2.3.2 Nominal Point Selection.....	21
	2.3.3 Output and Control Variable Formulation.....	22
	2.4 Dynamic Analysis.....	30
	2.5 Performance Specifications.....	34
3	CONTROL SYSTEM DESIGN METHODOLOGY.....	37
	3.1 Robustness.....	37
	3.1.1 Robustness Design Considerations.....	37
	3.1.2 LQG Compensator.....	40
	3.2 LQG Compensator.....	43
	3.3 Loop-Transfer Recovery.....	46
4	COMPENSATOR DESIGN PROCEDURE.....	49
	4.1 Augmented Dynamics.....	49
	4.2 Loop-Shaping Techniques.....	59
	4.3 Model Based Compensator Design.....	62

TABLE OF CONTENTS (Cont.)

<u>Chapter</u>		<u>Page</u>
5	MODEL BASED COMPENSATOR EVALUATION.....	79
	5.1 Compensator Design Implementation.....	79
	5.2 Evaluation of Output Variable Selection.....	79
	5.3 Robustness.....	93
	5.4 Gain Scheduling.....	95
	5.5 Other Notes.....	99
	5.6 Chapter Summary.....	100
6	CONCLUSIONS.....	101
	6.1 Summary.....	101
	6.2 Recommendations.....	102
 <u>Appendix A:</u>		
	A-1 Table of Dynamical Response Terms.....	106
	A-2 Nonlinear Equations of Motion.....	107
	A-3 Parametric Linearization.....	115
 <u>Appendix B:</u>		
	B-1 Nominal Design Point.....	131
	B-2 Augmented Linear System ( <u>A</u> , <u>B</u> Matrices).....	132
	B-3 $r - \theta$ Compensator Matrices.....	133
	B-4 $\dot{\psi} - \dot{z}$ Compensator Matrices.....	134
 <u>Appendix C:</u>		
	C-1 Nonlinear Simulation of $\dot{\psi} - \dot{z}$ Compensator for Various Commanded Inputs.....	136
	REFERENCES.....	103

## LIST OF FIGURES

### CHAPTER 2:

- Figure 2-1 Conventions showing positive directions of deflections, forces, velocities, and moments.
- 2-2 Linear open-loop plant model.
- 2-3 Reconstruction of actual and linearized depth rate for the submarine in a turn.
- 2-4 Reconstruction of actual and linearized turn rate, and the state "r" for the submarine in a turn.
- 2-5 Unscaled eigenvectors of  $\underline{A}$ .
- 2-6 Scaled eigenvector of  $\underline{A}$ .
- 2-7 Typical form of a wave spectrum containing swell (from Reference 6).

### CHAPTER 3:

- Figure 3-1 MIMO feedback configuration.
- 3-2 MIMO feedback configuration representing perturbation of the nominal system.
- 3-3 MIMO feedback configuration reflecting premultiplicative error at plant output.
- 3-4 The model based compensator in a feedback configuration.

### CHAPTER 4:

- Figure 4-1 Augmented dynamics placed in command variable channel of plant.
- 4-2 Stern plane command channel with augmented dynamics.
- 4-3 Rudder command channel with augmented dynamics.
- 4-4 Unaugmented open-loop plant;  $r - \theta$  system; singular values vs frequency.
- 4-5 Unaugmented open-loop plant;  $\dot{\psi} - \dot{z}$  system; singular values vs frequency.

- Figure 4-6 Augmented open-loop plant;  $r - \theta$  system; singular values vs frequency.
- 4-7 Augmented open-loop plant;  $\dot{\psi} - \dot{z}$  system; singular values vs frequency.
- 4-8 Shaped and unscaled filter open-loop transfer function;  $r - \theta$  system; singular values vs frequency.
- 4-9 Shaped and unscaled filter open-loop transfer function;  $\dot{\psi} - \dot{z}$  system; singular values vs frequency.
- 4-10 Scaled open-loop plane;  $r - \theta$  system; singular values vs frequency.
- 4-11 Scaled open-loop plant;  $\dot{\psi} - \dot{z}$  system; singular values vs frequency.
- 4-12 Shaped and scaled filter open-loop transfer function;  $r - \theta$  system; singular values vs frequency.
- 4-13 Shaped and scaled filter open-loop transfer function;  $\dot{\psi} - \dot{z}$  system; singular values vs frequency.
- 4-14 Kalman Filter loop transfer function;  $r - \theta$  system; singular values vs frequency.
- 4-15 Kalman Filter loop transfer function;  $\dot{\psi} - \dot{z}$  system; singular values vs frequency.
- 4-16 Loop-transfer recovery;  $r - \theta$  system; singular values vs frequency.
- 4-17 Loop-transfer recovery;  $\dot{\psi} - \dot{z}$  system; singular values vs frequency.
- 4-18 Kalman Filter return difference;  $r - \theta$  system; singular values vs frequency.
- 4-19 Kalman Filter inverse return difference;  $r - \theta$  system; singular values vs frequency.
- 4-20 Kalman filter return difference;  $\dot{\psi} - \dot{z}$  system; singular values vs frequency.
- 4-21 Kalman filter inverse return difference;  $\dot{\psi} - \dot{z}$  system; singular values vs frequency.

**CHAPTER 5:**

- Figure 5-1**      **Modification of the MBC feedback configuration due to scaling.**
- 5-2      Complete nonlinear simulation for  $\dot{\psi} - \dot{z}$  control system in vicinity of nominal point.
  - 5-3      Nonlinear simulation showing output error and response for  $r - \theta$  control system in vicinity of nominal point.
  - 5-4      Complete nonlinear simulation for  $\dot{\psi} - \dot{z}$  control system away from nominal point.
  - 5-5      Nonlinear simulation showing output error and response for  $r - \theta$  control system away from nominal point.
  - 5-6      Integral yaw error for commanded  $\psi$  rate after 100 seconds.
  - 5-7      Integral depth error for commanded  $\psi$  rate after 100 seconds.
  - 5-8      Output error response to various commanded inputs for  $r - \theta$  control system
  - 5-9      Steady-state rudder required to achieve commanded bearing rate.
  - 5-10     Inverse return difference of recovered transfer function and premultiplicative error;  $r - \theta$  system; singular values vs frequency.
  - 5-11     Inverse return difference of recovered transfer function and premultiplicative error;  $\dot{\psi} - \dot{z}$  system; singular values vs frequency.
  - 5-12     Schematic showing operating volume for determination of model robustness and acceptable performance near a nominal point.

## CHAPTER 1

### INTRODUCTION

#### 1.1 Background

The submarine operator's objective is to maneuver his vehicle freely in the ocean environment with respect to depth, heading, and speed. In some situations, such as transits and patrols, the operator's task is simplified to maintaining the submarine's depth, heading, and speed essentially constant. Such maneuvering requirements are easily accomplished by the crewmembers of the submersible. On the other hand, docking, turning, and performing evasive maneuvers to avoid navigation hazards or enemy torpedos are instances where the submarine's depth, heading, and speed may have to be varied suddenly. Obviously these maneuvers must be carried out safely and effectively. However, there are many environmental and design obstacles that inhibit the operator from fully controlling this process. These impediments include a cruciform stern without differential control; cross-coupling of the planes of motion (due primarily to the large sail area), variable hydrodynamic forces (vorticity, turbulence), and a limited ability to "see" the environment (no windows).

Largely through experience and familiarity with the vehicle dynamic response, the conning officer learns that certain rudder angle/pitch angle orders will result in a certain heading rate and depth rate for a given speed. Rules of thumb have been developed for ordering the appropriate amount of pitch angle to accomplish the required depth change and for an appropriate amount of stern plane angle to offset the vehicle's

tendency to dive in a turn. It is particularly difficult for the conning officer to simultaneously command the turn rate and pitch angle due to the interaction of complex dynamics. The operator's control task becomes increasingly difficult as the severity of the maneuver increases. One would therefore seek to eliminate much of the guesswork associated with performing these maneuvers by providing more substantial means of controlling the transient dynamics of the submarine.

It is the intent of this thesis to demonstrate a procedure for a truly multivariable control system design that would provide the operator with a means of achieving desired submarine motion in depth and heading through rate control. The multiple input - multiple output (MIMO) design methodologies based on the MIMO-LQG formulation of Stein and Doyle [1] will form the theoretical basis of this thesis. Specifically the novel MIMO-LQG/LTR approach proposed by Athans [2] for model based compensators will be followed in this controller design. Importantly, this methodology permits the design of dynamic compensators without the need for full state feedback. This will allow the development of a "robust" controller that is tolerant of modeling errors, nonlinearities, and noise.

## 1.2 Outline of Thesis

Chapter 2 first introduces submarine dynamics and develops the linear models that will be used for two different control system designs at 30 knots. The last section of the chapter will provide the desired controller design specifications to be adhered to in the remainder of this design.

In Chapter 3 the theory that provides the basis for the LQG-LTR process is introduced.

Chapter 4 is the design procedure chapter for the two controller designs. A method to produce consistent Kalman Filter loop shapes is developed.

In Chapter 5 the obtained designs are evaluated through computer simulation and comparisons are made.

Chapter 6 contains the summary and suggestions for further study.

## CHAPTER 2

### THE NONLINEAR SUBMARINE MODEL

#### 2.1 Introduction to Submersible Modeling

Submersible dynamics of motion and attitude can be described in a variety of coordinate systems. For the purpose of developing a model of submersible motion, the equations of motion are expressed in the body fixed axis because hydrodynamic forces and inertia are most readily computed in a ship reference frame. From the aspect of ship guidance and control, on the other hand, it may be desirable to describe motion, such as vehicle course and depth, in terms of an earth reference frame.

General dynamical equations have been developed for the description of an vehicle motion. These represent equalities of Newtonian force and moment expressions, on the left hand side, and the so called dynamical response terms on the right hand side:

$$\left. \begin{array}{l} \vec{F} \\ \vec{M} \end{array} \right\} = f \text{ (dynamical response terms)} \quad (2-1)$$

The general form of the force expression (Newton) is:

$$\vec{F} = \frac{d}{dt} (\text{momentum}) = \frac{d}{dt} (m\vec{U}_G)$$

where

$$\vec{U}_G = \vec{i}u + \vec{j}v + \vec{k}w$$

and the moment expression is

$$\vec{M}_G = \frac{d}{dt} (\text{angular momentum}) = \frac{d}{dt} (I\vec{\Omega})_G$$

where

$$\vec{\Omega} = \vec{i}p + \vec{j}q + \vec{k}r$$

(The definitions of  $u$ ,  $v$ ,  $w$ ,  $p$ ,  $q$ , and  $r$  are found in Table 2-1).

The subscript  $G$  indicates the origin to coincide with a body-fixed coordinate system located at the vehicle center of gravity. However, the reference point is seldom taken there since the center of gravity moves with shifting weights inside the vehicle. Instead, the coordinate system is generally taken about the submersible center of buoyancy, and so provides a useful location for hydrodynamic estimates. This point is a function of vehicle geometry and is therefore fixed. The left hand side equations become somewhat more involved due to this coordinate system transformation and will not be discussed further. Details of these terms and simplifications commonly used for ocean vehicle dynamics can be found in reference [3].

The dynamical response terms of the right hand side of Eq. (2-1) are presented in Appendix A. These terms express the external forces and moments exerted on the vehicle by hydrodynamic, control surface, propulsion, and other effects.

The force and moment equalities of Eq. (2-1) describe the six possible degrees of freedom of the submersible. The three forces are in the axial, lateral, and normal directions, which give rise to motions

Table 2-1. Definitions of submarine states and controls.

Submarine States

<u>State</u>	<u>Definition</u>	<u>Units</u>
u	= Component of $\vec{U}$ in direction of x axis	(ft/s)
v	= Component of $\vec{U}$ in direction of y axis	(ft/s)
w	= Component of $\vec{U}$ in direction of z axis	(ft/s)
p	= Component of $\vec{\Omega}$ about x axis	(rad/s)
q	= Component of $\vec{\Omega}$ about y axis	(rad/s)
r	= Component of $\vec{\Omega}$ about z axis	(rad/s)
$\phi$	= Angular rotation (roll) about the x axis	(radians)
$\theta$	= Angular rotation (pitch) about the y axis	(radians)

Submarine Controls

- $\delta r$ : deflection of rudder
- $\delta s$ : deflection of stern plane
- $\delta b$ : deflection of sail planes
- RPS: shaft revolutions per second

of surge, sway, and heave respectively. The three moment equations produce moments and motion of roll, pitch, and yaw. Figure 2-1 shows the positive directions of forces, moments, motions, and control surface deflections.

## 2.2 The Nonlinear Computer Model

The nonlinear model used for this design was derived from the original NSRDC 2510 document "Standard Equations of Motion for Submarine Simulation" [4]. These equations have since been improved to include crossflow drag and vortex contributions. This model is installed on the computer system at the Charles Stark Draper Laboratories. The nonlinear model used in this thesis consists of 8 differential equations to describe the submarine dynamics. The six equations derived from the force and moment equalities account for the states  $u$ ,  $v$ ,  $w$ ,  $p$ ,  $q$ , and  $r$ . The dependence of these states on hydrostatic restoring forces about the pitch and roll axis and their kinematic relations result in two additional states,  $\phi$  and  $\theta$ . The definitions of these states are listed in Table 2-1.

At this point, it will suffice to state that ship motion in open water is not sensitive to heading angle; on the other hand, the dynamics of a submersible are affected by changes in buoyant forces brought about by moderate depth excursions. These forces were not accounted for in the submarine model and, hence, depth is not included as a state in the system equations. By choice, propulsion plant dynamics were excluded in this model; the resulting propeller dynamics in an actual submarine vary, depending on the operating procedure of engineering plant personnel and would be difficult to model. Moreover, the model in its current version does not include either the actuator dynamics, or the actual angle rate limits of the control surfaces. Due to the importance of actuator dynamics on the control of actual submersibles, they will be considered as part of the augmented plant dynamics for this design in Section 4.1.

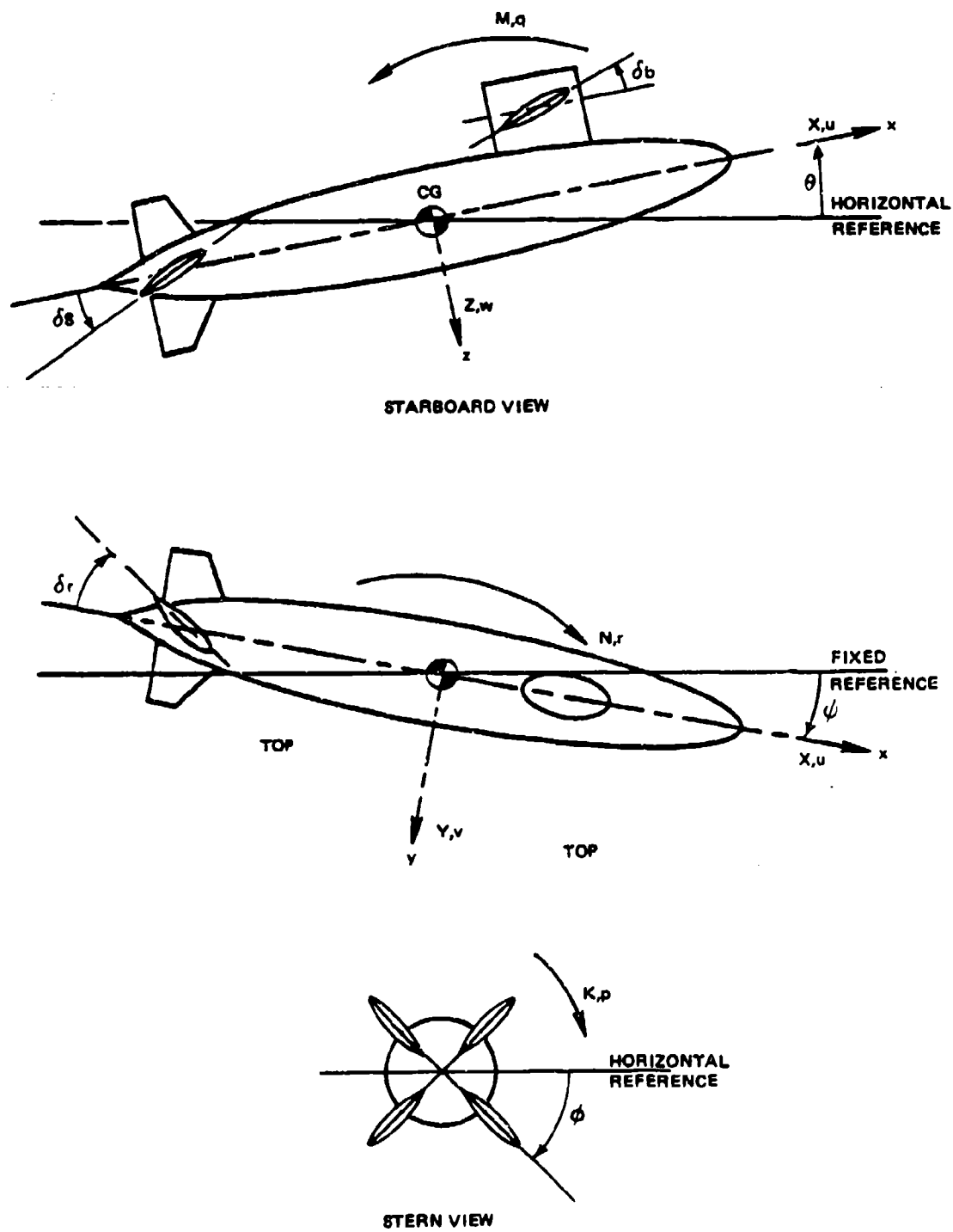


Figure 2.1. Conventions showing positive directions of deflections, forces, velocities, and moments.

The resulting eight nonlinear equations as used in the computer simulation with the definitions of the hydrodynamic coefficients are given in Appendix A. These coefficients are approximated by direct measurement on a full scale or model submarine, or analytically. The accuracy of the dynamic response of the model is governed to a large extent by the accuracy of these hydrodynamic coefficients. Additionally, some forces have yet to be modeled mathematically, and other effects such as vortex shedding and separation effects are not possible to include in a linear model and are most likely the weakest point in the design model.

## 2.3 Linear Modeling

### 2.3.1 Equations of Motion

The controller design procedure begins with the expression of the equation of motion in linear time invariant state space form. The nonlinear, multivariable system that represents the submarine is described by:

$$\frac{d}{dt} \underline{x}(t) = f(\underline{x}(t), \underline{u}(t)) \quad (2-2)$$

$$\underline{y}(t) = g(\underline{x}(t)) \quad (2-3)$$

where

$\underline{x}$  is the state vector

$\underline{u}$  is the control input vector

$\underline{y}$  is the output vector

These nonlinear equations can be linearized through a Taylor series expansion in the vicinity of a nominal point (ideally where  $\frac{d}{dt} (\underline{x}(t)) = 0$ ) for small deviations of  $\underline{u}(t)$  and  $\underline{x}(t)$  from the nominal state  $\underline{u}_0, \underline{x}_0$ . From Eq. (2-2) and (2-3) the linearized dynamics are derived as:

$$\Delta \dot{\underline{x}}(t) \approx \underline{A} \Delta \underline{x}(t) + \underline{B} \Delta \underline{u}(t) \quad (2-4)$$

$$\Delta \underline{y}(t) \approx \underline{C} \Delta \underline{x}(t) \quad (2-5)$$

where

$$\Delta \underline{x}(t) = \underline{x}(t) - \underline{x}_0$$

$$\Delta \underline{u}(t) = \underline{u}(t) - \underline{u}_0 \quad (2-6)$$

and

$$\dot{\underline{x}}_0 \Big|_{\substack{\underline{x}=\underline{x}_0 \\ \underline{u}=\underline{u}_0}} = f(\underline{x}_0(t), \underline{u}_0(t))$$

$$\underline{y}_0(t) = g(\underline{x}_0(t))$$

$$\underline{A} = \frac{\partial f(\underline{x}, \underline{u})}{\partial \underline{x}} \Big|_{\substack{\underline{x}=\underline{x}_0 \\ \underline{u}=\underline{u}_0}} \quad (2-7)$$

$$\underline{B} = \frac{\partial f(\underline{x}, \underline{u})}{\partial \underline{u}} \Big|_{\substack{\underline{x}=\underline{x}_0 \\ \underline{u}=\underline{u}_0}} \quad (2-8)$$

$$\underline{C} = \frac{\partial g(\underline{x})}{\partial \underline{x}} \Big|_{\underline{x}=\underline{x}_0} \quad (2-9)$$

The parametric linearization of the nonlinear equations was accomplished analytically in the interest of accuracy for obtaining good linear models, given some of the modeling drawbacks already mentioned. Details are given in Appendix A.

### 2.3.2 Nominal Point Selection

A most important step in the design process is to select a linear model that best describes the dynamics of the submarine over the widest possible range of operating conditions. The control system to be designed in this study will use as command variables and, therefore, control, in some manner, depth and heading rates. The nominal point chosen for the design, then, will be taken about a submarine in a level turn (i.e., pitch angle, or  $\theta$  is zero), since this attitude of a submarine is the most likely operating condition.

All four actuator variables; RPS,  $\delta r$ ,  $\delta b$ , and  $\delta s$  must be selected to define the particular nominal operating point. The shaft RPS will remain at that required for 30 knots in straight ahead motion. The rudder deflection,  $\delta r$ , can be set at arbitrary angles to cause the submarine to turn at different rates. A rudder deflection of (+) 2 degrees was selected for this nominal point design.\*

The next condition involves the use of the stern and bow planes that result in zero pitch while turning. For reasons outlined in the next subsection, the sail planes will be "locked" at a zero deflection angle for this model. With this constraint, the stern planes were perturbed on the nonlinear computer model in order to achieve zero pitch angle. The four actuator variables chosen result in the nominal design point of Appendix B.

---

\*The linearization about (-) 2 degrees of rudder would yield different system matrices than that obtained about (+) 2 degrees of rudder; this is primarily attributed to dynamic asymmetry caused by rotation of the vehicle propellor (torque reaction and flow).

### 2.3.3 Output and Control Variable Formulations

In this subsection one will gain insight into the appropriate selection of the output and control variables to accomplish the proposed control design. This will eventually lead to the development, in parallel, of two controller designs based on two sets of output variables. There will be some freedom in the choice of control (actuator) variables as well, but their selection will be based on a rather casual approach.

#### a. Control Methodology Constraints

The Loop Transfer Recovery method for the class of Model Based Compensators, apart from its advantages, places a very important requirement on the design freedom at a very early stage. It will be seen in later sections that the mathematics (singular values et al.) require a square system, that is, the number of control inputs be equal to the number of output controlled variables. Stated more precisely:

$$\underline{y}(t) = \epsilon R^m$$

$$\underline{u}(t) = \epsilon R^p$$

where R indicates the dimension space of the system. So the requirement is

$$p = m \quad (2-10)$$

and with three independent control surfaces available

$$p \leq 3$$

Note that RPS is not a control variable in the present model.

### b. Control Input Selection

It was proposed to have two "y" outputs for the operator to control through a "joystick-like" device. From the requirement for a square system  $p = m = 2$ . How, then, are the two independent control inputs selected? Clearly one needs a rudder to produce motion in the horizontal plane. For motion in the vertical plane, however, there are two control surfaces available, the stern and sail planes, which provide a redundant control capability. The stern planes provide about three and a half times more force to affect  $q$  than the sail planes for the same deflection angle. This can be seen by comparing entries  $B(5, 1)$  and  $B(5, 2)$  of the B matrix in Table 2.2. Realizing the importance of controlling the stern planes, there are two options concerning the use of the sail planes:

- (1) Model the submersible with the sail planes locked at some angle,  $\delta b_0$ , or;
- (2) Model the submersible so that a linear relationship exists between deflection of the stern and sail planes.

In either method, there is effectively only one independent control surface for vertical motion control.

Table 2-2. Model based B matrix.

<u>State</u>	$\delta s$	$\delta b$	$\delta r$
u	0.29053E-01	-0.15339E-02	-0.10980E+00
v	0.00000E+00	0.00000E+00	0.21864E+01
w	-0.18604E+01	-0.13578E+01	-0.27856E-05
p	0.00000E+00	0.00000E+00	0.39980E-01
q	-0.45053E-01	0.13042E-01	0.91875E-06
$\tau$	0.00000E+00	0.00000E+00	-0.55462E-01
$\phi$	0.00000E+00	0.00000E+00	0.00000E+00
$\theta$	0.00000E+00	0.00000E+00	0.00000E+00

In the first option above, a constant deflection other than  $\delta b = 0$  may not prove to be ideal if the controller is to operate at arbitrary pitch conditions in a turn. Additionally, if several nominal points were selected for gain scheduling, then, when the controller shifted from one set of gains to another, a step change in  $\delta b$  may be required. This change could lead to other problems and possible instabilities.

In this design,  $k$  has consequently been chosen to equal zero so that  $\delta b = 0$ . This is consistent with current fleet submarine practice of generally not using the sail planes to accomplish high-speed maneuvers. The effect of  $k$  on robustness and performance will not be addressed in this thesis.

### c. Output Variable Selection

Ideally one would have the present systems directly control the bearing rate,  $\dot{\psi}$ , and depth rate  $\dot{z}$ . The expressions:

$$\dot{\psi} = (r \cos \phi + q \sin \theta) / \cos \theta \quad (2-13)$$

and

$$\dot{z} = -u \sin \theta + v \cos \theta \sin \phi + w \cos \theta \cos \phi \quad (2-14)$$

are nonlinear functions of the state variables.

To proceed further, the open-loop time domain linear model of the plant in Figure 2-2 is introduced. Here the output variable,  $y(t)$ , is defined as  $y(t) = \underline{C}x(t)$ . The  $\underline{C}$  matrix will be an important parameter in the design of the Model Based Compensator. The  $\underline{C}$  matrix is a constant matrix which represents the linearization of (2-13) and (2-14) using (2-9). Letting  $y_1 = \dot{\psi}$  and  $y_2 = \dot{z}$ , the coefficients of the  $\underline{C}$  matrix are given in Table 2-3. The matrix indices (1, 2, ..., 8) represent states  $u, v, w, p, q, r, \phi, \theta$ , respectively, the subscript "o" indicating the (value of the) state at the nominal point.

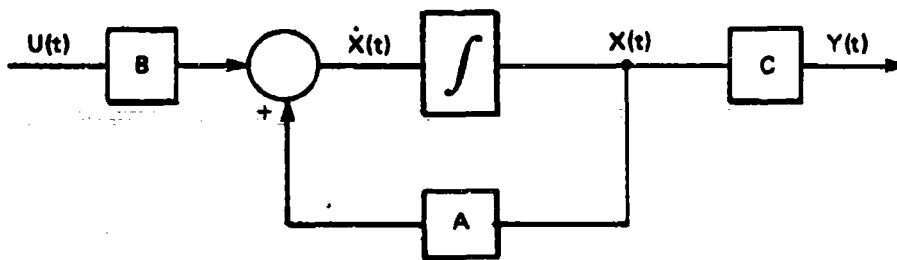


Figure 2-2. Linear open-loop plant model.

Table 2-3. Linearization of outputs  $\dot{\psi}$  and  $\dot{z}$  to obtain the  $\underline{C}$  matrix.

$$C(1, 5) = \frac{\sin \phi_0}{\cos \theta_0}$$

$$C(1, 6) = \frac{\cos \phi_0}{\cos \theta_0}$$

$$C(1, 7) = \frac{-r_0 \sin \phi_0 + q_0 \cos \theta_0}{\cos \theta_0}$$

$$C(1, 8) = \frac{(r_0 \cos \phi_0 + q_0 \cos \phi_0) + \tan \theta_0}{\cos \theta_0}$$

$$C(2, 1) = -\sin \theta_0$$

$$C(2, 2) = \cos \theta_0 \sin \phi_0$$

$$C(2, 3) = \cos \phi_0 \cos \theta_0$$

$$C(2, 7) = v_0 \cos \theta_0 \cos \phi_0 - w_0 \cos \theta_0 \sin \phi_0$$

$$C(2, 8) = -u_0 \cos \theta_0 - v_0 \sin \theta_0 \sin \phi_0 - w_0 \sin \theta_0 \cos \phi_0$$

To determine how accurately  $\underline{y}(t) = \underline{C}\underline{x}(t)$  represents the actual observed outputs  $\dot{\psi}$  and  $\dot{z}$ , the author has taken all states of a maneuver of a submarine in a turn and reconstructed the linear and nonlinear (actual) representations of  $\dot{\psi}(t)$  and  $\dot{z}(t)$ . These results are presented in Figures 2-3 and 2-4. It is seen that  $\dot{z}_{\text{linear}}$  becomes 50% of  $\dot{z}_{\text{actual}}$ . It is found that the relative deviation between the linear and actual  $z$  decreases as  $\dot{z}_{\text{actual}}$  increases in magnitude.  $\dot{\psi}_{\text{actual}}$  and  $\dot{\psi}_{\text{linear}}$  are nearly identical over the full maneuver. The control design based on these linearized states will be referred to in the remainder of this study as the  $\dot{\psi} - \dot{z}$  controller.

An alternative to a  $\underline{C}$  matrix which is dependent on the vehicle states at the nominal point is to choose  $\underline{C}$  such that its entries are independent constants, but that would still represent rates that are desirable to control.

Referring to Figure 2-4 once more one can see that such a term for  $\dot{\psi}$  exists. The state  $r$  has, throughout this maneuver, remained within 4% of  $\dot{\psi}_{\text{actual}}$ . This is made clear by referring to (2-13) and noting that for nearly all turning maneuvers,  $r \gg q$  and the  $\cos \theta \approx 1$ . To control depth rate, one can revert back to current submersible operational practice of commanding pitch angle. This follows from (2-14) where  $u \gg v, w$  so that  $z \approx -u \cdot \sin \theta \approx -u\theta$ . Since forward velocity is known,  $\dot{z}$  is proportional to  $\dot{\theta}$  so  $\underline{C}$  becomes:

$$C(1, 6) = 1$$

$$C(1, 8) = 1$$

The designed based on this  $\underline{C}$  matrix will be known as the  $r - \theta$  controller.

For implementation purposes the exact values of  $\dot{\psi}$  and  $\dot{z}$  are always available (observable) for both the nonlinear models and the actual submersible. Observer devices to measure  $z$  include depth gauge measurement. For more accurate designs with less environmental noise, gimballed accelerometers could be integrated to provide  $\dot{z}$ . The installed rate gyros used

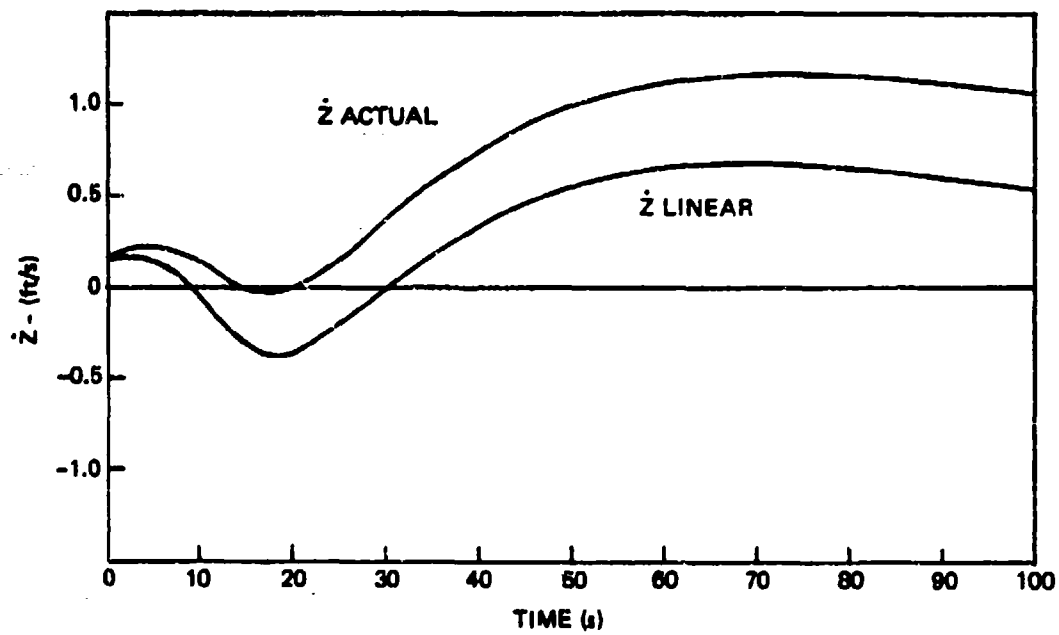


Figure 2-3. Reconstruction of actual and linearized depth rate for the submarine in a turn.

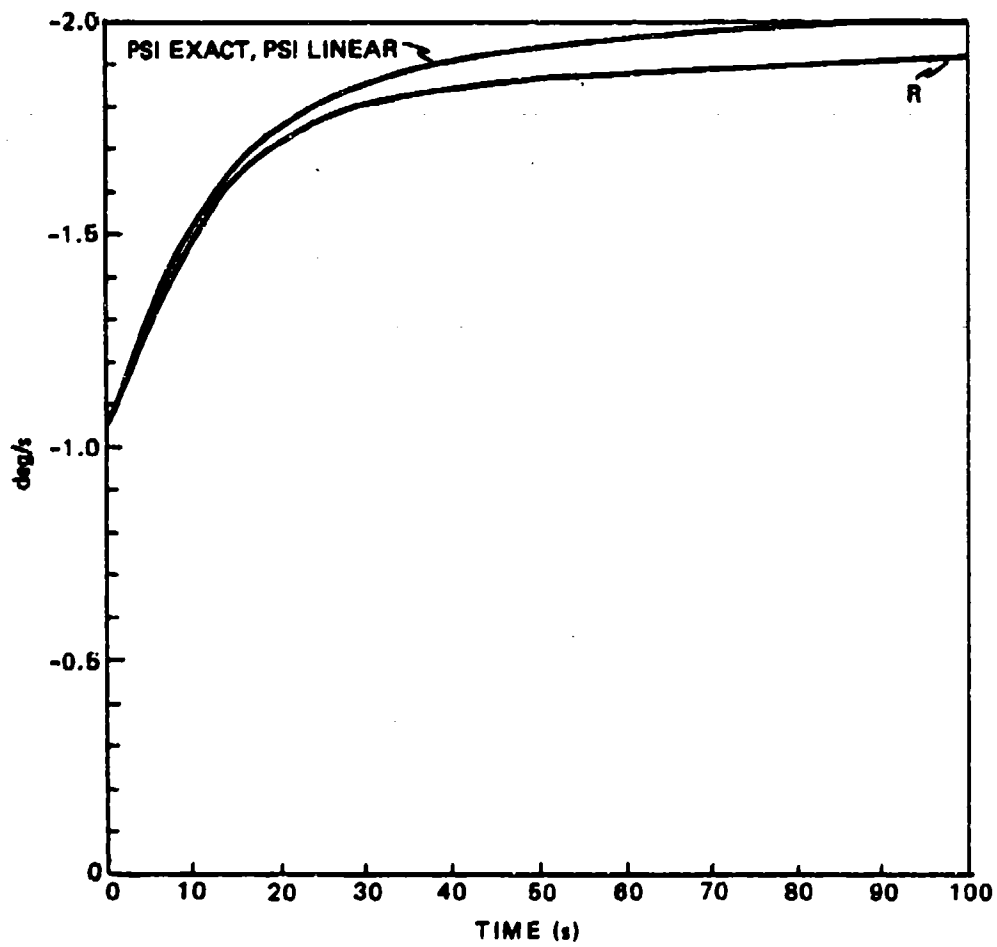


Figure 2.4. Reconstruction of actual and linearized turn rate, and the state "r" for the submarine in a turn.

for fire control system can measure the submarine's true heading rate,  $\dot{\psi}$ , regardless of the vehicle attitude. The  $r$  and  $\theta$  states can be measured with similar ease.

#### 2.4 Dynamic Analysis

In this subsection the open-loop poles (eigenvalues) and eigenvectors will be calculated, and the conditions for controllability and observability of linear control systems will be presented.

The eigenvalues of the A matrix resulting from the linearization are shown in Table 2-4. The corresponding normalized eigenvectors are shown in Figure 2-5. It would appear that all modes are dominated by the velocity states  $u$ ,  $v$ , and  $w$ . A different picture results when the values of the eigenvectors involving angle and angle rate states are scaled from radians to degrees and the velocities  $u$ ,  $v$ , and  $w$  remain in feet/second. Although the choice of units was somewhat arbitrary, the scaled and normalized eigenvectors of Figure 2-6 seem to provide a clearer picture of the state contribution to the system modes. The complex pole,  $-0.19 \pm 0.32i$ , is associated with the natural roll behavior of the submarine. The slowest pole,  $-0.013$ , is primarily a pitch mode. The zeroes of the system will be discussed in Chapter 4, after the addition of augmented dynamics.

Table 2-4. Complex eigenvalues of A.

-0.190874E+00	0.320975 I
-0.190874E+00	-0.320975 I
-0.487435E+00	0.000000 I
-0.443184E+00	0.000000 I
-0.978560E-01	0.000000 I
-0.432890E-01	0.000000 I
-0.591569E-01	0.000000 I
-0.133116E-01	0.000000 I

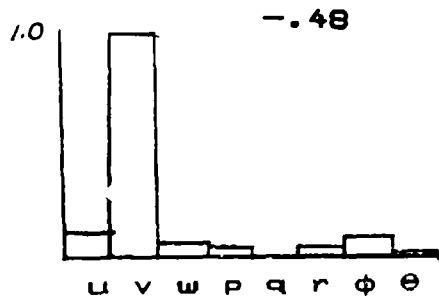
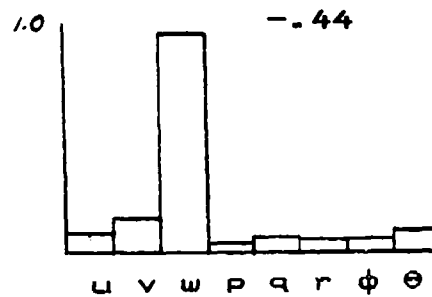
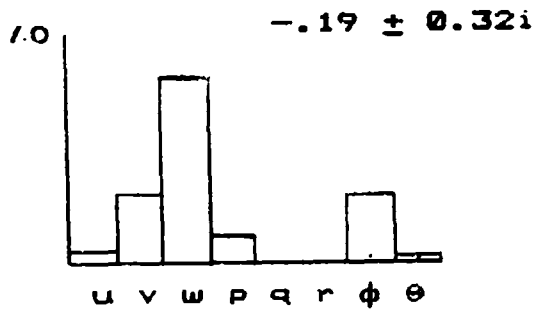
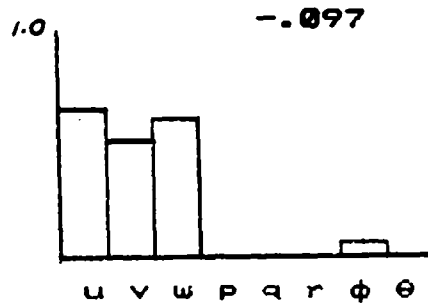
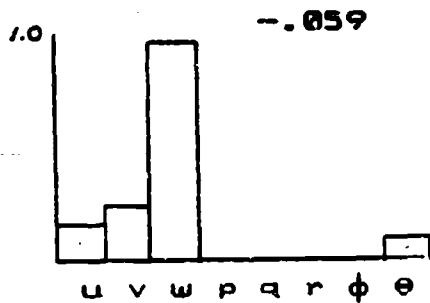
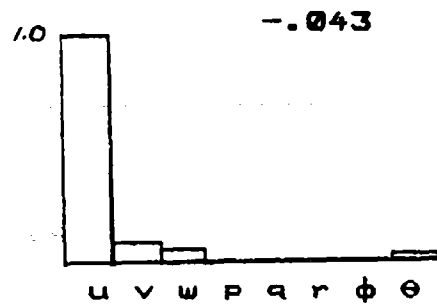
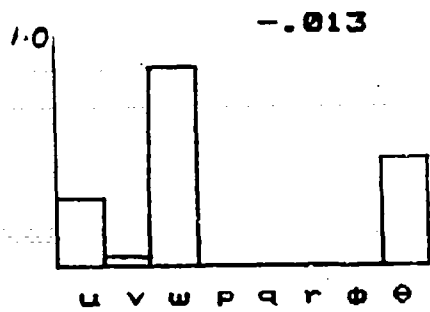


Figure 2-5. Unscaled eigenvectors of  $[A]$ .

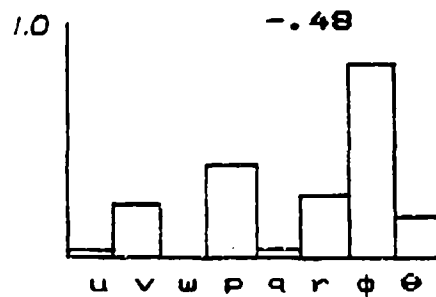
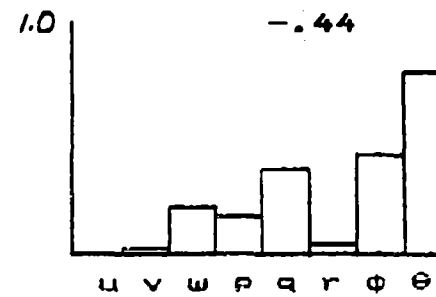
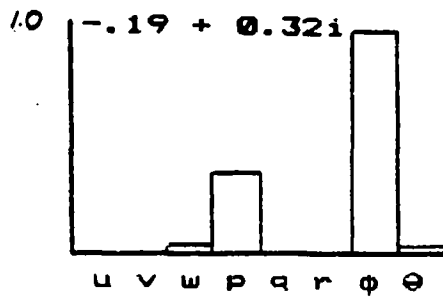
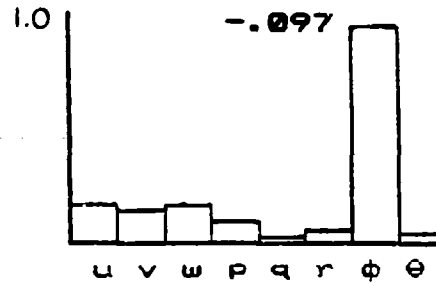
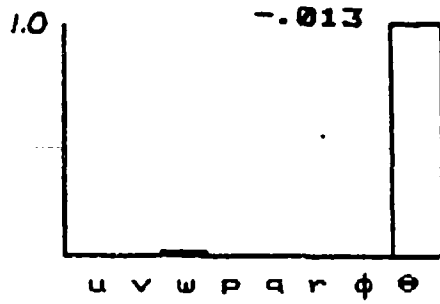
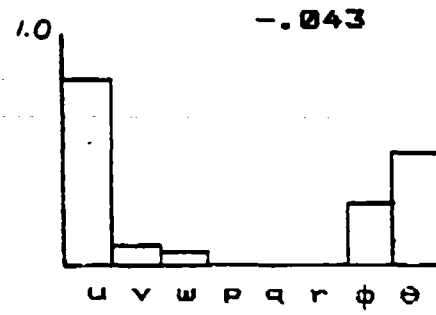
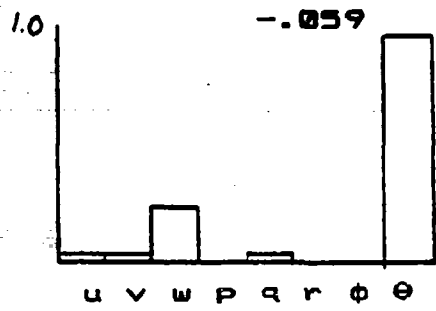


Figure 2-6. Scaled eigenvectors of  $[A]$ .

Controllability and observability properties need to be established to proceed further with the control system design. Controllability is ensured only if the matrix

$$[\underline{B}, \underline{A}\underline{B}, \dots, \underline{A}^{n-1}\underline{B}] \quad (2-15)$$

has rank  $n$ . Similarly, observability is guaranteed if the matrix

$$\begin{bmatrix} \underline{C} \\ \underline{C}\underline{A} \\ \cdot \\ \cdot \\ \underline{C}\underline{A}^{n-1} \end{bmatrix} \quad (2-16)$$

has rank  $n$ .

A simpler, but more conservative method than (2-15) and (2-16) above will be used to establish controllability and observability. Since eigenvalues of  $\underline{A}$  are distinct and nonzero, one can find the complex modal matrix,  $\underline{T}$ , whose columns are the distinct eigenvectors,  $\underline{v}_i$ . For any set of scalars  $c_i$  (not all zero):

$$\sum_i c_i \underline{v}_i = 0$$

implies that  $\underline{T}$  is a nonsingular matrix. Then the state equation can be written in the modal domain. [5]:

$$\frac{d}{dt} \underline{x}^* = \underline{T}^{-1} \underline{A} \underline{T} \underline{x}^* + \underline{T}^{-1} \underline{B} u$$

$$\underline{y} = \underline{C} \underline{T} \underline{x}^*$$

The controllability and observability conditions are then more than satisfied by observing that the real parts of the columns of  $\underline{T}^{-1}\underline{B}$  and the rows  $\underline{C}\underline{T}$  have no zeros. This was found to be the case for both the  $x - \theta$  and  $z - \dot{\psi}$  systems.

## 2.5 Performance Specifications

Performance specifications outlined in this section are not all encompassing and may not coincide with established Navy specifications for submersible control. The performance requirements as stated here are mainly driven by the intuitive engineering approach to obtain good command following, speed of response, robustness, and disturbance rejection with due respect to the natural dynamics of the vehicle as they emerge from the available model. These performance requirements (guidelines) will be accomplished through loopshaping techniques to be discussed in Chapter 3.

Since there are no natural integrator states (the  $8 \times 8 \underline{A}$  matrix is nonsingular), elimination of steady-state error to step inputs is not possible. Good command following and elimination of steady-state errors will be obtained through the use of integrators in the command variable channel. Although an actual rate control system may also experience ramp-like commands from the "joy-stick", the command inputs here are closer to being a step due to the large time constants of the system. Therefore, the system described in this thesis will not be designed to meet type-2 specifications.

The open-loop dynamic simulation demonstrates that achievable vehicle settling times due to deflections of control surfaces are a function of the vehicle speed. For a submersible at a speed of 30 knots, settling time of 50 - 60 seconds are achievable. When settling is defined to occur in 4 or 5 time constants, the resulting minimum bandwidth requirements for crossover are 0.07 to 0.1 radians/second. From the performance aspect it is desirable to have all channels crossover at roughly the same frequency.

On the high frequency side, one must be able to reject noise and possible modeling errors. Noise sources generally originate from the environment (true sensor readings) or from the sensor itself. Sensor noise typically comes at a higher frequency than the system bandwidth and should not affect ship dynamics since ship eigenvalues will typically lie in the lower frequency band. It is desired that the ship actuators do not respond to normal environmental disturbances that may cause unnecessary actuator motion. Of concern here is the effect of the submersible operating close to the surface, but not so close as to be in the danger of broaching, and experiencing excitations of surface waves. Based on Figure 2-7 [6], it is apparent that a typical wave spectrum has a frequency range between 0.2 and 2 radians/second. The excitation or driving frequency the submarine experiences will be

$$\omega_e = \omega + ku \cos(\phi)$$

where

- $\omega_e$  = frequency of encounter
- $\omega$  = wave spectrum frequency
- $k = \omega^2/g$  = wave number in deep water
- $u$  = ship forward velocity
- $\phi$  = ship head relative to sea direction

then, based on an estimated max ship speed of 35 knots (60 fps):

$$\omega_{e \max} = 9.5 \text{ rad/s (in head seas)}$$

$$\omega_{e \min} = 0.13 \text{ rad/s (in following seas)}$$

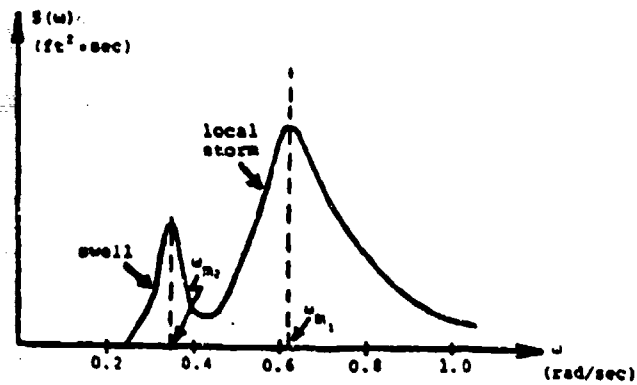


Figure 2-7. Typical form of a wave spectrum containing swell (from Ref. [6]).

and therefore at any vehicle speed, 35 knots or less, all other ship headings relative to the sea will be contained within  $\omega_e \text{ max} > \omega_e > \omega_e \text{ min}$ .

The proposed controller will, then, be able to meet these minimum criteria with the suggested bandwidth, at least in the region where linear behavior dominates the vehicle dynamics.

## CHAPTER 3

### CONTROL SYSTEM DESIGN METHODOLOGY

#### 3.1 Robustness

##### 3.1.1 Robustness Design Considerations

Control system design frequently involves the tradeoff of realizing high performance while preserving good command following, disturbance rejection, and system stability. The achievement of high performance is pointless if the control system becomes unstable as a result. This is particularly important in the present design. Overall system instability could cause the submersible, in some instances, to exceed its safe operating depth or ground itself, resulting in the loss of the submarine and its crew. The multivariable methods used to assure stability and robustness will be reviewed next.

Singular value analysis has evolved as a reliable method to evaluate system stability and robustness in the presence of unstructured uncertainty. The singular values of an  $(n \times n)$  complex matrix  $\underline{A}$  derived from the spectral norm  $\|\underline{A}\|_2$  are defined by:

$$\sigma_i = \sqrt{\lambda_i(\underline{A}^H \underline{A})} \quad i = 1, 2, \dots, n$$

where

$\underline{A}^H$  is the complex conjugate transpose of  $\underline{A}$

$\lambda_i$  is the  $i$ th eigenvalue operator

in modeling the system dynamics and therefore will be used in this model. Furthermore, a premultiplicative error of the loop transfer function will be defined to reflect errors at the plant output, as shown in Figure 3-3. In this instance

$$\underline{L}(s) = \underline{I} + \underline{E}(s)$$

so that the premultiplicative error,  $\underline{E}_{\text{pre}}(s)$ , is found to be

$$\underline{E}_{\text{pre}}(s) = [\tilde{\underline{G}}(s) - \underline{G}(s)]\underline{G}^{-1}(s) \quad (3-1)$$

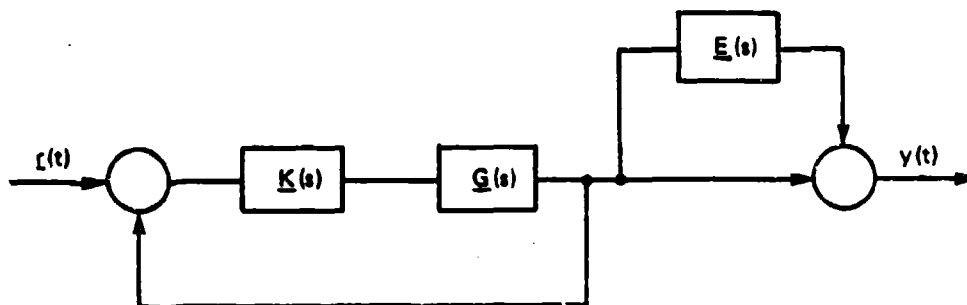


Figure 3-3. MIMO feedback configuration reflecting premultiplicative error at plant output.

From the Fundamental Robustness Theorem and the Theorem for Robustness for Multiplicative Errors (see Lahtomaki [7]), for guaranteed stability, the following inequality must hold:

$$\sigma_{\max}[\underline{E}_{\text{pre}}(j\omega)] \leq \sigma_{\min}[\underline{I} + (\underline{G}(j\omega)\underline{K}(j\omega))^{-1}] \quad (3-2)$$

If the inequality (3-2) above is not true, it does not necessarily imply the system must be unstable. Singular value analysis does not take into account the actual direction of the perturbation matrix that may cause a system to become singular; hence the system may actually be more robust than singular value analysis may indicate. Therefore the inequality (3-2) above is conservative.

### 3.1.2 Scaling

Scaling is a method of weighting the physical units of a system, through an appropriate transformation, so that the numerical values of the variables become equally significant. Scaling and its effect in designing robust multivariable control systems has been recently discussed by Kappos [9] and Boettcher [8]. Apparently, scaling does in fact change the singular value magnitudes, but it may not necessarily change the robustness of the system [8]. Ostensibly, not all effects of scaling are understood at present.

A systematic method does not yet exist to obtain optimal scaling. Kappos [9] selects a scaling matrix based on the expected nominal departure (error) of the output. Kwakernaack [10], although not specifically addressing the robustness issue, similarly suggests weighting the states by their tolerable error, i.e., a deviation of 10 ft/s in velocity may be as bad as a deviation of 0.2 radians in pitch, and then base the weighting on the ratio of the tolerable errors. In this thesis the author presents a method that allows the system to scale itself through loop shaping techniques. This procedure will be presented in Chapter 4.

A scaling transformation to transform state vectors must be diagonal and positive to preserve the system eigenvalues. Briefly, if  $\underline{u}$ ,  $\underline{y}$ , and  $\underline{x}$  are the original state vectors, and  $\underline{u}'$ ,  $\underline{y}'$ , and  $\underline{x}'$  are a set of scaled vectors, then:

$$\begin{aligned}
 \underline{u} &= \underline{S}_u \underline{u}' \\
 \underline{y} &= \underline{S}_y \underline{y}' \\
 \underline{x} &= \underline{S}_x \underline{x}'
 \end{aligned}
 \tag{3-3}$$

consequently for a system of the original form:

$$\begin{aligned}
 \dot{\underline{x}} &= \underline{A}\underline{x} + \underline{B}\underline{u} \\
 \underline{y} &= \underline{C}\underline{x}
 \end{aligned}
 \tag{3-4}$$

the transformed matrices become

$$\begin{aligned}
 \underline{A}' &= \underline{S}_x^{-1} \underline{A} \underline{S}_x \\
 \underline{B}' &= \underline{S}_x^{-1} \underline{C} \underline{S}_y \\
 \underline{C}' &= \underline{S}_y^{-1} \underline{C} \underline{S}_x
 \end{aligned}
 \tag{3-5}$$

Scaling directly affects transfer functions as well. Defining the open-loop transfer function,  $\underline{G}_{OL}(s)$  of Figure 2-2 as

$$\underline{G}_{OL}(s) = \underline{C}(s\underline{I} - \underline{A})^{-1} \underline{B}
 \tag{3-6}$$

it can be shown straightforwardly that the scaled transfer function becomes

$$\underline{G}'(s) = \underline{S}_y^{-1} \underline{G}(s) \underline{S}_u
 \tag{3-7}$$

Similarly, scaling  $\underline{E}_{pre}(s)$ , the premultiplicative error defined in Eq. (3-1), one obtains

$$\underline{E}'(s) = \underline{S}_y^{-1} \underline{E}(s) \underline{S}_y \quad (3-8)$$

Finally, a useful property of the scaling transformation will be developed next. Take the special case of Eq. (3-7) where  $\underline{S}_u^{-1}$  is the identity matrix so that

$$\underline{G}'(s) = \underline{S}_y^{-1} \underline{G}(s) \quad (3-9)$$

By taking the complex conjugate transpose of Eq. (3-9) above:

$$\underline{G}'^H(s) = \underline{G}^H(s) \underline{S}_y^{-1H} \quad (3-10)$$

From Eq. (3-9) and (3-10) then

$$\underline{G}'(s) \underline{G}'^H(s) = \underline{S}_y^{-1} \underline{G}(s) \underline{G}^H(s) \underline{S}_y^{-1H} \quad (3-11)$$

and, applying the two-norm implies

$$\|\underline{G}'(s)\|_2^2 = \|\underline{S}_y^{-1} \underline{G}(s)\|_2^2 \quad (3-12)$$

so that

$$\|\underline{G}'(s)\|_2 = \|\underline{S}_y^{-1} \underline{G}(s)\|_2 \quad (3-13)$$

Note that  $S_y^{-1}$  is not a function of  $s$ . Through matrix multiplication, the diagonal entries of  $S_1^{-1} \dots S_n^{-1}$  of the matrix  $S_y^{-1}$  independently multiply the rows of  $\underline{G}(s)$ . Knowing the following relation to hold

$$||\alpha A|| = |\alpha| \cdot ||\underline{A}||$$

where  $\alpha$  is a scalar,

it follows that the  $i$  singular values of  $||S_y^{-1} \underline{G}(s)||$  satisfy

$$\sigma_i[\underline{G}'(s)] = S_i^{-1} \sigma_i[\underline{G}(s)] \quad (3-14)$$

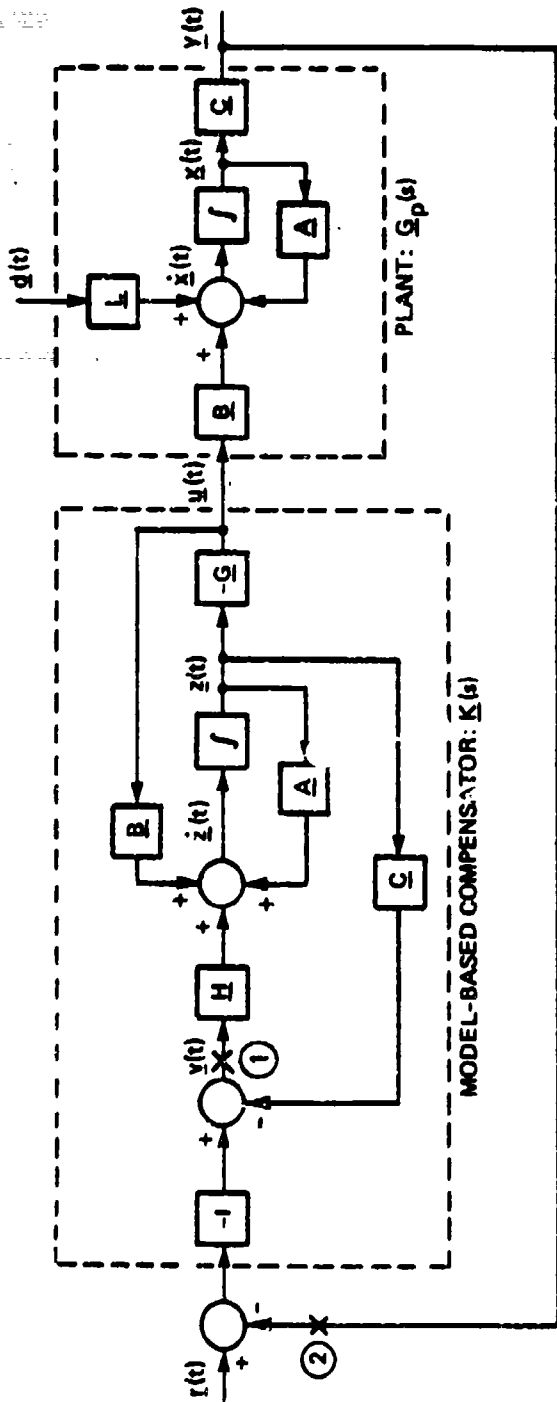
Hence, it is seen that the transformation matrix  $S_y^{-1}$  directly effects the magnitude of the singular values of the original transfer matrix. Equation (3-14) will be an important tool that will be employed in Chapter 4 to help select appropriate scaling transformations to achieve consistent loop shaping.

### 3.2 LOG Compensator

The Model Based Compensator (MBC) has evolved from the optimal estimation theory (Kalman Filter) and optimal control theory (Linear-Quadratic Feedback). The concepts presented here can be found in more complete form in references [10] and [11]. The form of the compensator used in this design together with the state definitions is shown in Figure 3-4 with the plant and compensator dynamics represented separately. The transfer function definitions used in the remainder of this paper will be based on Figure 3-4.

Referring to Figure 3-4, the error  $e(t)$  is the input and  $u(t)$  is the output of the compensator; the overall MBC transfer matrix is defined by

$$\underline{u}(s) = \underline{K}(s) \underline{e}(s)$$



#### OPEN LOOP PLANT

$$\begin{aligned}\dot{\bar{x}}(t) &= \underline{A}\bar{x}(t) + \underline{B}\bar{u}(t) + \underline{L}d(t) \\ \bar{y}(t) &= \underline{C}\bar{x}(t) \\ \bar{y}(s) &= \underline{G}_p(s)\bar{u}(s) \\ \underline{G}_p(s) &= \underline{C}(s\underline{I} - \underline{A})^{-1}\underline{B}\end{aligned}$$

#### MODEL-BASED COMPENSATOR

$$\begin{aligned}\dot{\bar{z}}(t) &= \underline{A}\bar{z}(t) + \underline{B}\bar{u}(t) + \underline{H}\bar{y}(t) \\ \bar{y}(t) &= \bar{y}(t) - \underline{C}\bar{z}(t) - \bar{r}(t) = -\bar{e}(t) - \underline{C}\bar{z}(t) \\ \bar{u}(t) &= -\underline{G}\bar{z}(t) \\ \bar{u}(s) &= \underline{K}(s)\bar{e}(s) \\ \underline{K}(s) &= \underline{G}(s\underline{I} - \underline{A} + \underline{B}\underline{C} + \underline{H}\underline{C})^{-1}\underline{H}\end{aligned}$$

Figure 3.4. The model based compensator in a feedback configuration.

where

$$\underline{K}(s) = \underline{G}(\underline{sI} - \underline{A} + \underline{BG} + \underline{HC})^{-1} \underline{H} \quad (3-15)$$

Also, it is easily shown that the overall closed-loop transfer function,  $\underline{\phi}_{CL}(s)$  is

$$\underline{\phi}_{CL}(s) = \frac{\det(\underline{sI} - \underline{A} + \underline{BG})}{\det(\underline{sI} - \underline{A} + \underline{HC})} \quad (3-16)$$

It follows that the requirements for stability of the system are:

$$\text{Re } \lambda_i[\underline{A} - \underline{BG}] < 0 \quad (3-17)$$

and

$$\text{Re } \lambda_i[\underline{A} - \underline{HC}] < 0 \quad (3-18)$$

which are the poles of the compensator.

The conditions for ensuring a stable compensator are now postulated. From linear system theory, if the pair  $[\underline{A}, \underline{B}]$  is controllable (or stabilizable), then there exists at least one feedback gain matrix  $\underline{G}$  to ensure that all closed-loop poles of  $[\underline{A} - \underline{BG}]$  are in the left half s-plane.  $\underline{G}$  is given by

$$\underline{G} = \underline{R}^{-1} \underline{BK} \quad (3-19)$$

where  $\underline{K}$  solves the Control Algebraic Ricatti Equation (CARE):

$$0 = -\underline{KA} - \underline{A}^T \underline{K} - \underline{Q} + \underline{KBR}^{-1} \underline{B}^T \underline{K} \quad (3-20)$$

Likewise, if the pair  $[A, C]$  is controllable (or detectable), then there exists at least one output gain matrix  $H$  such that all closed-loop poles are in the left half  $s$ -plane. The matrix  $H$  is given by:

$$\underline{H} = \underline{\Sigma} \underline{C}^T \underline{\Sigma}^{-1} \quad (3-21)$$

where  $\underline{\Sigma}$  solves the Filter Algebraic Ricatti Equation (FARE):

$$0 = \underline{\Sigma} A + A^T \underline{\Sigma} + \underline{L} \underline{L}^T - \underline{\Sigma} C^T \theta^{-1} C \underline{\Sigma} \quad (3-22)$$

### 3.3 Loop-Transfer Recovery

In the sequel, some properties of the Kalman Filter that forms the basis for the Loop-Transfer Recovery (LTR) method to be employed in this design will be discussed. The Kalman Filter loop transfer function,  $\underline{G}_{KF}$ , is taken at point 1 on Figure 3-4. The resulting loop-transfer function is defined

$$\underline{G}_{KF} \triangleq \underline{C} (sI - A)^{-1} \underline{H} \quad (3-23)$$

One can also define  $\underline{G}_{FOL}$ , the filter open-loop transfer function as

$$\underline{G}_{FOL} \triangleq \underline{C} (sI - A)^{-1} \underline{L} \quad (3-24)$$

where  $\underline{L}$  is a free design parameter that is chosen to give  $\underline{G}_{FOL}$  desirable singular values to meet the performance and robustness specifications.

The Kalman Filter Domain Equality

$$[\underline{I} + \underline{G}_{KF}(s)] [\underline{I} + \underline{G}_{KF}(s)]^H = \underline{I} + \frac{1}{\mu} \underline{G}_{FOL}(s) \underline{G}_{FOL}^H(s) \quad (3-25)$$

has been derived from Eq. (3-22), (3-23), and (3-24) where the substitution

$$\underline{\theta} = \underline{\mu I} \quad \text{for } \mu > 0$$

has been made in the FARE Eq. (3-22).

As

$$\mu \rightarrow 0$$

in Eq. (3-25), it follows directly from the definition of singular values that

$$\sigma_i[\underline{G}_{KF}(j\omega)] \approx \sigma_i\left[\frac{1}{\sqrt{\mu}} \underline{G}_{FOL}(j\omega)\right] \quad (3-26)$$

which is valid for low frequency range, and represents the recovery of the loop shapes of the  $\underline{G}_{KF}$  from  $\underline{G}_{FOL}$ . The value of  $\mu$  is also a free-design parameter.

The Kwakernaack Loop Transfer Recovery process (see e.g., Doyle, Stein [1], Kwakernaack [12]) is described next, in which the shapes of the Kalman Filter singular values of Eq. (3-26) are recovered in the loop-transfer matrix of the Model Based Compensator. The loop-transfer matrix of Figure 3-4 is given by

$$\underline{T} = \underline{G}(s) \underline{K}(s) = \underline{C}(s\underline{I} - \underline{A})^{-1} \underline{B} \underline{G}(s\underline{I} - \underline{A} + \underline{B} \underline{G} + \underline{H} \underline{C})^{-1} \underline{H} \quad (3-27)$$

The LTR method sets

$$\underline{R} = \underline{I}$$

and

$$\underline{Q} = \rho \underline{C} \underline{C}^T$$

in the CARE Eq. (3-20). Then, as

$$q \rightarrow \infty$$

the corresponding  $\underline{G}_\infty$  in Eq. (3-27) becomes 'large' so that Eq. (3-27) becomes

$$\underline{T}_\infty \approx \underline{C}(\underline{sI} - \underline{A})^{-1} \underline{H} \quad (3-28)$$

and, consequently

$$\sigma_1[\underline{T}_\infty(j\omega)] \rightarrow \sigma_1[\underline{C}(j\omega I - \underline{A})^{-1} \underline{H}] \quad (3-29)$$

for low frequencies.

The LTR method is guaranteed to work in the open-loop system is minimum phase. For non-minimum phase systems there is no such guarantee, although some recovery of performance and robustness properties are expected as the non-minimum phase zeros move further away from the desired operating bandwidth (see [13]).

#### Robustness Theorems

The following robustness properties can be derived from the Kalman Filter Equality (3-25) and are required for system robustness:

$$(1) \quad \sigma_{\min}[\underline{I} + \underline{G}_{KF}(j\omega)] \geq 1 \quad (3-30)$$

which follows directly from the KFE; and

$$(2) \quad \sigma_{\min}[\underline{I} + \underline{G}_{KF}^{-1}(j\omega)] \geq \frac{1}{2} \quad (3-31)$$

which has been proved by Kappos [9].

## CHAPTER 4

### COMPENSATOR DESIGN PROCEDURE

#### 4.1 Augmented Dynamics

Augmenting the dynamics of the submersible control system serves a dual purpose. One is to model the actuator dynamics to make the model as accurate as possible, and achieve desirable roll-off at crossover for robustness. The other is to include integrators to cause the compensator to behave as a type-1 system, which will permit the submersible to achieve zero steady-state error to step inputs and disturbances (i.e., good command following). The result will be to increase the order of the system by four in the present two-input design.

A block diagram of the augmented model appears in Figure 4-1. It is seen that the augmented dynamics have been placed in the command channel.  $\underline{u}_c$  is the true commanded input (a physical variable),  $\underline{u}_{act}$ , the output of the augmented dynamics, is not. The mathematics of the augmented states will be manipulated in such a way as to provide a means to achieve the desired loop shapes of  $\underline{G}_{POL}$ .

#### Actuator Dynamics

The complete actuator dynamics are governed by their mass properties of the rudder and planes, and angle rate limits imposed by the electro-hydraulic servomechanisms that position them. Since the rate limits are highly nonlinear, they will not be modeled per se. Instead,

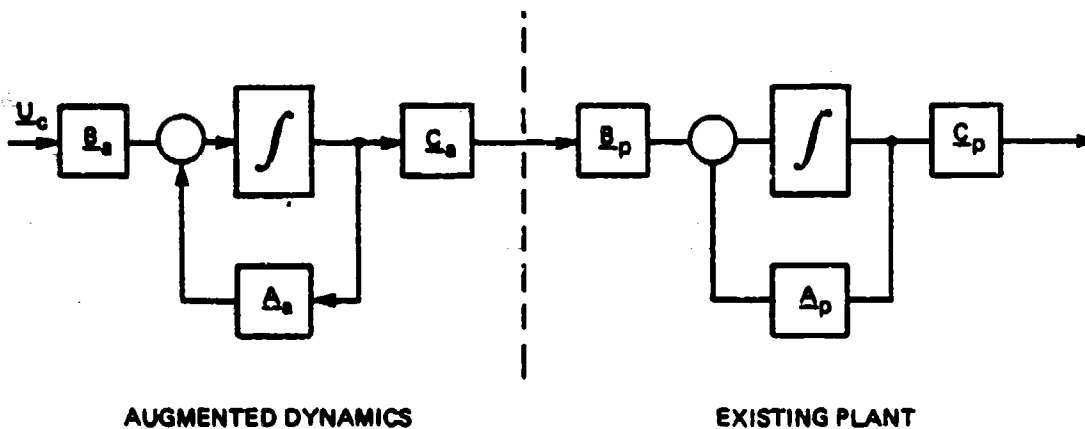


Figure 4-1. Augmented dynamics placed in command variable channel of plant.

the compensator will be designed so that the rudder and stern planes are never driven past their rate limits of 7 and 6 degrees/second respectively, nor past their maximum allowable deflection angle.

The actuator dynamics of the rudder are represented by a second-order system. These are given for the stern planes as

$$\omega_d = 1.37$$

$$\zeta = 0.9$$

and for the rudder as

$$\omega_d = 1.09$$

$$\zeta = 0.9$$

as  $\zeta$  approaches unity, a second-order system begins to lose its oscillatory characteristics and behavior tends toward a first-order system. Since this is very nearly an overdamped system, the actuators will be modeled as a first-order system. By Ogata [15] the rise time for a second-order system is given by

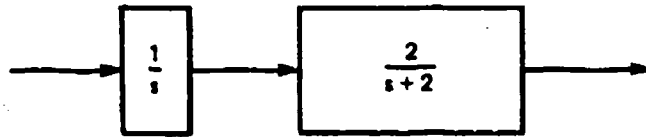


Figure 4-2. Stern plane command channel with augmented dynamics.

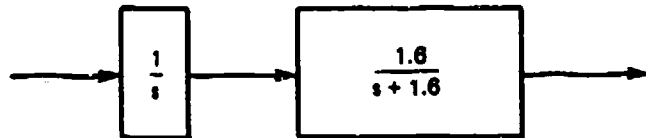


Figure 4-3. Rudder command channel with augmented dynamics.

These dynamics are introduced to the 8th order state space representation to produce a 12th order system. To get it in a form for further design manipulation a new state vector is defined

$$\dot{\underline{x}} = \begin{pmatrix} \dot{\underline{x}}' \\ \dot{\underline{x}}_s \end{pmatrix}$$

where  $\underline{x}'$  is the unaugmented 8th order system augmented with the two command channel actuator time lag states and  $\underline{x}_s$  are the two integrator states in the command channel. The augmented system can be written as

$$\begin{pmatrix} \dot{x}'_1 \\ \dot{x}'_2 \end{pmatrix} = \begin{bmatrix} \underline{A}_{8 \times 8} & \underline{B}_8 & 0 \\ \hline 0 & -\frac{1}{\tau_{\delta s}} & 0 & \frac{1}{\tau_{\delta s}} & 0 \\ 0 & 0 & -\frac{1}{\tau_{\delta r}} & 0 & \frac{1}{\tau_{\delta r}} \\ \hline 0 & 0 & 0 & 0 & 0 \end{bmatrix} \begin{pmatrix} \underline{x}' \\ \underline{x}'_8 \end{pmatrix} + \begin{bmatrix} 0 \\ 1 & 0 \\ 0 & 1 \end{bmatrix} \underline{u}$$

$$\underline{y} = \begin{bmatrix} \underline{C}_8 & 0 & 0 \end{bmatrix} \begin{pmatrix} \underline{x}' \\ \underline{x}'_8 \end{pmatrix}$$

and simplifying let

$$\begin{pmatrix} \dot{\underline{x}}' \\ \dot{\underline{x}}'_8 \end{pmatrix} = \begin{bmatrix} \underline{A}_{10} & \underline{B}_r \\ \hline 0 & 0 \end{bmatrix} \begin{pmatrix} \underline{x}' \\ \underline{x}'_8 \end{pmatrix} + \begin{bmatrix} \underline{B} \end{bmatrix} \underline{u} = \underline{Ax} + \underline{Bu}$$

$$\underline{y} = \begin{bmatrix} \underline{C}_{10} & 0 \end{bmatrix} \begin{pmatrix} \underline{x}' \\ \underline{x}'_8 \end{pmatrix} = \underline{Cx} \quad (4-2)$$

This form of state space equations will be used in Section 4.2 to derive suitable loop-shaping algorithms. The  $\underline{A}$  and  $\underline{B}$  matrices of the augmented system are found in Appendix B.

#### Augmented System Dynamics

The four additional states add two poles at the origin and one each at -1.6 and -2.0 to those already listed in Table 2-4. The multivariable zeros for both the  $r - \theta$  and  $\dot{\psi} - \dot{z}$  system are listed in Table 4-1. Note

OPEN LOOP PLANT ON R-THETA

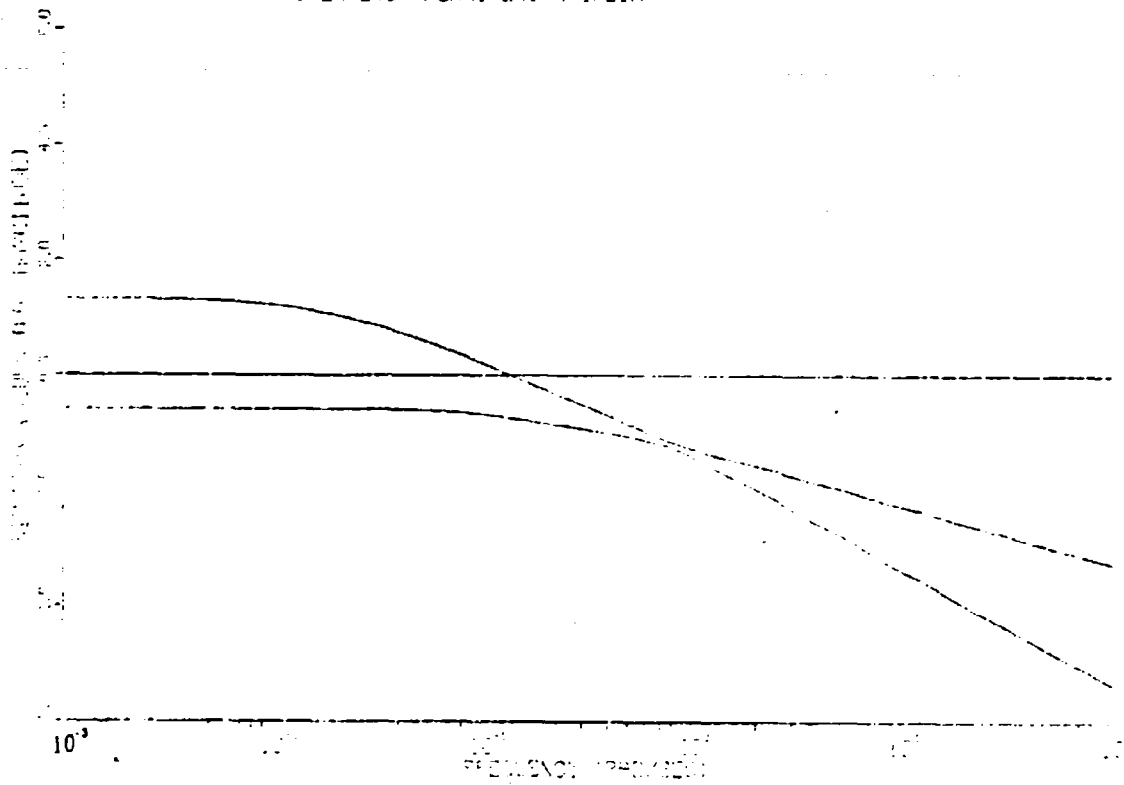


Figure 4-4. Unaugmented open-loop plant; r -  $\theta$  system; singular values vs frequency.

OPEN LOOP PLANT 2X8  $\psi - \dot{z}$

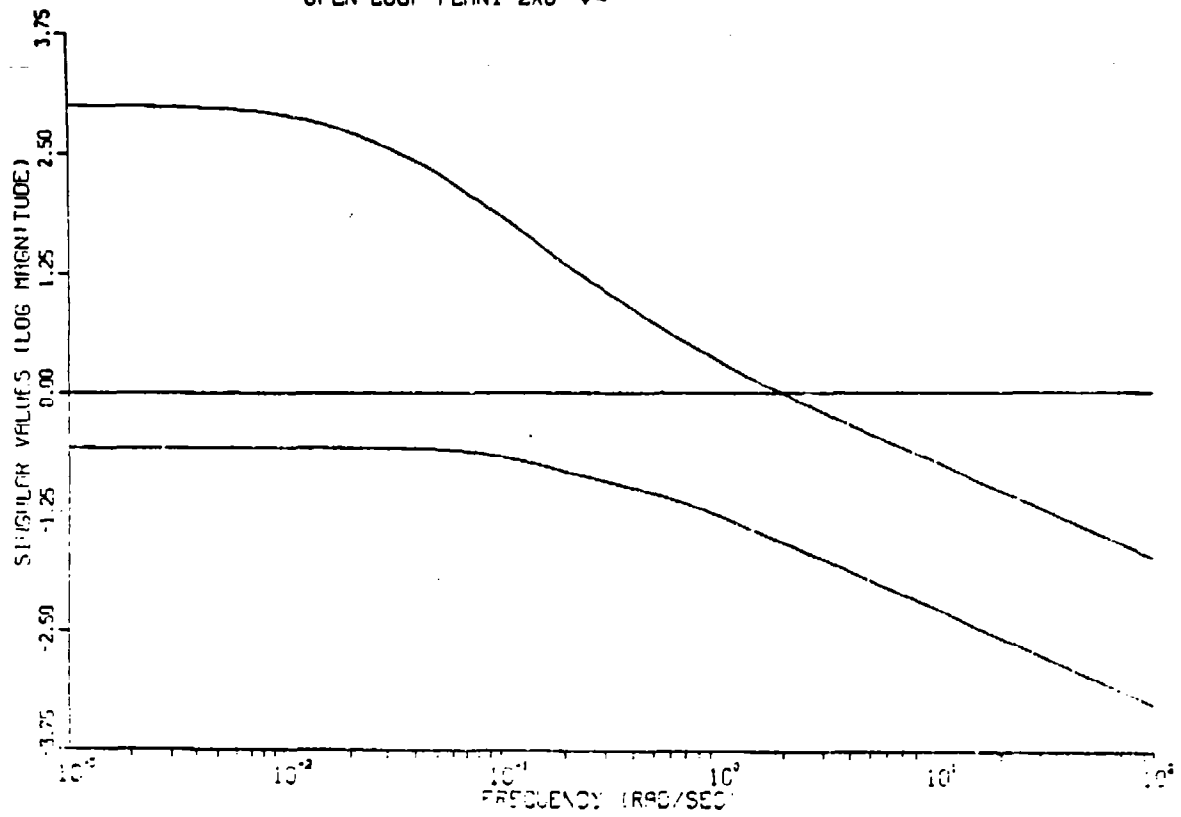


Figure 4-5. Unaugmented open-loop plant;  $\psi - \dot{z}$  system; singular values vs frequency.

OPEN LOOP PLANT 2X12 R, THETA UNSCALED

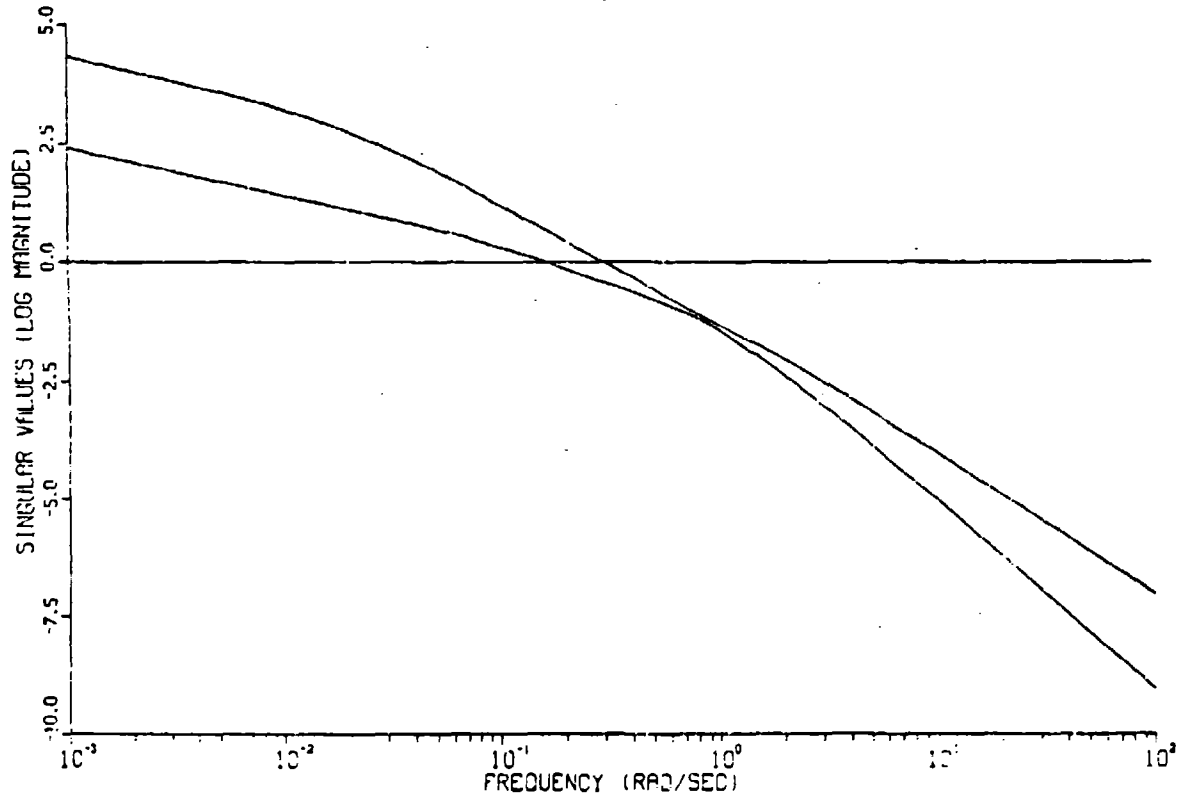


Figure 4-6. Augmented open-loop plant;  $r - \theta$  system; singular values vs frequency.

Table 4-1. Augmented system zeros (finite).

r -  $\theta$  System Zeros:

NUMBER	REAL	IMAG	DAMPING	FREQUENCY
1	-3.796252290E-02			
2	-1.57845617E-01			
3	-2.907426130E-01			
5	-1.88200004E-01	-3.06042303E-01	5.23827439E-01	3.59278428E-01

$\dot{\psi}$  -  $\dot{z}$  System Zeros:

NUMBER	REAL	IMAG	DAMPING	FREQUENCY
1	-3.79647618E-02			
2	-2.387798847E-01			
3	-3.115217184E-01			
5	-1.813410260E-01	-3.08824069E-01	5.06355747E-01	3.58129688E-01
6	7.209455317E-01			

that  $\dot{\psi}$  -  $\dot{z}$  system has a non-minimum phase zero at 0.7, the existence of which is most likely due to the relationship between the pitch ( $\theta$ ) and heave ( $w$ ) states in  $z$ . It is pointed out here that both the actuator dynamics and the non-minimum phase zero are beyond the desired system bandwidth of 0.1. Therefore, they are not expected to effect the design appreciably. However, the actuators have been incorporated in the design, to provide additional roll-off at higher frequencies.

Open-Loop Transfer Function

The singular values of the unaugmented (8th order)  $G_{OL}$  systems are plotted in Figure 4-4 and 4-5. In both of these figures, the minimum singular values correspond primarily to the turn related outputs,  $\dot{\psi}$  and  $r$ . The beginning of gain roll-off corresponds to a system pole as it would in a Bode plot. The maximum singular values in both figures begin to roll-off at  $10^{-2}$  radians/s, which corresponds to the pole at -0.013

OPEN LOOP PLANT 2X12 ZDOT, PSIDOT UNSCALED

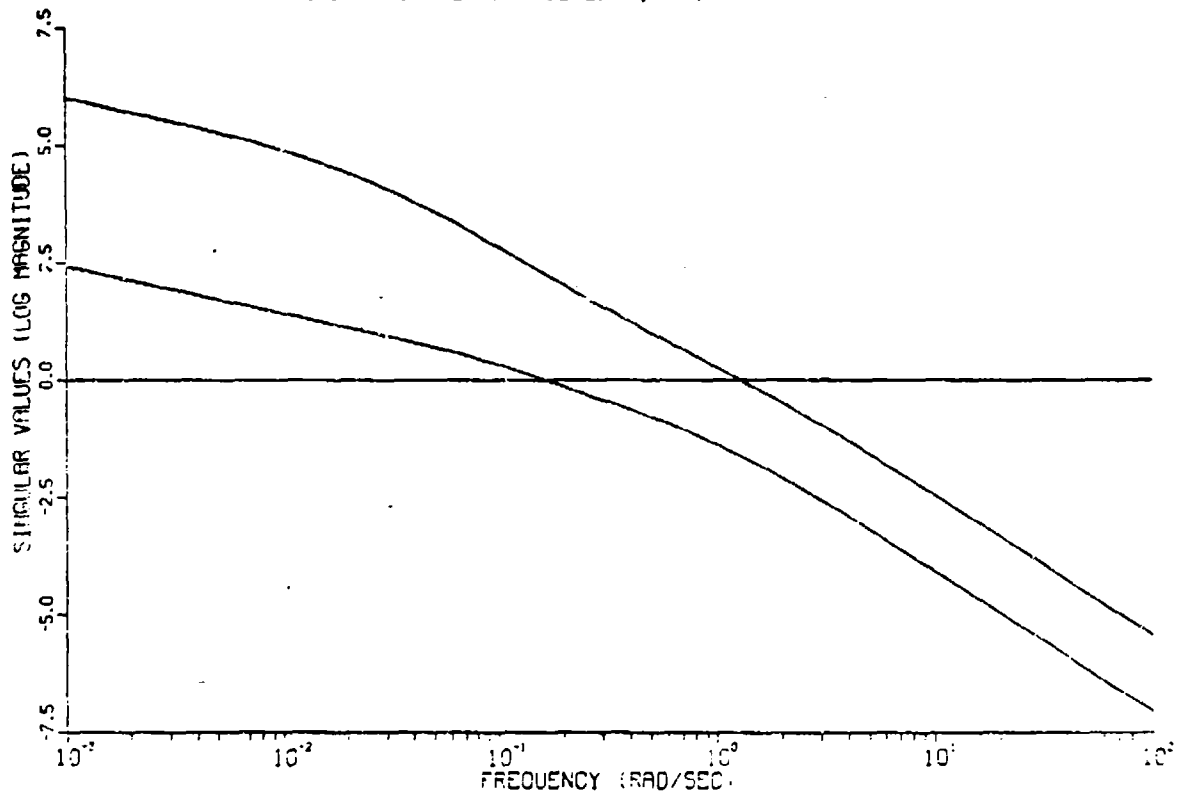


Figure 4-7. Augmented open-loop plant;  $\dot{\psi} - \dot{z}$  system; singular values vs frequency.

(the  $\theta$  -  $w$  dominated eigenvector of Figure 2-6). The minimum singular values start to roll-off at  $10^{-1}$  radians/s, which relates to the pole at  $-0.097$ . This pole corresponds to the "slowest" eigenvector to first contain components of the  $r$  state. The bandwidth corresponding to the  $r$  and  $\dot{\psi}$  outputs is nearly an order of magnitude greater than the  $z$  and  $\theta$  outputs.

The open-loop singular values of the augmented (12th order) system are shown in Figure 4-6 and 4-7. The integrators in the command channel correspond to the slope of  $1/s$  or 20 dB/decade at low frequency. Also note that the minimum singular values of both figures are nearly identical over the chosen frequency range. It will be shown that either choice of  $r$  or  $\dot{\psi}$  as an output variable will result in nearly equal performance in the controller design.

#### 4.2 Loop-Shaping Techniques

In Chapter 3 the notion of the free-design parameter  $\mu$  and matrix  $\underline{L}$  was introduced to provide a means of shaping the singular values to meet the design specifications. In this section, the author will derive a procedure to obtain  $\sigma_i[\underline{G}_{\text{FOL}}]$  that are tied together throughout the desired operating bandwidth, and will eventually result in a desirable tight cross pattern of the Model Based Compensator loop transfer function  $\underline{T}(s)$ .

The filter open-loop transfer function is given in Eq. (3-24) as

$$\underline{G}_{\text{FOL}} = \underline{C}(s\underline{I} - \underline{A})^{-1} \underline{L}$$

Let  $\underline{L}$  be of the form

$$\underline{L} = \begin{bmatrix} \underline{L}_1 \\ \underline{L}_2 \end{bmatrix}$$

where

$\underline{L}_1$  is all states excluding the integrator states

$\underline{L}_2$  is the integrator states

and, starting with the full augmented system dynamics in the state space form as developed in Eq. (4-2)

$$\underline{A} = \begin{bmatrix} \underline{A}_{10} & \underline{B}_\tau \\ 0 & 0 \end{bmatrix}$$

one obtains

$$s\underline{I} - \underline{A} = \begin{bmatrix} s\underline{I} - \underline{A}_{10} & -\underline{B}_\tau \\ 0 & s\underline{I} \end{bmatrix}$$

Taking the block inverse

$$s\underline{I} - \underline{A})^{-1} = \begin{bmatrix} (s\underline{I} - \underline{A}_{10})^{-1} & \frac{(s\underline{I} - \underline{A}_{10})^{-1} \underline{B}_\tau}{s} \\ 0 & \frac{\underline{I}}{s} \end{bmatrix} \quad (4-3)$$

Now for low frequencies

$$s \rightarrow 0$$

$$\underline{C}(s\underline{I} - \underline{A})^{-1} \underline{L} = \begin{bmatrix} \underline{C}_{10} & 0 \\ 0 & \frac{\underline{I}}{s} \end{bmatrix} \begin{bmatrix} \frac{-\underline{A}_{10}^{-1} \underline{B}_{\tau}}{s} \\ \underline{L}_2 \end{bmatrix} \begin{bmatrix} \underline{L}_1 \\ \underline{L}_2 \end{bmatrix}$$

$$= -\underline{C}_{10} \underline{A}_{10}^{-1} \underline{L}_1 - \frac{\underline{C} \underline{A}_{10}^{-1} \underline{B}_{\tau} \underline{L}_2}{s} \quad (4-4)$$

Hence, for small  $s$ , Eq. (4-4) further becomes

$$\underline{C}(s\underline{I} - \underline{A})^{-1} \underline{L} \approx \frac{-\underline{C} \underline{A}_{10}^{-1} \underline{B}_{\tau} \underline{L}_2}{s} \quad (4-5)$$

By Eq. (3-22)

$$\underline{G}_{\text{FOL}}(s) = \underline{C}(s\underline{I} - \underline{A})^{-1} \underline{L}$$

To tie the singular values together, it is desirable to set

$$\underline{G}_{\text{FOL}} \approx \frac{\underline{I}}{s}$$

and, consequently, obtain from (4-5)

$$\frac{\underline{I}}{s} = \frac{-\underline{C} \underline{A}_{10}^{-1} \underline{B}_{\tau} \underline{L}_2}{s} \quad (4-6)$$

Finally, solving for  $\underline{L}_2$

$$\underline{L}_2 = -(\underline{C} \underline{A}_{10}^{-1} \underline{B}_{\tau})^{-1} \quad (4-7)$$

The dependence of the low frequency singular values should be clear;  $\underline{L}_2$  drives the controller through the integrator states.

An analogous method was used to the high frequency singular values together. From Eq. (4-3) it follows that

$$\underline{L}_1 = \underline{C}^T (\underline{C}\underline{C}^T)^{-1} \quad (4-2)$$

#### 4.3 Model Based Compensator Design

Equations (4-7) and (4-8) were applied to both designs. Figures 4-8 and 4-9 are the plots of the shaped  $\sigma_i(G_{FOL})$  which show how the singular values are tied together at low and high frequencies. By varying the design parameter  $\mu$ , these singular values can be shifted up or down. However, neither plot would result in a tight crossover pattern at the desired crossover frequency of 0.08 radians/s. It is through the use of the scaling transformation properties developed in Eq. (3-14) that the shapes of these singular values approach the desired shapes for good command following, disturbance rejection, and crossover frequency specifications.

Referring to Figure 4-8 it is proposed that the minimum singular value,  $r$ , be scaled to match the maximum singular value,  $\theta$ , at its greatest separation. This point occurs at a separation of about 24 dB, which is equivalent to a ratio between the values of  $r$  and  $\theta$  of 16, at a frequency of 0.02 radians/s. For numerical convenience,  $r$  will be scaled by a factor of 10 (versus 16). This means that  $r$  will be observed in "tens of radians, while the output  $\theta$  continues to have units of radians.

A similar approach is applied to figure 4-9. In this case, the maximum separation approaches 4 orders of magnitude. For numerical convenience,  $\dot{\psi}$  will be scaled up by a factor of 10 (the same factor used for  $r$  above), where  $\dot{z}$  is scaled down by 0.01.

PLANT 2X12 C(SI-A)<sup>1</sup> L R, THETA, UNSCALED, SHAPED

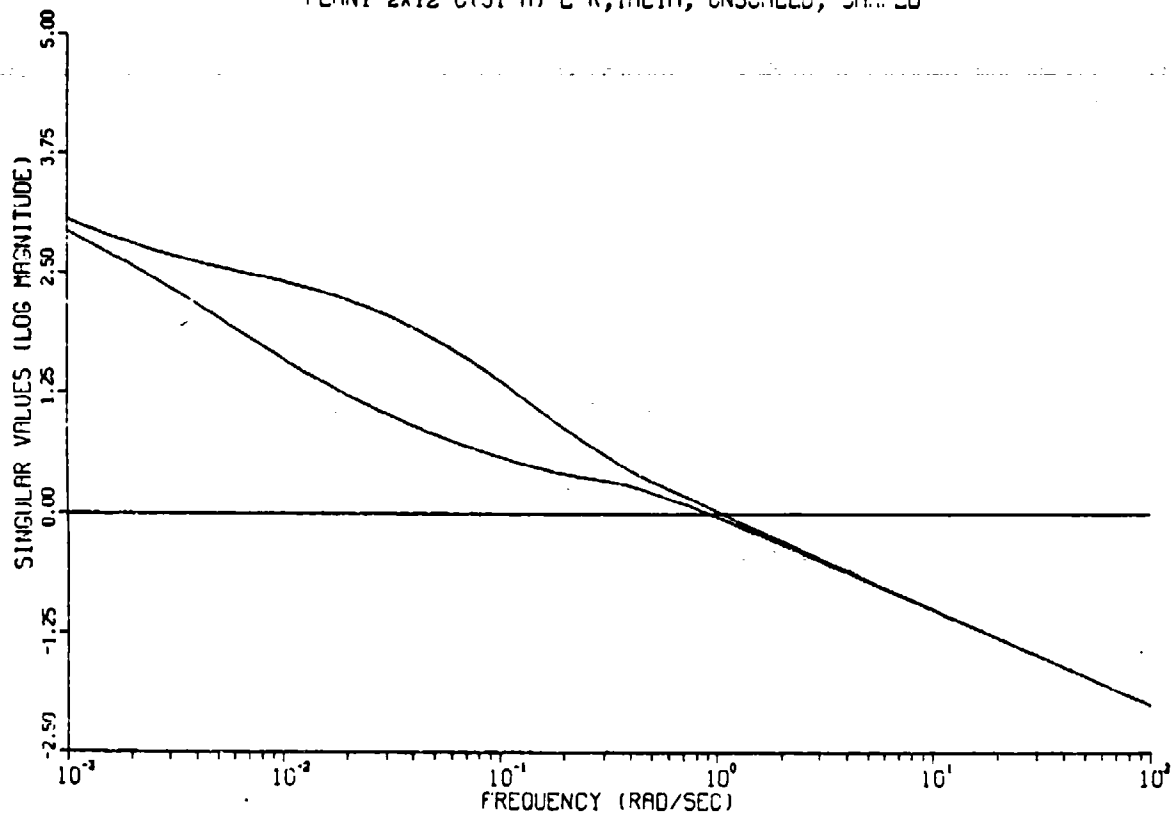


Figure 4-8. Shaped and unshaped filter open-loop transfer function;  $r - \theta$  system; singular values vs frequency.

PLANT 2X12 C(SI-A)<sup>1</sup>L Z,PSI DOT, UNSCALED

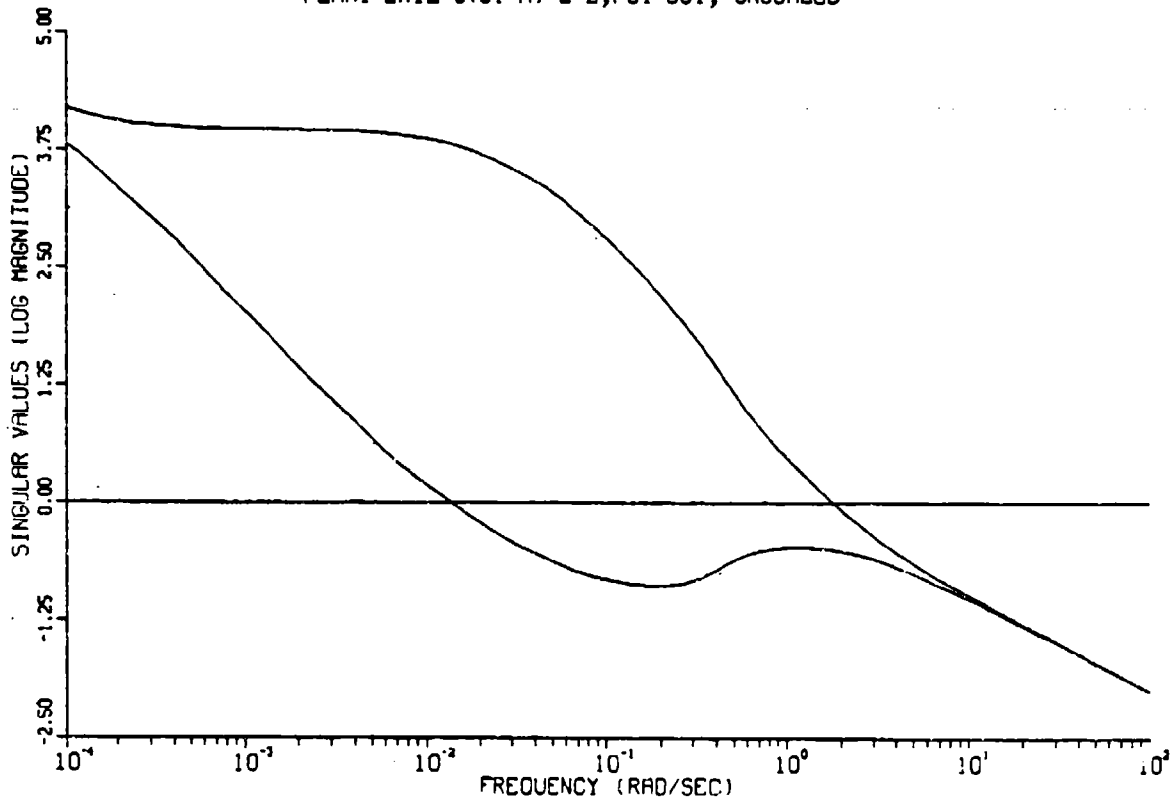


Figure 4-9. Shaped and unshaped filter open-loop transfer function;  $\psi - z$  system; singular values vs frequency.

OPEN LOOP PLANT 2X12 R, THETA SCALED

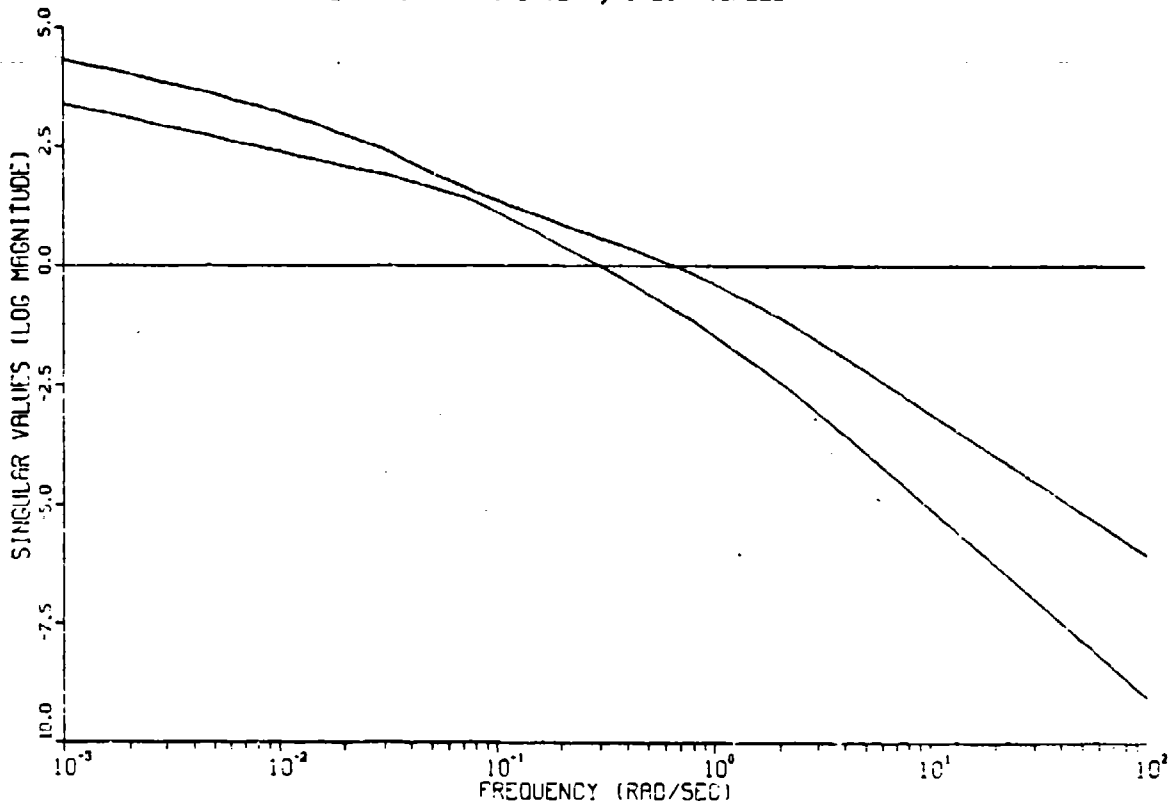


Figure 4-10. Scaled open-loop plant; r -  $\theta$  system; singular values vs frequency.

OPEN LOOP PLANT 2X12 ZDOT, PSIDOT SCALED

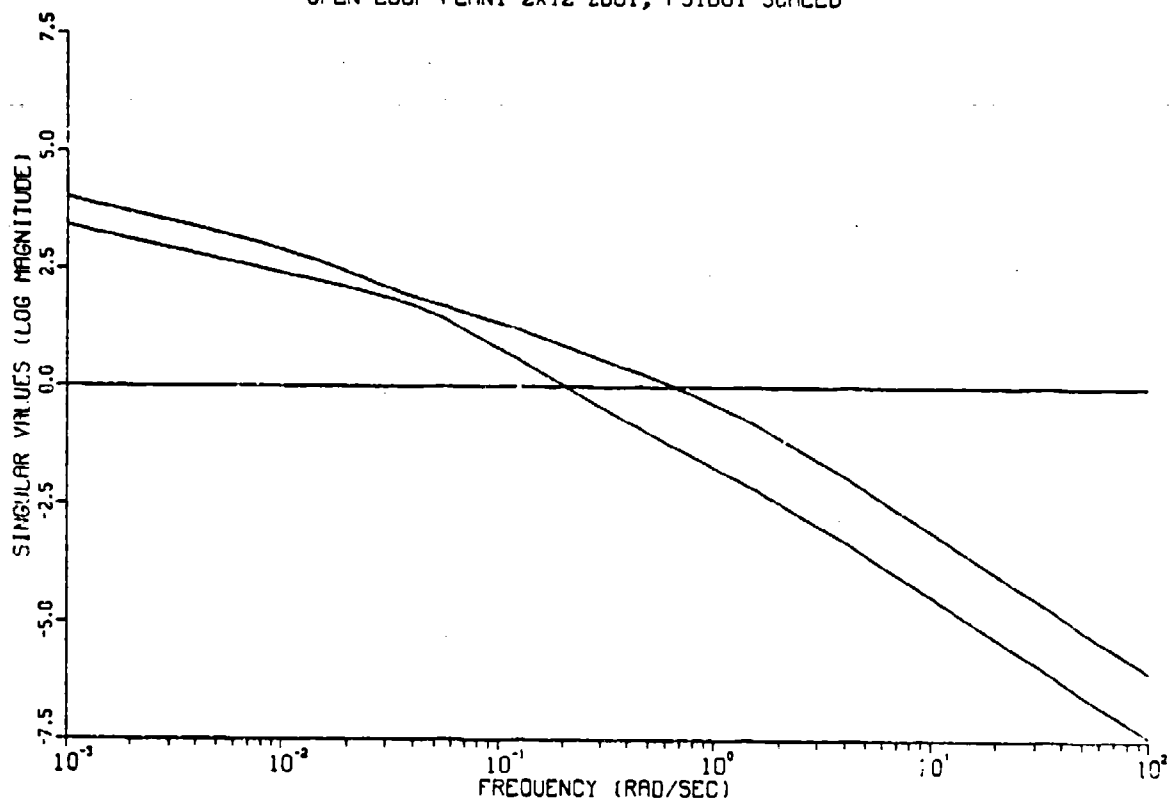


Figure 4-11. Scaled open-loop plant;  $\dot{\psi} - \dot{z}$  system; singular values vs frequency.

PLANT 2X12 C(SI-A)<sup>1</sup> L R, THETA, SCALED, SHAPED

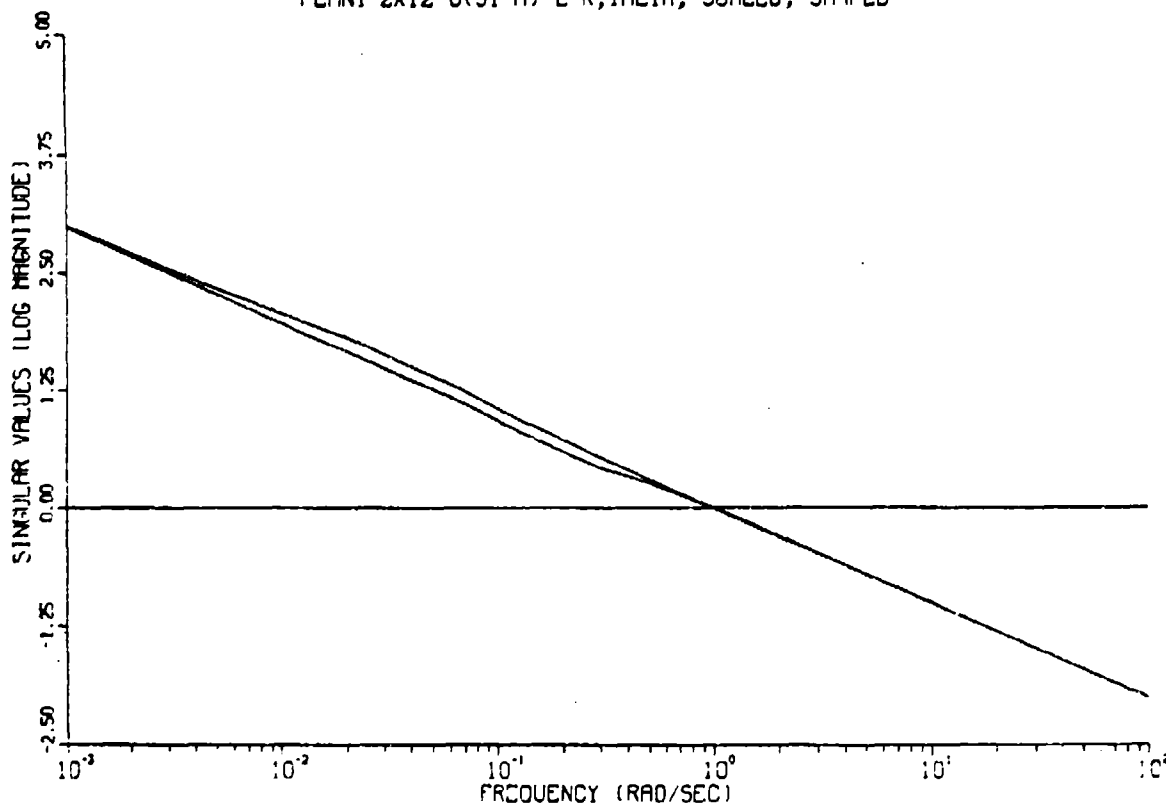


Figure 4-12. Shaped and scaled filter open-loop transfer function;  $r - \theta$  system; singular values vs frequency.

PLANT 2X12 C(SI-A) L Z, PSI DOT, SCALED, SHAPED

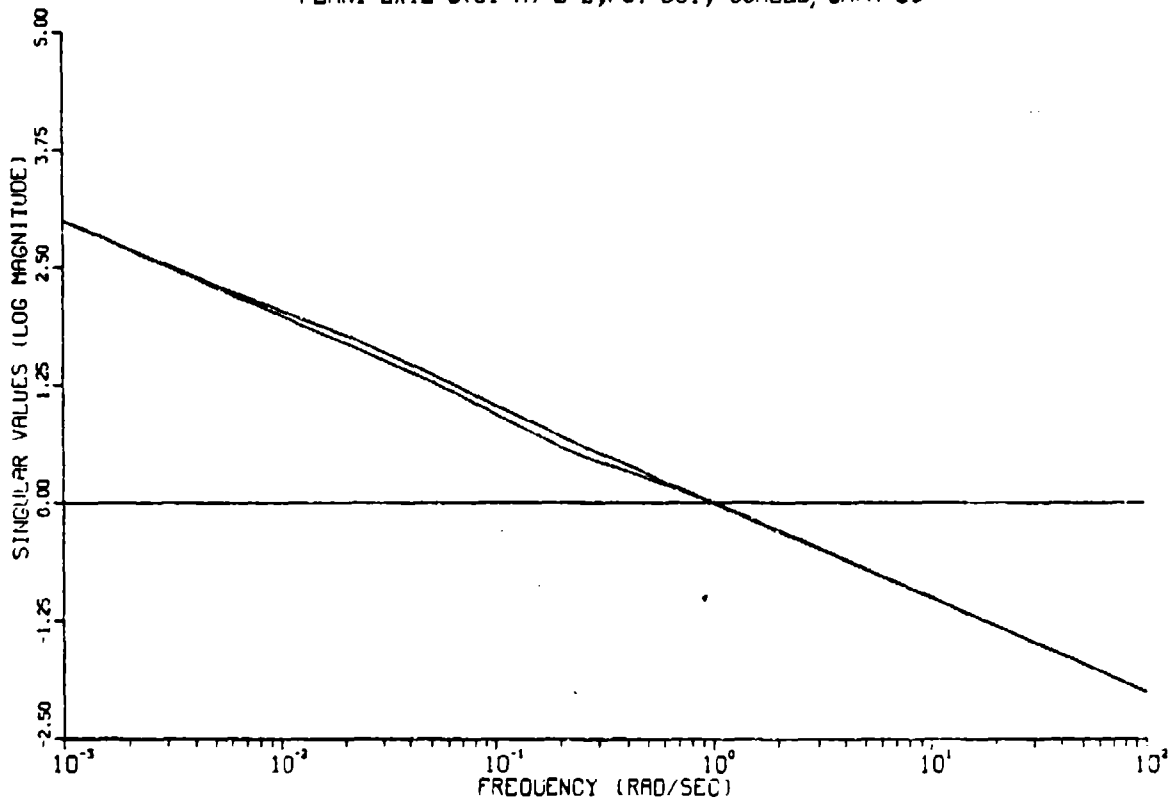


Figure 4-13. Shaped and scaled filter open-loop transfer function;  $\psi - z$  system; singular values vs frequency.

and solving for  $\mu$  then

$$\mu = \left( \sigma_{\max} \left[ \frac{G}{FOL}(\omega_o) \right] \right)^{-2}$$

where  $\delta_o$  is the (maximum) desired crossover frequency. The value of  $\mu$  obtained were 126 and 144 respectively, for the  $r - \theta$  and  $\dot{\psi} - \dot{z}$  controller, using a maximum crossover frequency of 0.09 radians/s.

With the design parameters,  $\mu$ ,  $L$ , and  $S_y^{-1}$  thus determined, the design can proceed with the application of the FARE Eq. (3-22) and (3-21) to calculate the Kalman Filter gain matrix  $H$ . The singular values of  $G_{KF}$  are plotted in Figures 4-14 and 4-15. The loop shapes have been recovered in both cases with crossover in the range of 0.07 to 0.09 radians/s.

Finally, the controller gain matrix,  $K$  is calculated by the CARE Eq. (3-20) and (3-19). The only free design parameter to choose is  $q$ , the control weighting index. Generally, to prevent control saturation from high gain of  $K$ , it makes sense to choose  $q$  as small as possible and still meet the design specifications. In both controller designs, when  $q$  was set equal to 10, a crossover of 0.075 radians/s was obtained by the singular values of the loop-transfer matrix,  $T(s)$ . These are plotted in Figures 4-16 and 4-17. Note the roll-off at crossover is 20 dB/decade, as expected, and that Eq. (3-27) fails to hold at frequencies above 0.7 radian/s.

### Robustness

The singular value plots of the Kalman Filter return difference and Kalman Filter inverse return difference matrices are shown in Figure 4-18 and 4-19 for the  $r - \theta$  system, and in Figure 4-20 and 4-21 for the  $\dot{\psi} - \dot{z}$  system. The robustness criteria set forth in Eq. (3-30) and (3-31) have been met.

A discussion of the robustness of the loop-transfer matrix according to Eq. (3-2) is given in Chapter 5.

PLANT 2X12 C(SI-A)-1H

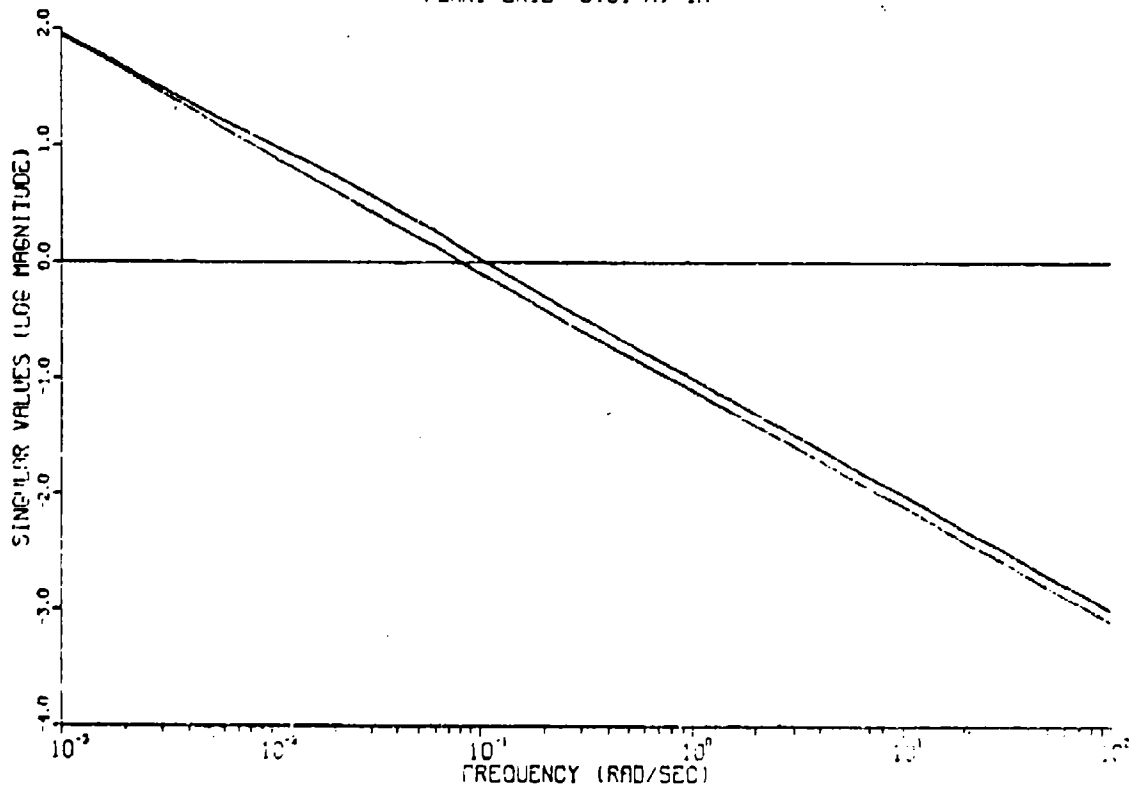


Figure 4-14. Kalman filter loop-transfer function;  $r - \theta$  system; singular values vs frequency.

PLANT 2X12 C(SI-A)-1H,  $\dot{z}$ , PSI

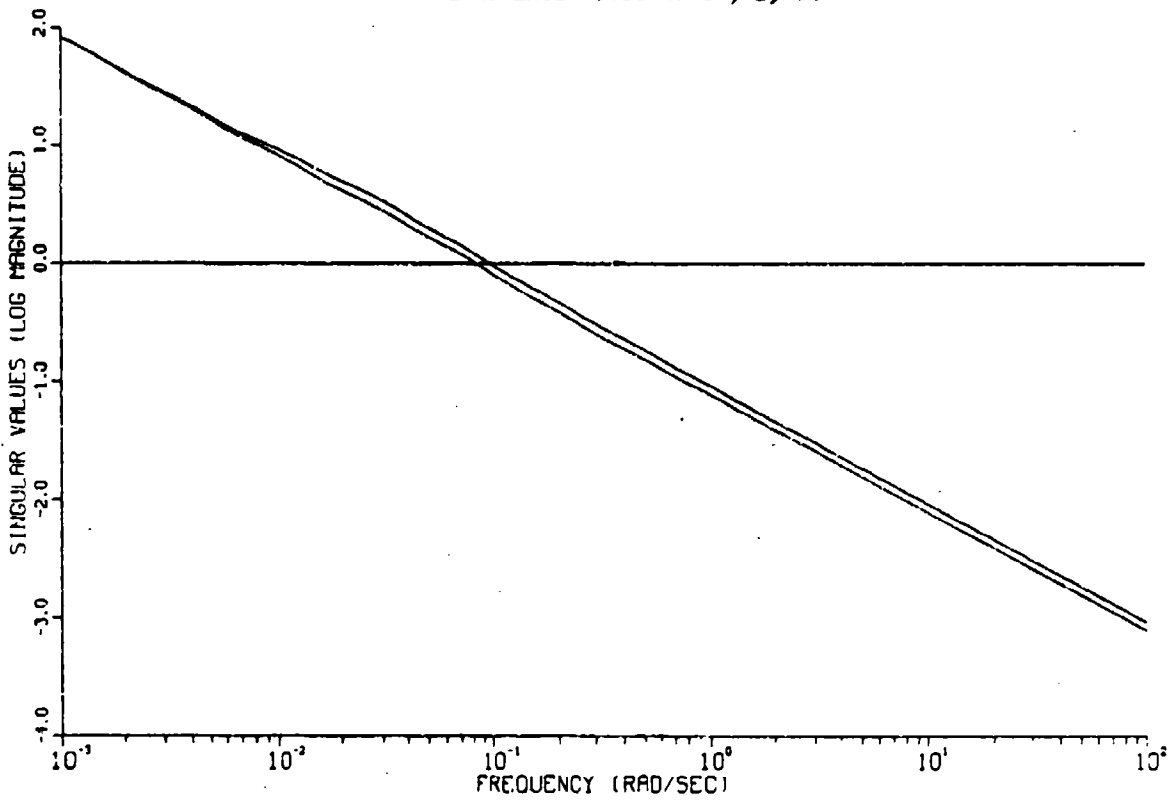


Figure 4-15. Kalman filter loop transfer function;  $\dot{\psi} - \dot{z}$  system; singular values vs frequency.

COMPENSATED SYSTEM 30R2 0-10 THETA, R

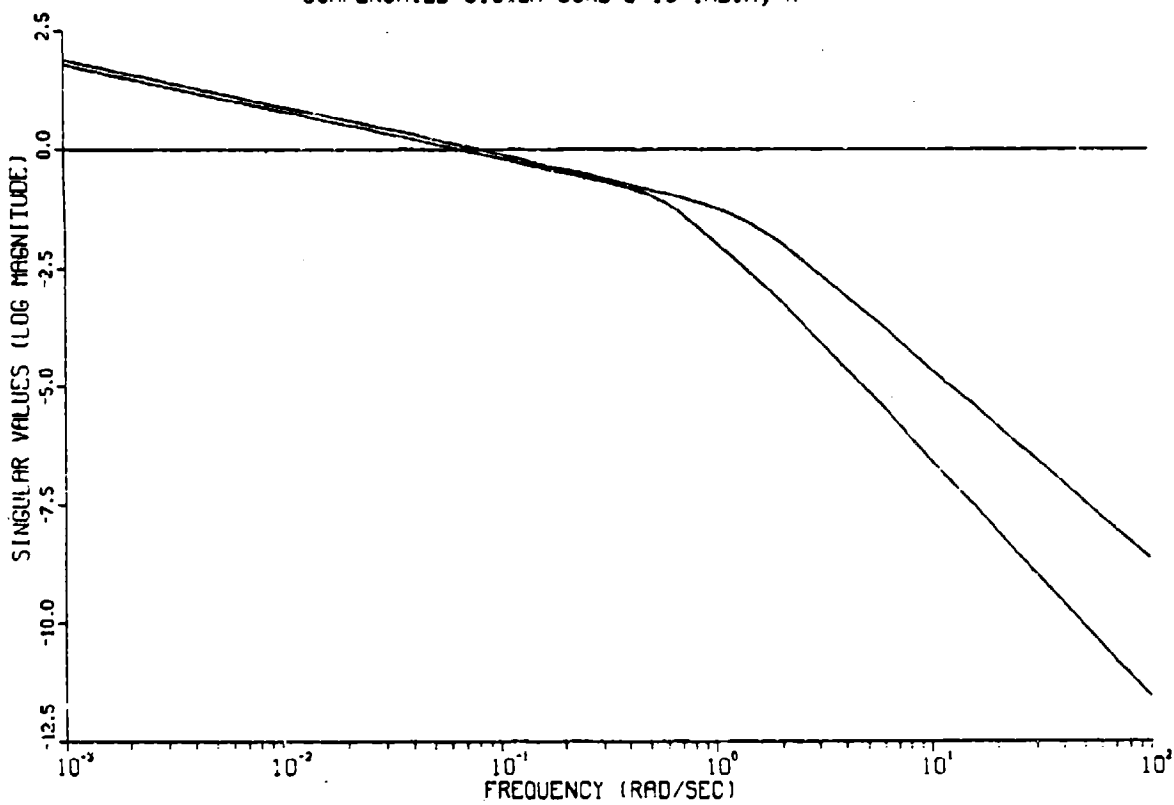


Figure 4-16. Loop-transfer recovery;  $r - \theta$  system; singular values vs frequency.

COMPENSATED SYSTEM 30R2 0-10 Z, PSI DOT

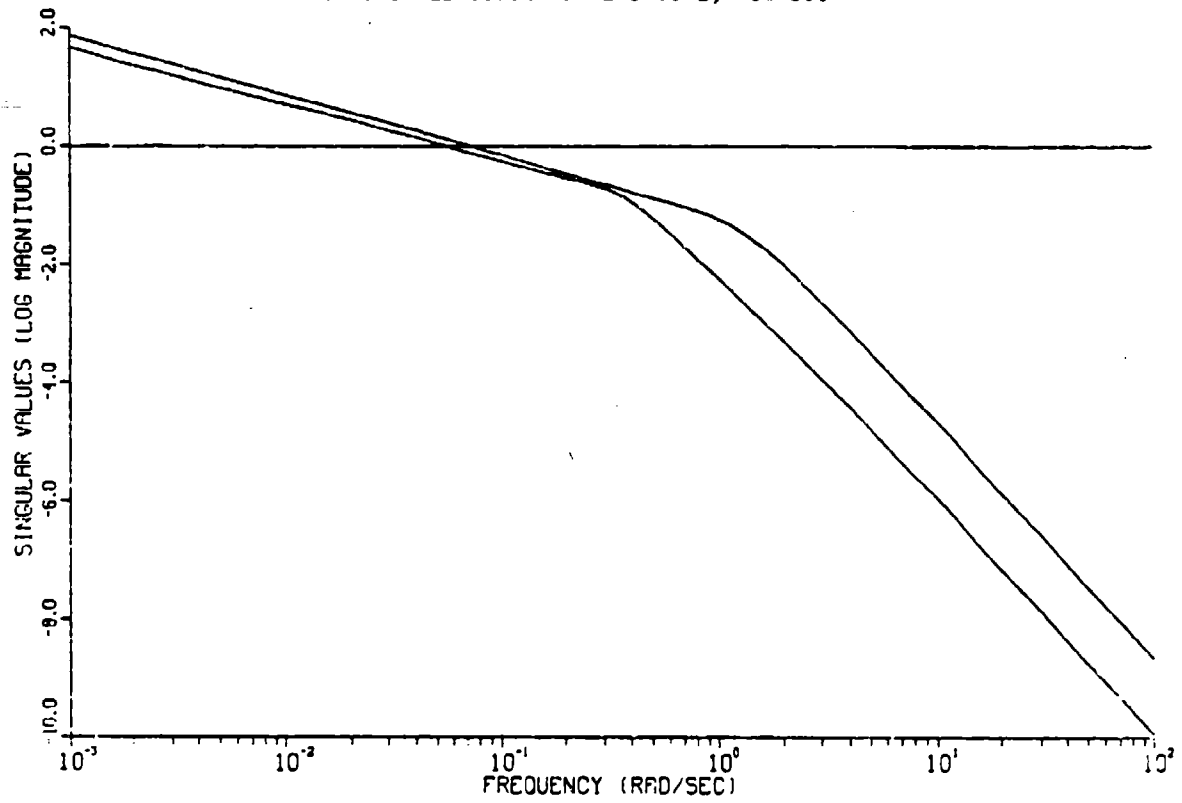


Figure 4-17. Loop-transfer recovery;  $\dot{\psi} - \dot{z}$  system; singular values vs frequency.

(1 + G) R-THETA COMPENSATOR

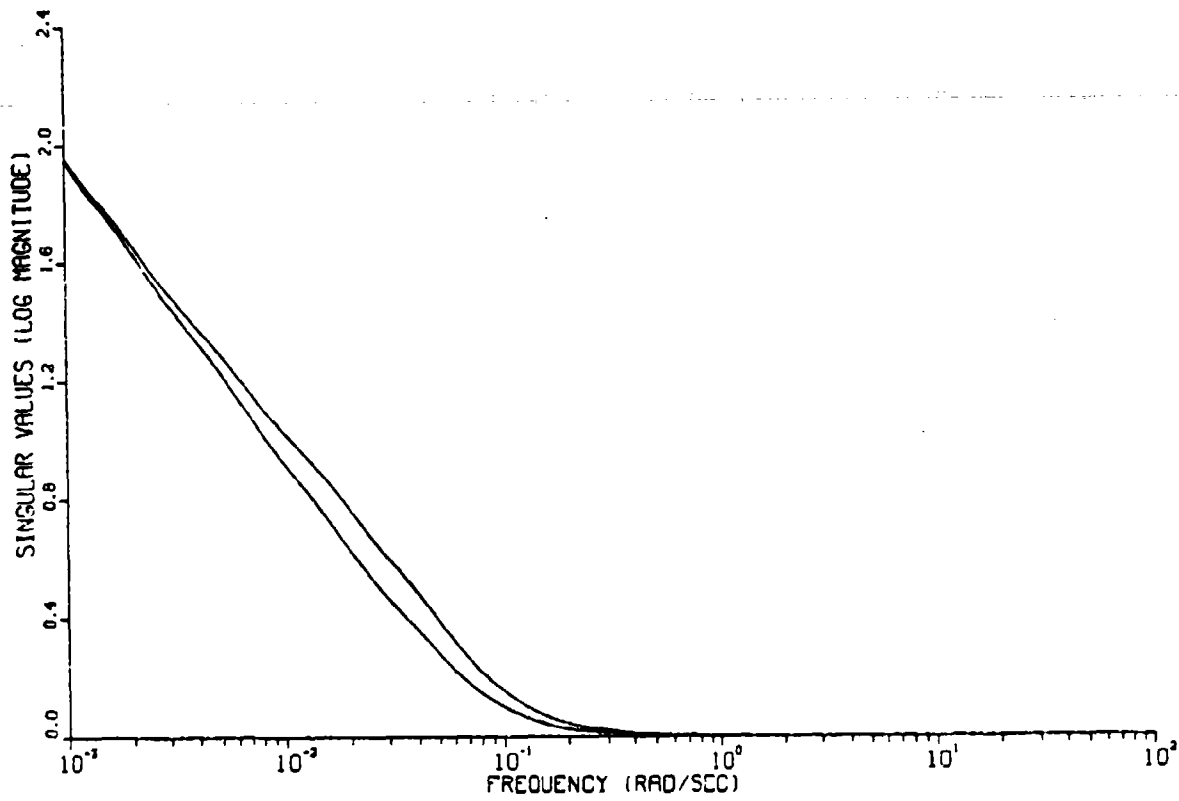


Figure 4-18. Kalman filter return difference; r -  $\theta$  system; singular values vs frequency.

(I + G-1) R-THETA COMPENSATOR

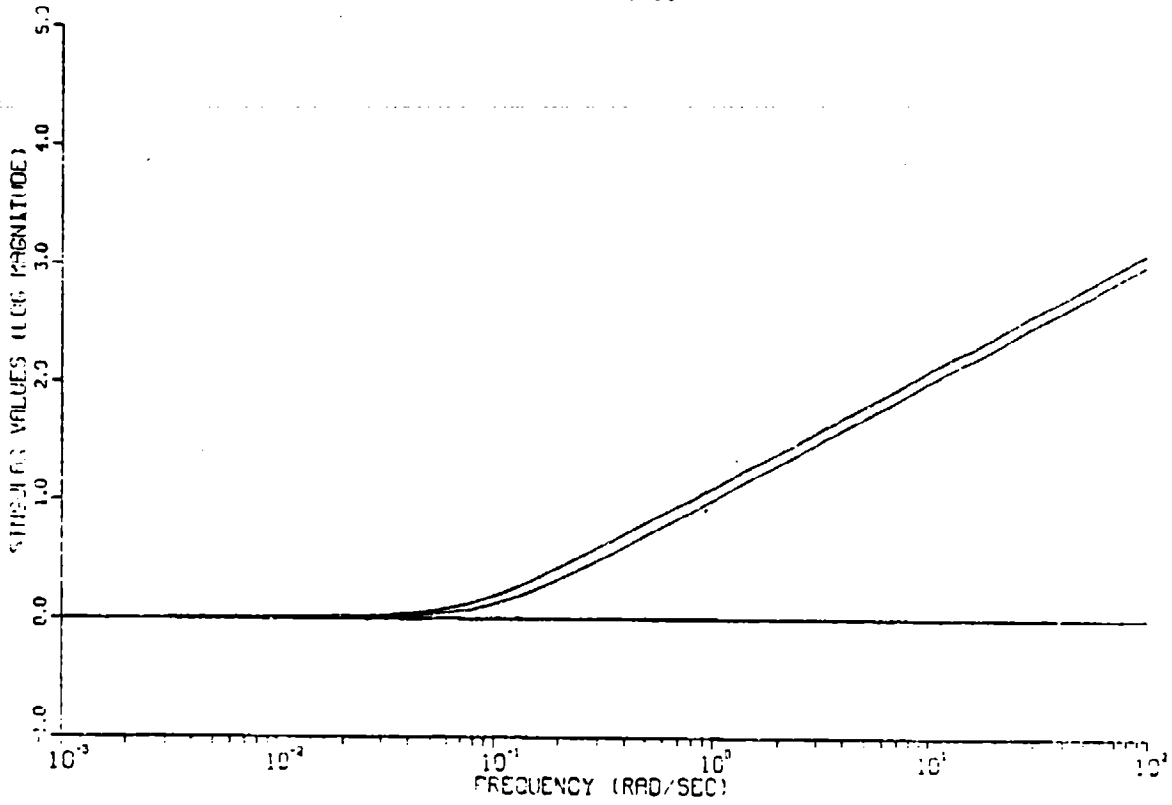


Figure 4-19. Kalman filter inverse return difference; r -  $\theta$  system; singular values vs frequency.

(I + G) PSI - Z DOT COMPENSATOR

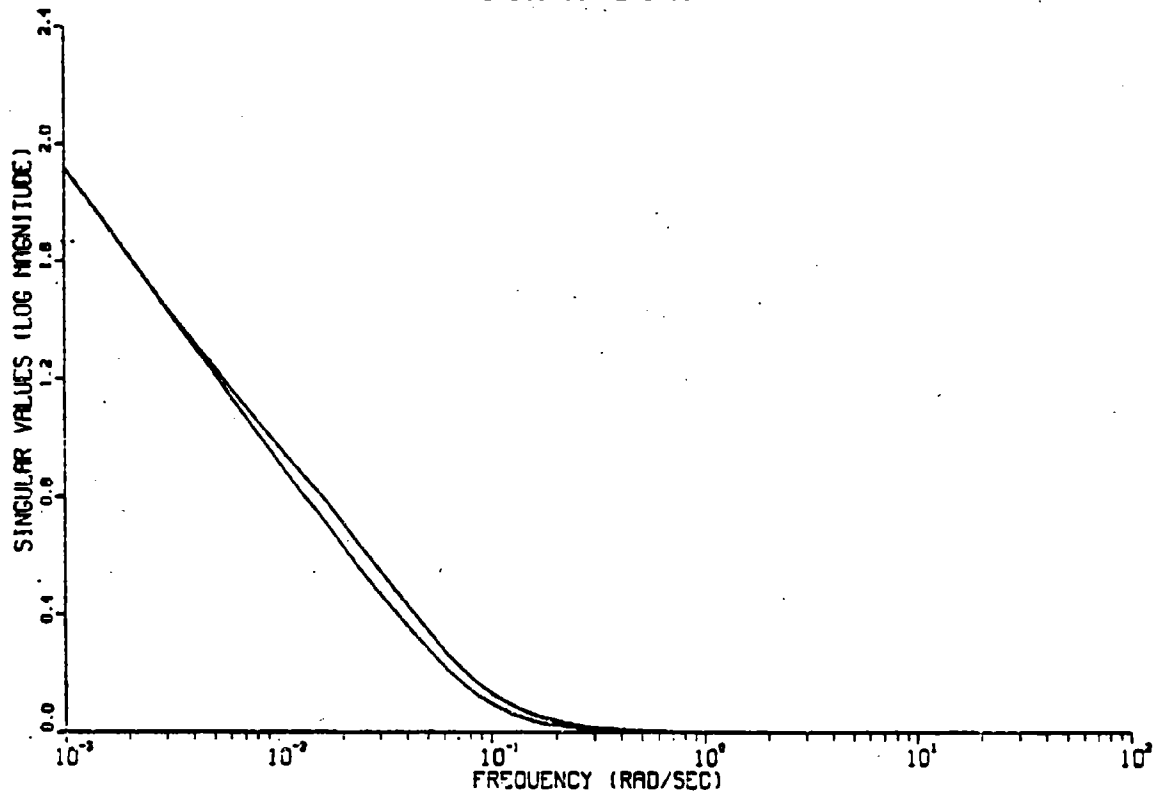


Figure 4-20. Kalman filter return difference,  $\dot{\psi} - \dot{z}$  system; singular values vs frequency.

## CHAPTER 5

### MODEL BASED COMPENSATOR EVALUATION

#### 5.1 Compensator Design Implementation

In this section, the performance of both the  $r - \theta$  and  $\dot{\psi} - \dot{z}$  controllers will be tested on the nonlinear submarine simulation to see how closely the performance specifications are met and to check for instabilities. Note that the linear plant dynamics  $G(s)$  presented in the feedback configuration of Figure 3-4 has been replaced by the nonlinear plant dynamics of the simulation. The states at point 2 of Figure 3.4 are therefore the actual measure of output variables. This means that the error vector,  $e(t)$ , at the input of the Model Based Compensator is always the true difference between the commanded input and the output variables.

In order to avoid the additional computations required to transform the output variables back to their original units, the output variables are handled in their scaled form. To maintain a properly scaled error vector,  $e(t)$ , the true output variables and the command input variables,  $r(t)$ , are multiplied by the appropriate scaling transformation. Figure 5-1 illustrates how the modal based compensator feedback configuration for this design implementation is modified by scaling.

#### 5.2 Evaluation of Output Variable Selection

Comparison of the two system performances will be accomplished in this section to determine which rate control system provides better performance and robustness characteristics. The performance evaluation will be based

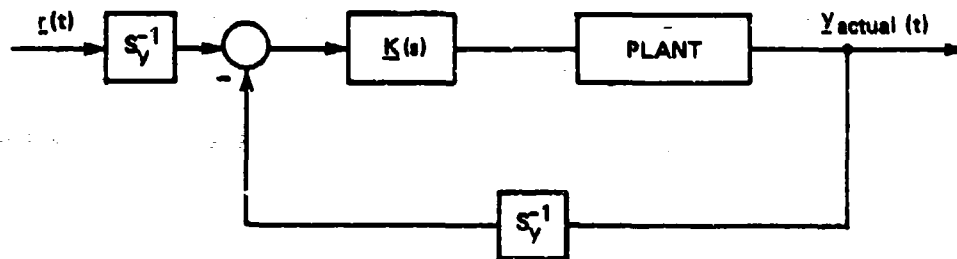


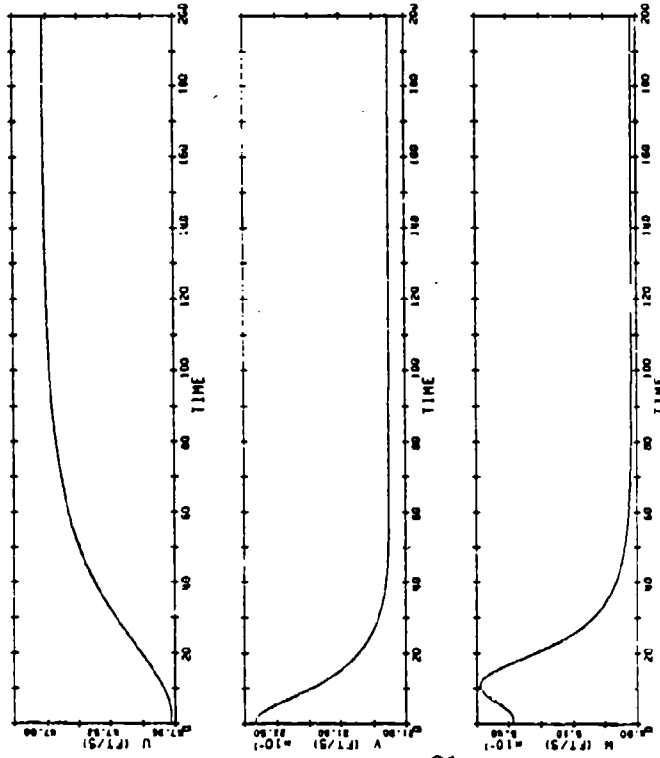
Figure 5-1. Modifications of the MBC feedback configured due to scaling.

on commanding various bearing rates, while ordering zero pitch or zero depth rate to the two compensators. The resulting behavior of the vehicle with respect to depth will then provide a common means of comparing the response of the two designs.

The first simulation run for both controllers is for a small excursion about the nominal point of 1 degree/s and zero feet/s (or zero pitch for the  $r - \theta$  system); it is expected that the nonlinear model should behave linearly in this vicinity and would provide a gauge of how successful the model was in meeting some of the performance specifications. The entire state outputs for the  $\dot{\psi} - \dot{z}$  compensator simulation are found in Figure 5-2. The  $\dot{\psi}$  and  $\dot{z}$  command errors under the control input heading of Figure 5-2 indicate the performance. It can be seen that settling times for both outputs are indeed within 50 - 60 seconds and are in compliance with the performance specifications of Section 2.6. Note also that there is already a small error in  $\dot{z}$  after 60 seconds. This error tends to zero as more time is allowed for the simulation, and results in a maximum vehicle depth change of about 5 feet for this maneuver. The command errors of the  $r - \theta$  compensator shown in Figure 5-3 exhibit nearly the same performance as the  $\dot{\psi} - \dot{z}$  compensator for the heading rate orders, but the  $\theta$  output state experiences a small overshoot. Figure 5-3 also shows that as  $\theta$  approaches the value of zero (level turn), the vehicle depth continues to increase without apparent bounds. This is not a sign of instability, but rather an indication that  $\theta$  is not a very accurate representation of depth rate.

### VELOCITIES

NON-LINEAR SIMULATION Z-PSI



### ANGULAR VELOCITIES

NON-LINEAR SIMULATION Z-PSI

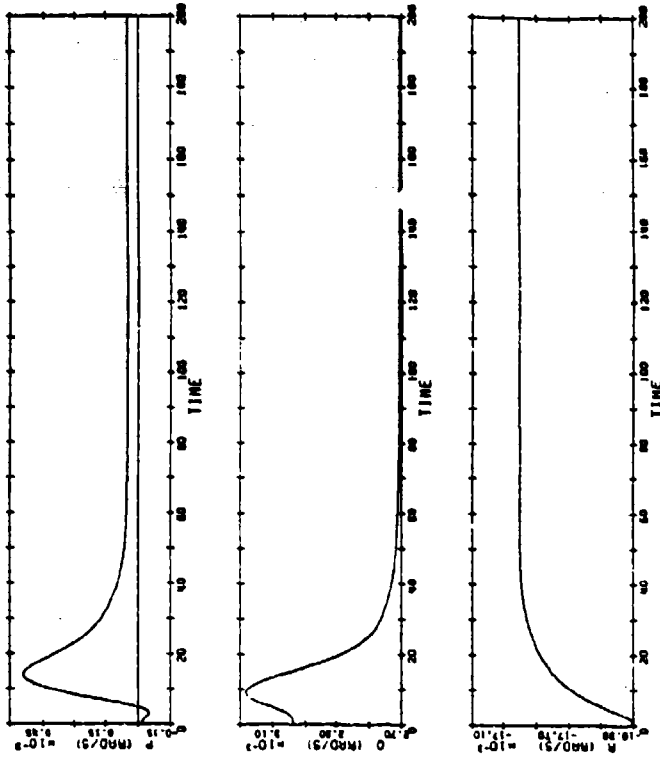
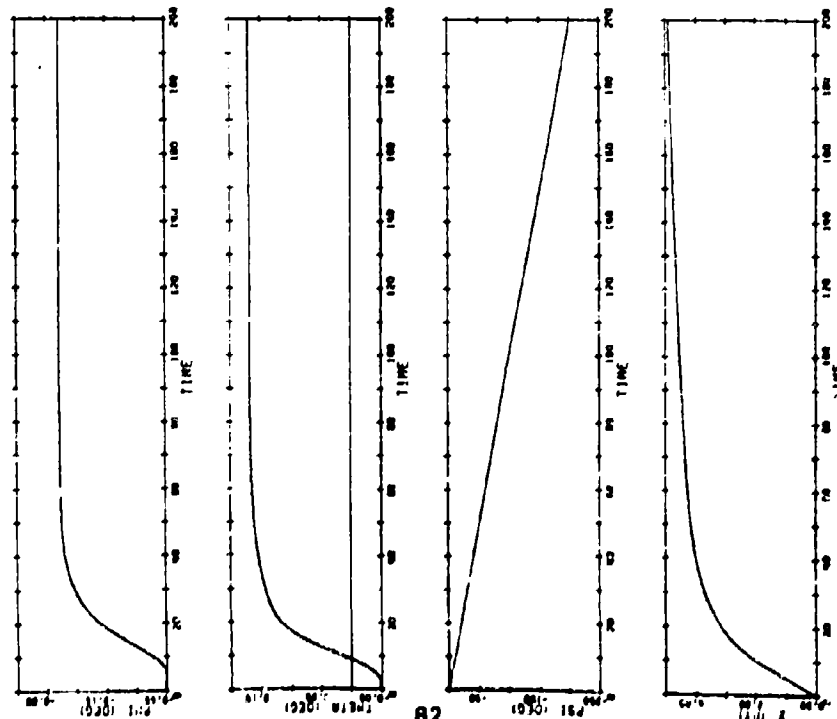


Figure 5-2. Complete nonlinear simulation for  $\dot{\psi} - \dot{z}$  control system in vicinity of nominal point.

ATTITUDE AND DEPTH

NON-LINEAR SIMULATION Z-PSI



OUTPUT ERROR

NON-LINEAR SIMULATION Z-PSI

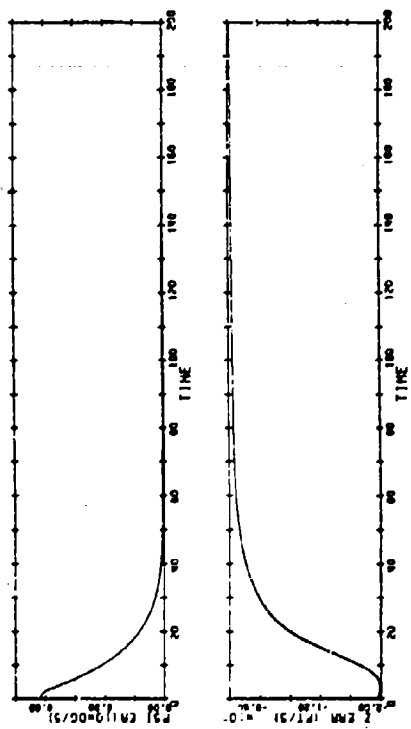


Figure 5-2. Complete nonlinear simulation for  $\dot{\psi} - \dot{z}$  control system in vicinity of nominal point. (Cont.)

CONTROL INPUTS  
NON-LINEAR SIMULATION Z-PSI

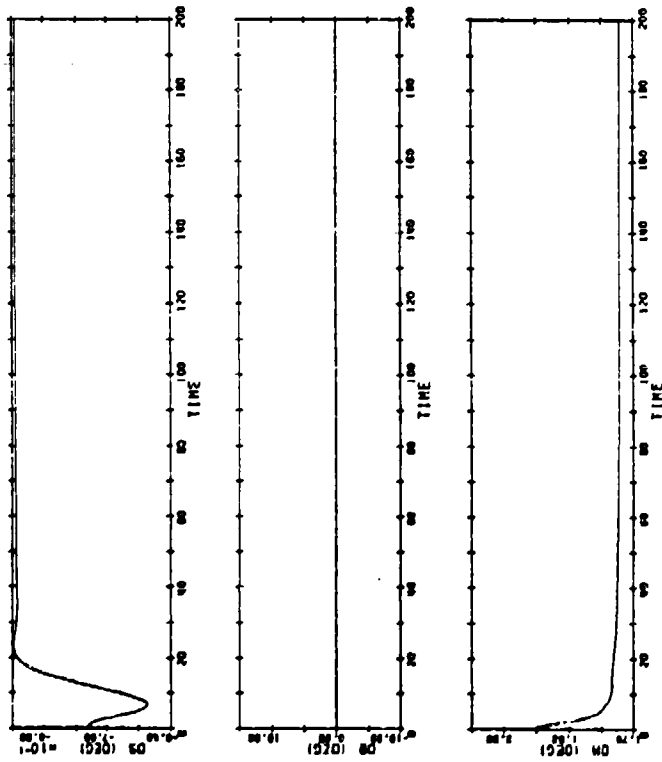


Figure 5-2. Complete nonlinear simulation for  $\dot{\psi} - \dot{z}$  control system in vicinity of nominal point. (Cont.)

NON-LINEAR SIMULATION R-THETA

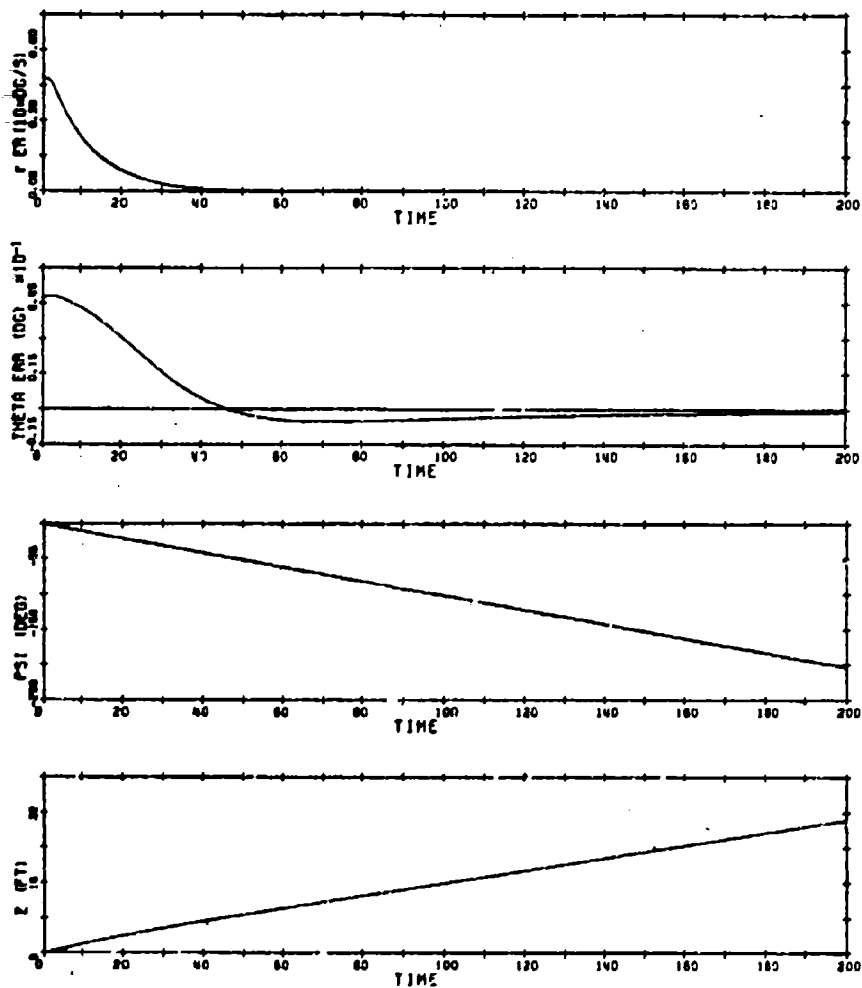


Figure 5-3. Nonlinear simulation showing output error and response for  $r - \theta$  control system in vicinity of nominal point.

When bearing rates were much greater than the nominal rate, the system behaved in a much different fashion. The simulation results in Figures 5-4 are for a commanded bearing rate of 2 degrees/s, or about double the nominal rate. Note here that the time scale has been expanded to 400 seconds. The output error of  $\dot{\psi}$  takes about 120 seconds to settle, while the  $z$  error shows indications of settling in some time greater than 400 seconds. Figure 5-5 demonstrates similar results for the  $r - \theta$  controller; the  $\theta$  error state has nearly the same shape as the  $z$  error state except for a different sign. Note that the dynamics of  $\dot{z}$  and  $\theta$  are rather complicated and certainly not harmonic in nature. This is no doubt caused by the nonlinear behavior of the submarine.

Ordinarily, performance measures are given in the form of settling times, rise times, percent overshoot, etc. These conventional measures cannot be applied exactly (unaltered) in this case due to the nonlinear behavior that would render such indices meaningless or misleading. For instance, a steady-state output error may prolong the measure of system settling time, although the output error may have reached this particular state in a relatively short time.

Quantitative comparisons will be made, instead, through performance indices that are based on an integral error of the form

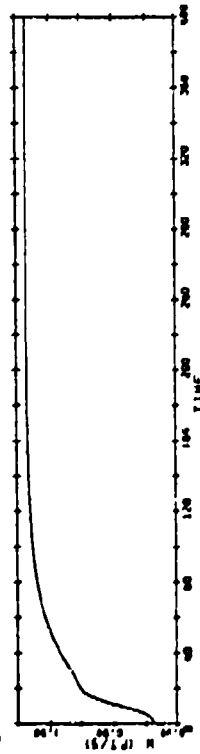
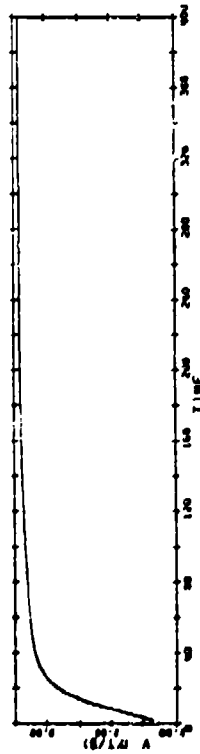
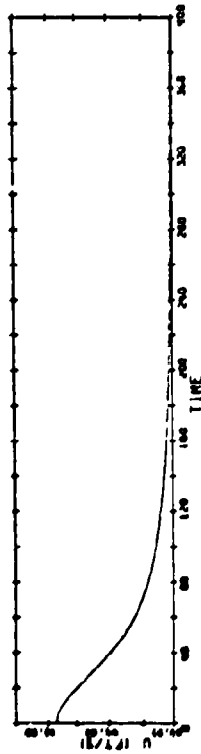
$$P.I. = \int_0^{t_f} \underline{e}(t) dt$$

for a step input of  $\underline{y}_c$ , the commanded output, the integral error becomes

$$P.I. = \underline{y}_c t_f - \int_0^{t_f} \underline{y}(t) dt \quad (5-1)$$

# VELOCITIES

NON-LINEAR SIMULATION Z-PSI



# ANGULAR VELOCITIES

NON-LINEAR SIMULATION Z-PSI

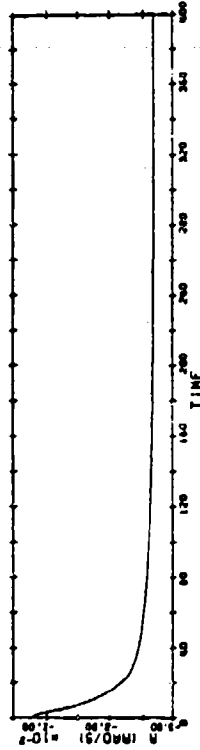
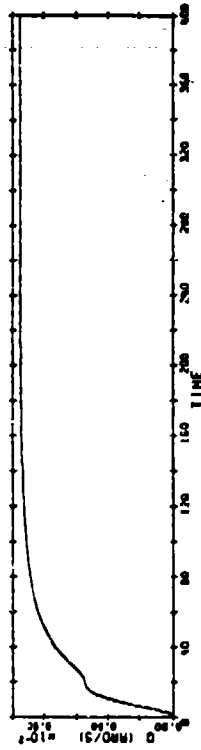
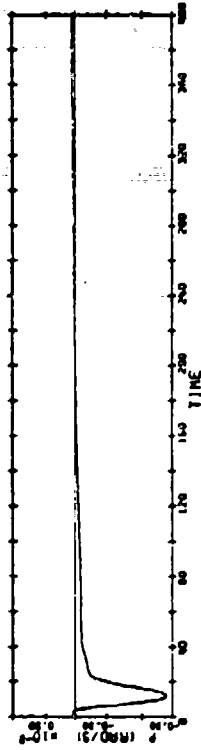
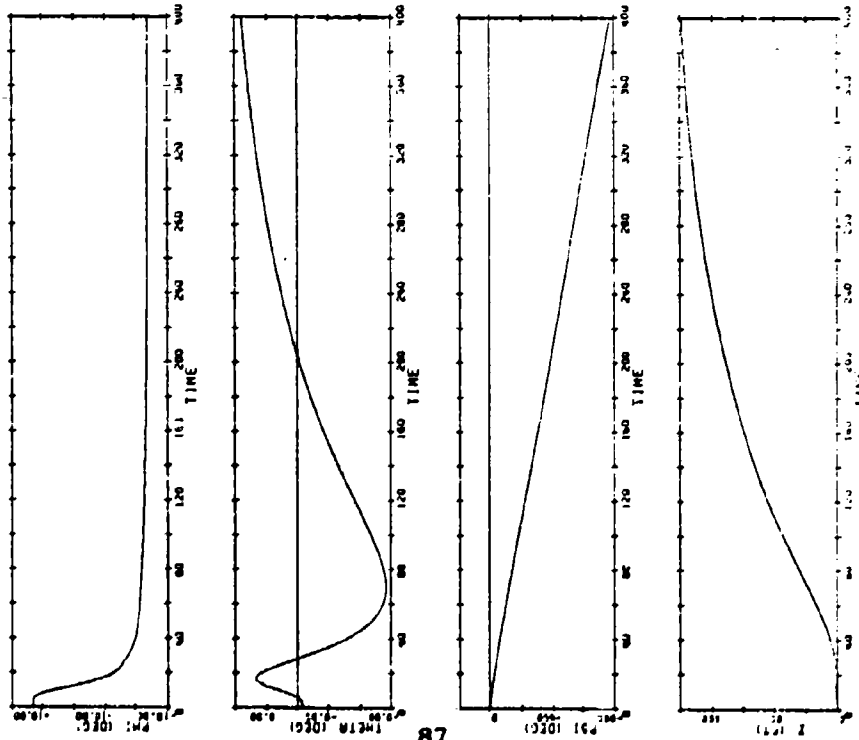


Figure 5-4. Complete nonlinear simulation for  $\dot{\psi} - \dot{z}$  control system away from nominal point.

### ATTITUDE AND DEPTH

NON-LINEAR SIMULATION Z-PSI



### OUTPUT ERROR

NON-LINEAR SIMULATION Z-PSI

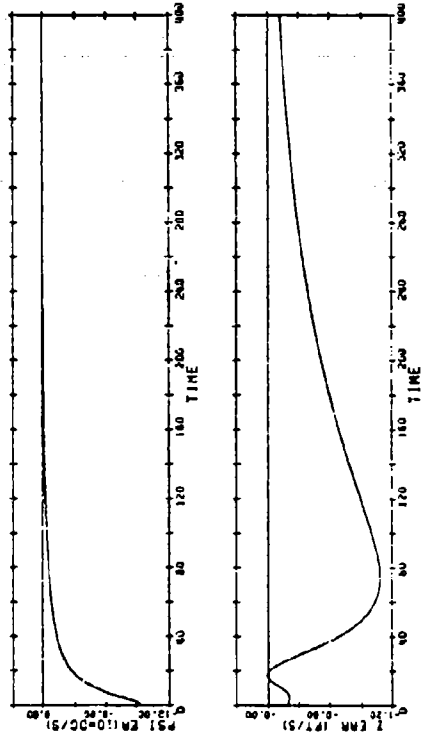


Figure 5-4. Complete nonlinear simulation for  $\dot{\psi} - \dot{z}$  control system away from nominal point. (Cont.)

CONTROL INPUTS  
NON-LINEAR SIMULATION Z-FSI

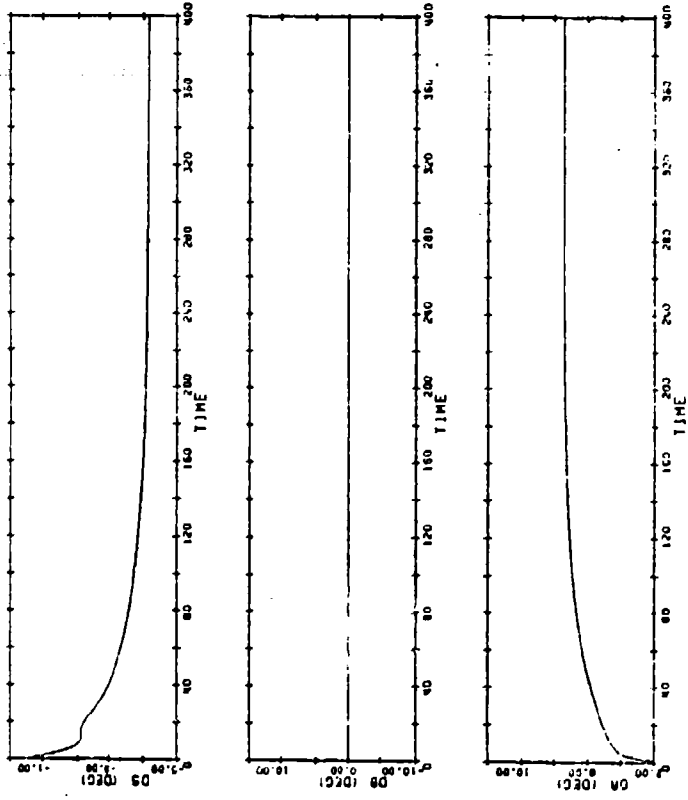


Figure 5-4. Complete nonlinear simulation for  $\dot{\psi} - \dot{z}$  control system away from nominal point. (Cont.)

NON-LINEAR SIMULATION R-THETA

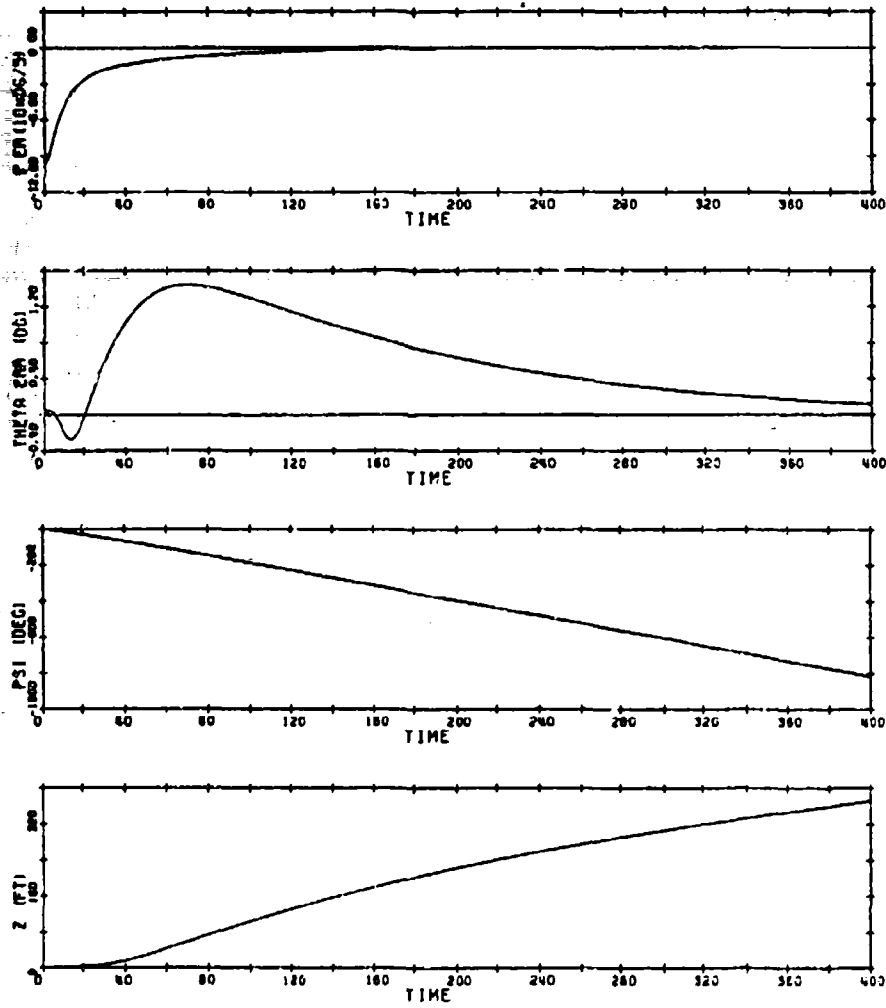


Figure 5-5. Nonlinear simulation showing output error and response for  $r - \theta$  control system away from nominal point.

This is a particularly useful and convenient measure. As it turns out, the change in depth, or depth excursion, in a specified time,  $t_f$ , of a submersible that is commanded to maintain a constant depth is equal to the depth rate integral error. Equation (5-1) will not be applied precisely to the  $r - \theta$  controller; however, the resulting depth excursions and heading errors provide a common means to compare the performance of the two control systems. These results are plotted in Figures 5-6 and 5-7. Figure 5-6 shows no significant differences between either control system's yaw rate integral errors. Several conclusions can be drawn from Figure 5-7, however. Both controllers' performance is best near the nominal point bearing rate (1 degree/s), although it can be seen that the depth excursion of the  $r - \theta$  controller is greater. Again, this is not surprising since  $\theta$  is only a partial description of the full depth expression [(Eq. (2.14))]. For an equal interval of 1 degree/s on either side of the nominal point, the depth excursions of the  $\dot{\psi} - \dot{z}$  controller are nearly symmetrical with respect to the nominal point, whereas the error of the  $r - \theta$  controller is less at lower turning rates. In either case, the controllers provide better depth control than otherwise achievable by manual means, although the rapid increase of depth for commanded turning rates greater than 2 degrees/second or less than 0 degree/second (opposite turn) may be an indication that the system is becoming less stable.

It is very unlikely that a submarine would stay in a maneuver like this for very long since it would have completed a full (360 degree) turn in about 3 minutes. A more realistic operating scenario was simulated. Figure 5-8 shows a series of maneuvers in response to various reference inputs listed in Table 5-1. Which are in the form of fast ramps (1 - 5 seconds). This is to simulate the commands an operator may issue through the "joy-stick" in maneuvering his vehicle. An interesting observation in Figure 5-8 is that commanded changes in  $\theta$  have very little effect on  $r$  as indicated by points 1, 3, and 4; however, the commanded change in  $r$  does have a substantial effect on the error in  $\theta$ , as seen in point 2. Point 5 of Figure 5-8 shows the effect of commanding simultaneous changes in  $r$  and  $\theta$ .

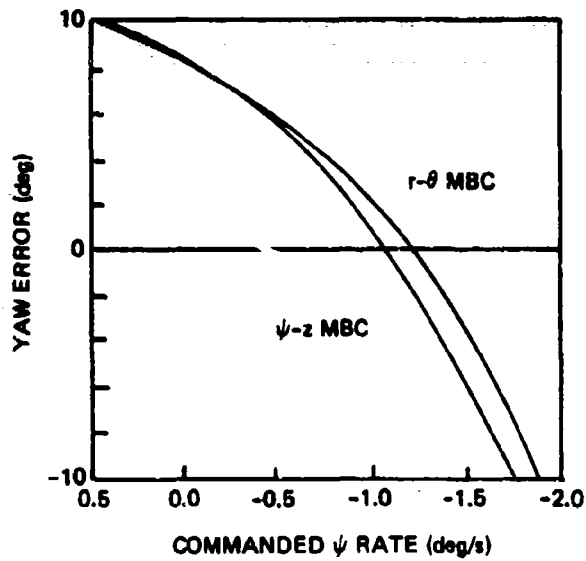


Figure 5-6. Integral yaw error for commanded  $\psi$  rate after 100 seconds.

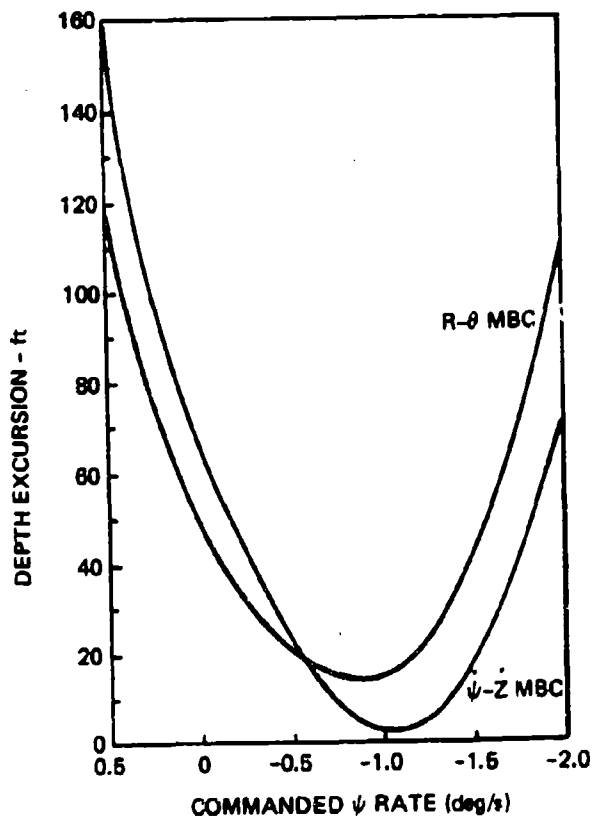


Figure 5-7. Integral depth error for commanded  $\psi$  rate after 100 seconds.

Table 5-1. Nonlinear simulation  $r - \theta$ . Time and the corresponding reference inputs.

Point	TIME SEC	$r$ (10 deg/s)	$\theta$ (deg)
	0.0	-.100000E+02	0.000000E+00
	60.0	-.100000E+02	0.000000E+00
①	61.0	-.100000E+02	0.200000E+01
	100.0	-.100000E+02	0.200000E+01
②	101.0	0.000000E+00	0.200000E+01
	200.0	0.000000E+00	0.200000E+01
③	201.0	0.000000E+00	0.000000E+00
	300.0	0.000000E+00	0.000000E+00
④	305.0	0.000000E+00	0.500000E+01
	375.0	0.000000E+00	0.500000E+01
	380.0	0.000000E+00	0.500000E+01
⑤	440.0	0.000000E+00	0.500000E+01
	445.0	-.150000E+02	0.200000E+01
	500.0	-.150000E+02	0.200000E+01

The full response of the  $\theta - z$  compensator to various command inputs are shown in Appendix C.

### 5.3 Robustness

To determine how close the controller is to being unstable, recall that  $E_{pre}(s)$  was given by

$$E_{pre}(s) = [\tilde{G}(s) - G(s)] \cdot G^{-1}(s) \quad (3-1)$$

It is clear that for this simulation  $G(s)$  above is a function only of the system nonlinearities since the hydrodynamic coefficients remain as predetermined constants. The structure of  $G(s)$ , then, can be found for any operating condition. Note in Figure 5-9 that a commanded  $\dot{\psi}$  of -2 degrees/s corresponds roughly to 8 degrees of rudder. Since this region of controller operation appears to be approaching its performance limit,  $\tilde{G}(s)$  will be determined by linearization of the submarine dynamics about 8 degrees of rudder.

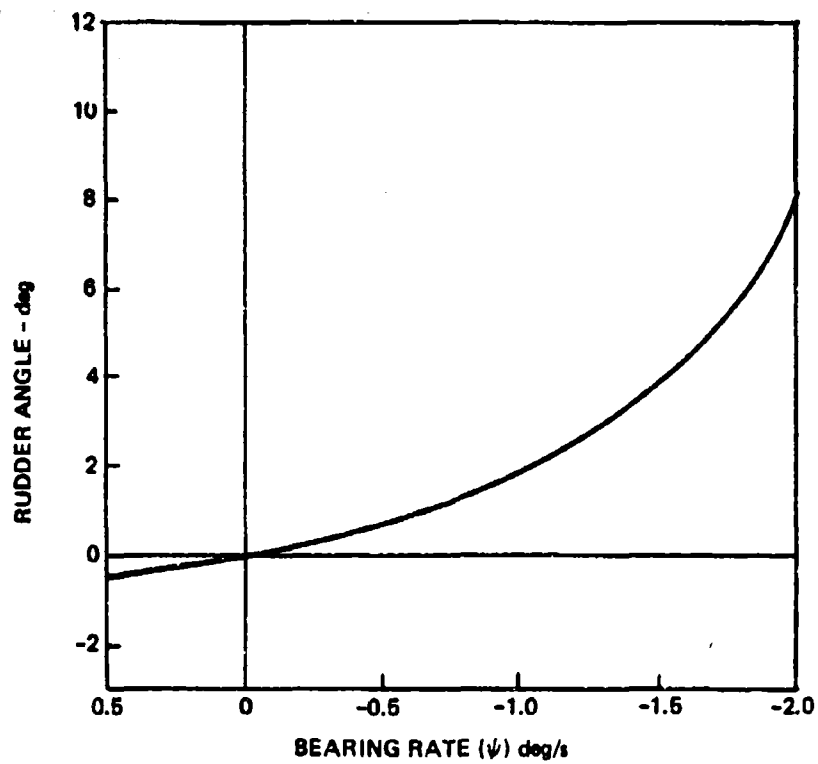


Figure 5.9. Steady state rudder required to achieve commanded bearing rate.

System robustness will then be studied through the inequality

$$\sigma_{\max}[\underline{E}_{\text{pre}}(j\omega)] \leq \sigma_{\min}[\underline{I} + (\underline{G}(j\omega) \underline{K}(j\omega))^{-1}] \quad (3-2)$$

Figures 5-10 and 5-11 provide a graphical interpretation of Eq. (3-2) above. In both instances the maximum singular values of  $\underline{E}_{\text{pre}}(s)$  are equal to, or slightly larger than the minimum singular values of the inverse return difference matrix of the loop-transfer function for the bandwidth up to 0.1 radians/s. Hence the inequality (3-2) above is not satisfied and stability can no longer be guaranteed.

For the  $\dot{\psi} - \dot{z}$  compensator of Figure 5-11 a bulge forms in the singular values of  $\underline{E}_{\text{pre}}(s)$ . This is most likely due to the presence of non-minimum phase zero in the  $\dot{\psi} - \dot{z}$  system since the difference between  $\underline{E}_{\text{pre}}(s)$  of either system can only be attributed to the  $\underline{C}$  matrix used for the outputs. Although the maximum singular value of  $\underline{E}_{\text{pre}}(s)$  is not greater than the singular values of  $(\underline{I} + \underline{T}^{-1}(s))$  near the bulge, it is typically at these higher frequencies and above that other modeling errors (such as unmodeled dynamics) are likely to occur in an actual submarine. The combination of the unmodeled errors in  $\underline{G}(s)$  and the bulge in  $\underline{E}_{\text{pre}}(s)$  for the  $\dot{\psi} - \dot{z}$  controller is more likely to result in an unstable system than, say, relatively flat singular values of  $\underline{E}_{\text{pre}}$  that appears in Figure 5-10.

#### 5.4 Gain Scheduling

Gain scheduling involves the use of more than one set of matched Kalman filter gain matrices ( $\underline{H}$ ) and control gain matrices ( $\underline{G}$ ) to provide the compensator with the ability to extend acceptable performance and robustness requirements over the widest possible range of operating conditions. These operating conditions for the rate controller design can be expressed here in 3-dimensional "volumes". This concept is shown in Figure 5-12. The specification of speed, rudder deflection, and stern plane deflection define a single point. On this diagram, one can plot

$E_{pre}, (1 + T^{-1})$  FOR R-THETA SYSTEM

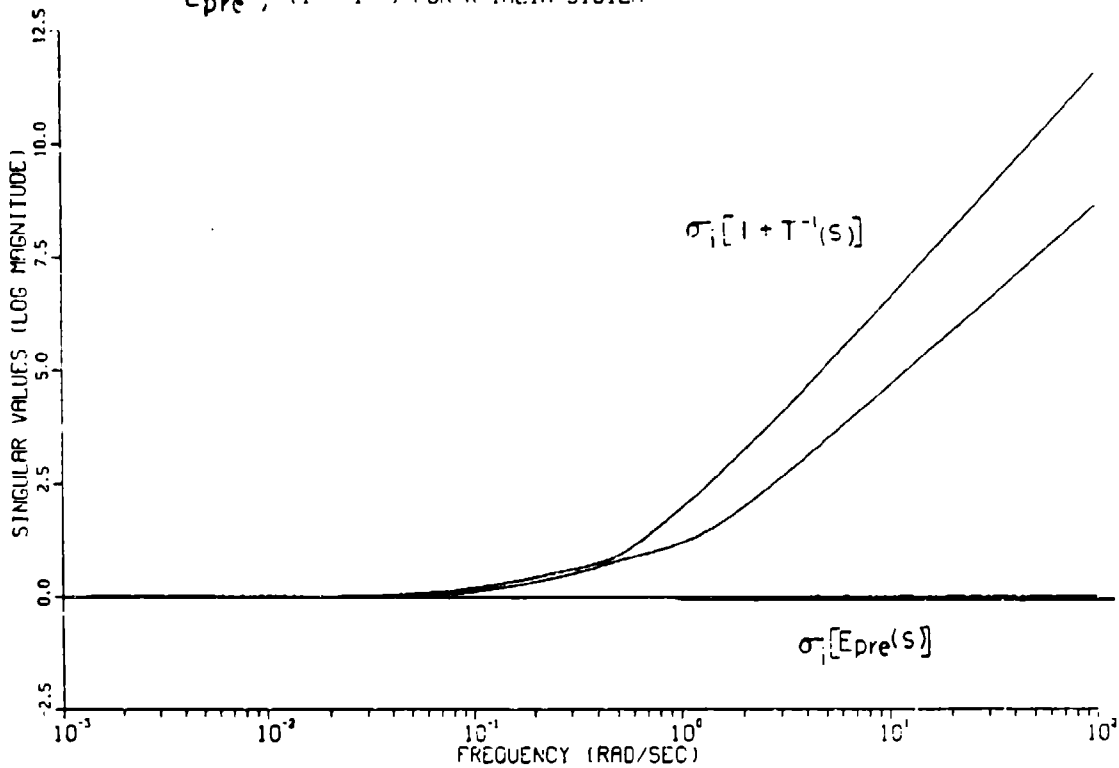


Figure 5-10. Inverse return difference of recovered transfer function and premultiplicative error; r -  $\theta$  system; singular values vs frequency.

$E_{pre}, (1 + T^{-1})$  FOR PSI - Z DCT COMPENSATOR

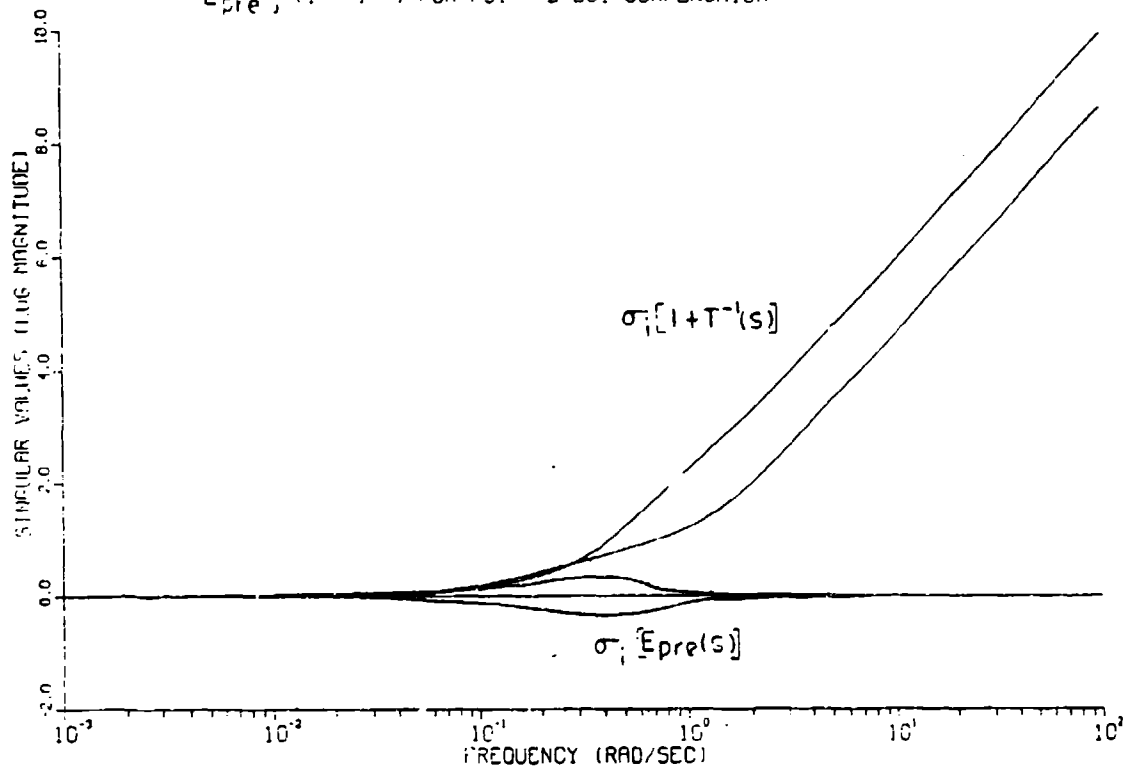


Figure 5-11. Inverse return difference of recovered transfer function and premultiplicative error;  $\psi$  - z system; singular values vs frequency.

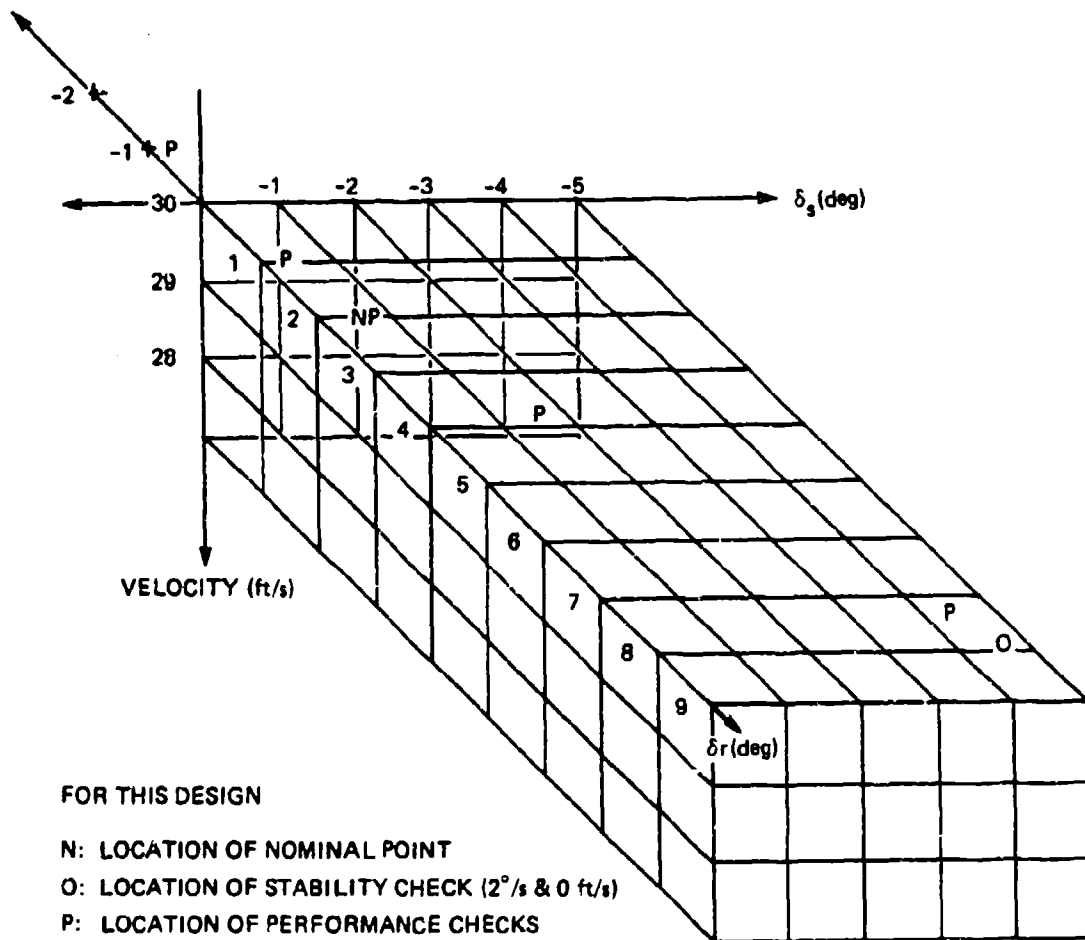


Figure 5.12. Schematic showing operating volume for determination of model robustness and acceptable performance near a nominal point.

regions where, about a nominal point(s), the multiplicative error can be determined and robustness checked in a test similar to Eq. (3-2) above. This is called the region of guaranteed stability. Another volume on the same plot is reserved for performance. It includes all points about the nominal point that result in acceptable performance. The intersection of the stability region and the performance region defines the outer bounds of the operating range of the particular set of gains. Many nominal points together would be required to cover the full possible operating range of the submersible.

Gain scheduling can then be accomplished by two possible approaches:

- (1) Establish large overlapping volumes around nominal points where particular set of gains (including corresponding models of the A, B, and C matrices) are satisfactory with respect to performance and robustness. The shift of gains from one region to another would be through a band-bang implementation. This procedure, of course, requires implementation schemes that would allow the gain shift to occur without violent transients of the control surfaces.
- (2) Select nominal points to span the volume, and schedule the gains of the compensator through a quadratic or least squares fit of the operating conditions through the nominal points. Lively [14] has successfully implemented such a methodology. It becomes difficult, however, to evaluate the robustness by methods used in this thesis. One must somehow ensure that all quadratically obtained gains result in enough robustness to overcome the unmodeled dynamics.

## 5.5 Other Notes

When  $q$ , the control gain weighting index is increased over the value of 10 used in this design, the gain entries of G, of course, increase. The result is that:

- (1) The bandwidth of  $T(s)$  increases slowly to match the crossover of  $G_{KF}$ .
- (2) The control surface deflections for maneuvers similar to those performed in this chapter increased, and tended toward saturation as  $q$  increased further.
- (3) The maximum rate limits of the actuators were exceeded.
- (4) There was no noticeable increase in performance. Therefore, the value of  $q$  was kept as small as possible consistent with meeting the minimum bandwidth requirements.

## 5.6 Chapter Summary

The performance comparisons of and between the two compensator designs are far from complete. It was the intent of this chapter to show how one could begin to evaluate a design; a full evaluation of each controller would require many more calculations to be completed. One might conclude at this point that linearization required to obtain the  $C$  matrix used in the  $\dot{\psi} - \dot{z}$  controller has resulted in a somewhat less robust design. However, the  $\dot{\psi} - \dot{z}$  controller provides more precise control of turning and depth rates which is the ultimate control objective of this design.

The question of robustness away from the nominal point chosen in this design was only partially answered. Nonlinearities most likely provide the greatest source of modeling errors. Other dynamics that arise from errors in the hydrodynamic coefficients and unmodeled dynamics are not known at this time but are required in order to complete the robustness picture before a practical design can be produced for a real submersible.

The control gain matrices for both control systems are found in Appendix B.

## CHAPTER 6

### CONCLUSIONS

#### 6.1 Summary

Multiple-input multiple output control system design methodologies has been successfully employed to provide a means for an operator of a submersible to control heading and depth for complicated maneuvers. This study is far from a completed design. However, results thus far are encouraging. Of significance this thesis has:

- (1) Provided one of few available examples of a complex LQG/LTR Model Based Compensator designs evaluated on a nonlinear simulation.
- (2) Developed a loop-shaping technique, using integrator augmentation in the command input channel, in which singular values can be brought arbitrarily close together and then recovered through natural scaling of the output variables.
- (3) Compared the performance and robustness of rate control designs based on a constant  $\underline{C}$  matrix (the  $r - \theta$  controller) and a linearized  $\underline{C}$  matrix (the  $\dot{\psi} - \dot{z}$  controller). The  $\dot{\psi} - \dot{z}$  controller, which directly controlled the heading rate,  $\dot{\psi}$ , and the depth rate,  $\dot{z}$ , provided better control of the submarine depth in a turn than the  $r - \theta$  controller design. Heading rate control was essentially equal in both designs. However, the linearized  $\underline{C}$  matrix of the  $\dot{\psi} - \dot{z}$  design showed potential for less stability as the vehicle states deviated

from the nominal point. The non-minimum phase zero of the  $\dot{\psi} - \dot{z}$  controller was outside the desired bandwidth and did not effect the loop-transfer recovery process.

## 6.2 Recommendations

Much more work can be done to further provide practical uses of the MIMO LQG-LTR methods used in this thesis and to take a deeper look into achievable submarine performance through rate control systems. Some topics not thoroughly covered in this thesis that could provide a basis for further research include:

- (1) A demonstration of stability and performance as a function of state variable scaling to see if the natural scaling procedures developed in this thesis effect the actual performance bandwidth over unscaled state variables or designs with different scaling methods.
- (2) Determining an error norm that combines both the known errors due to the model deviations from linearity as well as errors that estimate the tolerances of the hydrodynamic coefficients and other modeling errors in order to provide a better picture of the achievable compensator robustness.
- (3) Checking the performance of the model in response to environmental noise.
- (4) Developing a practical method of gain scheduling so the controller provides good performance in all attitudes and speeds.
- (5) Determining how scheduling the sail planes (the  $k$  factor in Eq. (2-11)) effects the performance and stability of the submarine.
- (6) Applying the design procedure used in this thesis to develop control systems for different fin configurations, to possibly include "Y" and "X" sterns, and differential control of a cruciform stern.

#### REFERENCES

- [1] Stein, G., and J. Doyle, "Multivariable Feedback Design Concepts for a Classical/Modern Synthesis," IEEE Trans. Automat. Contr., Vol. AC-26, No. 1, Feb. 1981, pp. 4-16.
- [2] Athans, M., "Multivariable Control Systems," Class Notes, MIT, Spring 1984.
- [3] Abkowitz, M., Stability and Motion Control of Ocean Vehicles, MIT Press, Cambridge, 1969.
- [4] Gertler, M., and G. Hagen, "Standard Equations of Motion for Submarine Simulation," NSRDC Report 2510, 1967.
- [5] Takahashi, Y., Rabins, M., and D. Auslander, Control and Dynamic Systems, Addison-Wesley Publishing Co., Reading, MA, 1972.
- [6] Triantafyllou, M., Bodson, M., and M. Athans, "Real-Time Estimation of Ship Motions Using Kalman Filtering Techniques," IEEE Journal, Vol. OE-8, No. 1, Jan. 1983.
- [7] Lehtomaki, N., "Practical Robustness Measures in Multivariable Control System Analysis," Ph.D. Thesis, MIT, 1981.
- [8] Boettcher, K., "Analysis of Multivariable Control Systems with Structural Uncertainty," Ph.D. Dissertation, MIT, 1983.
- [9] Kappos, E., "Robust Multivariable Control for the F-100 Engine," Engineers Thesis, MIT, 1983.
- [11] Athans, M., "The Role and Use of the Stochastic Linear-Quadratic-Gaussian Problem in Control System Design," IEEE Trans. Automat. Contr., Vol. AC-16, No. 6, Dec. 1971, pp. 279-286.
- [12] Kwakernaak, H., "Optimal Low-Sensitivity Linear Feedback Systems," Automatica, 5, 1959, pp. 279-286.

APPENDIX A

Table A-1. Dynamical response terms (Abkowitz).

1. Body Properties

Length  
 Geometry  
 Mass  
 Moments of Inertia

2. Properties of Motion

Orientation

$x_0, y_0, z_0$  fixed coordinate system, reference at surface  
 $\phi, \theta, \psi$  angular rotations about the x, y, and z axis, respectively

Body Motion

$\vec{U}$  linear velocity vector  
 $\vec{\Omega}$  angular velocity  
 $\dot{\vec{U}}$  linear acceleration vector  
 $\dot{\vec{\Omega}}$  angular acceleration  
 $\delta$  control surface deflection  
 $\dot{\delta}$  control surface velocity  
 $\ddot{\delta}$  control surface acceleration  
 $n$  propeller angular velocity  
 $\dot{n}$  propeller angular acceleration

3. Fluid Properties

$\rho$	mass density of fluid	$g$	acceleration of fluid
$\mu$	viscosity	$p$	pressure of fluid
$\tau$	surface tension	$P_v$	vapor pressure of fluid
		$E$	elasticity of fluid

## A.2 Nonlinear Equations of Motion

### Explanation of Conventions used in Hydrodynamic Coefficients

Hydrodynamic coefficients used in the nonlinear and linear equations of motion are generally written in the form

$$X_{ab\dots}$$

where  $X$  represents a force or moment and the subscripts  $a, b, \dots$  represent an angular velocity, linear velocity, rudder deflection, etc. The conventional meaning of coefficients written in this form is

$$X_{ab\dots} = \frac{\partial}{\partial (a, b\dots)} [X]$$

which are taken to be Taylor expansion coefficients.

Moments of inertia are written in similar form, but all subscripts following retain the usual meaning of coordinate system.

1. SURGE

$$m(\dot{u} + qv - rv - x_G(q^2 + r^2) + y_G(pq - \dot{r}) + z_G(pr + \dot{q})) =$$

$$\frac{\rho}{2} l^4 [x_{qq} q^2 + x_{rr} r^2 + x_{rp} rp]$$

$$+ \frac{\rho}{2} l^3 [x_u \dot{u} + x_{vr} vr + x_{wq} wq] + \frac{\rho}{2} l^2 [x_{uu} u^2 + x_{vv} v^2 + x_{ww} w^2] +$$

$$+ \frac{\rho}{2} l^2 u^2 [x_{\delta r \delta r} \delta r^2 + x_{\delta s \delta s} \delta s^2 + x_{\delta b \delta b} \delta b^2] + (\text{PROPTH} - \text{DRAG})$$

$$+ \frac{\rho}{2} l^{-(n-1)} [x_{vvn} v^2 + x_{wvn} w^2 + x_{\delta r \delta r n} u^2 n \delta r^2 + x_{\delta s \delta s n} u^2 n \delta s^2]$$

$$- \text{WTOT} \sin \theta$$

$$\text{PROPTH} - \text{DRAG} = u^2 (c_1 n^2 + b_1 n + a_1)$$

2. SWAY

$$\begin{aligned}
 m[\dot{v} - pw + ur - y_G(\dot{r}^2 + p^2) + z_G(q\dot{r} - \dot{p}) + x_G(qp + \dot{r})] = \\
 \frac{\rho}{2} l^4 [Y_r \dot{r} + Y_p \dot{p} + Y_p |p| |p| + Y_{pq} pq + Y_{qr} qr + Y_{rv} \text{sign}(r, v) \sqrt{v^2 + w^2}] \\
 + \frac{\rho}{2} l^3 [Y_{wp} wp + Y_r ur + Y_p up + Y_{|r|} |r| u |r| \delta r] + \\
 + \frac{\rho}{2} l^2 [Y_x u^2 + Y_v uv + Y_{|v|} |v| w \sqrt{v^2 + w^2} + Y_{\delta r} u^2 \delta r + \\
 + Y_{vw} vw u / \sqrt{u^2 + v^2 + w^2}] + WTOT \sin \phi \cos \theta + \\
 + (n-1) \left\{ \frac{\rho}{2} l^3 Y_{rn} ur + \frac{\rho}{2} l^2 Y_{vn} uv + \frac{\rho}{2} l^2 Y_{\delta rn} u^2 \delta r + \right. \\
 \left. + \frac{\rho}{2} l^2 Y_{|r|n} |r| w \sqrt{v^2 + w^2} \right\} + Y_{CRFL} + Y_{VTX}^*
 \end{aligned}$$

$$Y_{CRFL} = \left\{ \frac{\rho}{2} (-l^2 \frac{Zw}{\int_l D(x) dx} \right\} \int_l H(x) v(x) \sqrt{v^2(x) + w^2(x)} dx$$

$$Y_{VTX}^* = \left\{ \frac{\rho}{2} l^2 \frac{Zv}{(\bar{x}_{fw} - x_{so})} \right\} \int_{x_{vs}}^{x_{fw}} w(x) \bar{v}_{fw}(t - \tau_x) dx ; \text{ not included in IBM program.}$$

$$\text{sign}(r, v) \triangleq r \cdot \frac{v}{|v|}$$

$\tau_x$ : time it took vehicle to travel a distance  $x$  in the axial direction

3. HEAVE

$$\begin{aligned}
 & m[\dot{w} + v\dot{p} - u\dot{q} - z_G(p^2 + q^2) + x_G(rp - \dot{q}) + y_G(rp + \dot{p})] = \\
 & \frac{\rho}{2} l^4 [z_{qq}\dot{q} + (z_{rr}r^2 + z_{rp}rp) \frac{u}{\sqrt{u^2 + v^2 + w^2}}] + \\
 & + \frac{\rho}{2} l^3 [z_{vw}\dot{v} + z_{vr}vr \frac{u}{\sqrt{u^2 + v^2 + w^2}} + z_w|q| \frac{w}{|w|} \sqrt{v^2 + w^2} |q| + \\
 & + z_q uq + z_{|q|} u|q|\delta s] + \\
 & + \frac{\rho}{2} l^2 [z_{vp} \frac{u}{\sqrt{u^2 + v^2 + w^2}} vp + z_u u^2 + z_{vv} \frac{v^2 u}{\sqrt{u^2 + v^2 + w^2}} + \\
 & + z_w|w| \sqrt{v^2 + w^2} w + z_w uw + z_{\delta s} u^2 \delta s + z_{\delta b} u^2 \delta b + z_{|w|} u|w| + \\
 & + z_{ww}|w| \sqrt{v^2 + w^2}] + WTOT \cos \phi \cos \theta + \\
 & + (\eta - 1) \left\{ \frac{\rho}{2} l^3 z_{qn} uq + \frac{\rho}{2} l^2 z_{wn} uw + \frac{\rho}{2} l^2 z_w|w| \eta w \sqrt{v^2 + w^2} + \right. \\
 & \left. + \frac{\rho}{2} l^2 z_{\delta sn} u^2 \delta s \right\} + z_{CRFL} + z_{VTX}^*
 \end{aligned}$$

$$z_{CRFL} = -\frac{\rho}{2} \int_l C_d D(x) w(x) \sqrt{v^2(x) + w^2(x)} dx$$

$$z_{VTX}^* = \frac{\rho}{2} l C_y \int_{x_{vs}}^{\bar{x}_{fv}} v(x) v_{fv}(t - \tau_x) dx ; \text{ not included in the IBM program.}$$

4. ROLLING TORQUE ( $\phi$ )

$$\begin{aligned}
 & I_x \dot{p} + (I_z - I_y)qr - (\dot{r} + pq)I_{xz} + (r^2 - q^2)I_{yz} + (pr - \dot{q})I_{xy} + \\
 & m(y_G(\dot{w} - uq + vp) - z_G(\dot{v} - wp + ur)) = \\
 & \frac{\rho}{2} l^5 [K_p \dot{p} + K_r \dot{r} + K_p |p| |p| + K_{qr} qr + K_{pq} pq] + \\
 & + \frac{\rho}{2} l^4 [K_v \dot{v} + K_r ur + K_p up] + \\
 & + \frac{\rho}{2} l^3 [K_u u^2 + K_v uv + K_v |v| \sqrt{v^2 + w^2} + K_{\delta r} u^2 \delta r + K_{vw} vw + \\
 & + (n-1)K_{\eta} u^2] \\
 & - (z_G^{WTOT} - z_B) \cos \theta \sin \phi + (y_G^{WTOT} - y_B) \cos \theta \cos \phi + \\
 & + [u^2 + v_c^2 + w_c^2] [k_{4t} \beta_c^2 \sin 4\phi_c + k_{8t} \beta_c^2 \sin 8\phi_c] + \\
 & + \frac{\rho}{2} l C_v \bar{z} \int_{x_{vs}}^{\bar{x}_{fw}} w(x) \bar{v}_w(t - \tau_x) dx
 \end{aligned}$$

$$v_c = v + x_c r$$

$$w_c = w - x_c q$$

$$\phi_c = \tan^{-1} \left( -\frac{w_c}{v_c} \right)$$

$$\beta_c = \tan^{-1} \sqrt{v_c^2 + w_c^2} / u$$

5. PITCHING TORQUE ( $\theta$ )

$$\begin{aligned}
 & I_y \dot{q} + (I_x - I_z)rp - (\dot{p} + qr)I_{xy} + (p^2 - r^2)I_{zx} + (qp - \dot{r})I_{yz} + \\
 & + m[z_G(\dot{u} - vr + wq) - z_G(\dot{w} - uq + vp)] = \\
 & = \frac{\rho}{2} l^5 \left[ M_q \dot{q} + M_{rr} r^2 \frac{u}{\sqrt{u^2 + v^2 + w^2}} \right] + \\
 & + \frac{\rho}{2} l^4 \left[ M_w \dot{v} + M_{|w|q} q \sqrt{v^2 + w^2} + M_q uq + M_{|q|} \delta s u |q| \delta s \right] + \\
 & + \frac{\rho}{2} l^3 \left[ M_u u^2 + M_{\delta s} v^2 \frac{u}{\sqrt{u^2 + v^2 + w^2}} + M_{|w|} w \sqrt{v^2 + w^2} + M_{|w|} u |w| + \right. \\
 & \quad \left. + M_{\delta s} u^2 \delta s + M_{\delta b} u^2 \delta b + M_{|w|} u |w| + M_{|w|} |w| \sqrt{v^2 + w^2} \right] \\
 & - (z_G^{WTOT} - z_B) \sin \theta - (x_G^{WTOT} - x_B) \cos \theta \sin \phi \\
 & + (\eta - 1) \left[ \frac{\rho}{2} l^4 M_{qn} uq + \frac{\rho}{2} l^3 M_{wn} uw + \frac{\rho}{2} l^3 M_{|w|\eta} w \sqrt{v^2 + w^2} + M_{\delta s \eta} u^2 \delta s \right] \\
 & + M_{CRFL} + M_{VTX}^*
 \end{aligned}$$

$$M_{CRFL} = \frac{\rho}{2} \int_l C_d x D(x) w(x) \sqrt{v^2(x) + w^2(x)} dx$$

$$M_{VTX}^* = -\frac{\rho}{2} l C_v \int_{x_{vs}}^{\bar{x}_{fw}} x v(x) \ddot{v}_w(t - \tau_x) dx ; \text{ not included in IBM.}$$

6. YAWING TORQUE ( $\psi$ )

$$\begin{aligned}
 & I_z \dot{r} + (I_y - I_x) p q - (\dot{q} + r p) I_{yz} + (q^2 - p^2) I_{xy} + (r p - \dot{p}) I_{zx} + \\
 & + [x_G (\dot{v} - w p + u r) - y_G (\dot{u} - v r + w q)] = \\
 & \frac{\rho}{2} \ell^5 [N_r \dot{r} + N_p \dot{p} + N_{qr} q r + N_r |r| |r| + N_{pq} p q] + \\
 & + \frac{\rho}{2} \ell^4 [N_v |v| r \sqrt{v^2 + w^2} + N_{wp} w p + N_r u r + N_p u p + N_v \dot{v} + N_r |\delta r| |r| \delta r] + \\
 & + \frac{\rho}{2} \ell^3 [N_u u^2 + N_v |v| w \sqrt{v^2 + w^2} + N_v u v + N_{vw} \frac{v w u}{\sqrt{u^2 + v^2 + w^2}}] + \\
 & + (n-1) \left[ \frac{\rho}{2} \ell^4 N_{rn} u r + \frac{\rho}{2} \ell^3 N_{vn} u v + \frac{\rho}{2} \ell^3 N_v |v| n w \sqrt{v^2 + w^2} + \right. \\
 & \quad \left. + \frac{\rho}{2} \ell^3 N_{\delta rn} u^2 \delta r \right] \\
 & + (x_G^{WTOT} - x_B) \cos \theta \sin \phi + (y_G^{WTOT} - y_B) \sin \theta + N_{CRFL} + W_{VTX}^*
 \end{aligned}$$

$$N_{CRFL} = -\frac{\rho}{2} C_{dy} \int_{\ell} x H(x) v(x) \sqrt{v^2(x) + w^2(x)} dx$$

$$N_{VTX}^* = -\frac{\rho}{2} \ell C_v \int_{x_{vs}}^{\bar{x}_{vw}} x w(x) \bar{v} \bar{v}_w (t - \tau_x) dx ; \text{ not included in IBM}$$

### KINEMATIC RELATIONS

$$U^2 = u^2 + v^2 + w^2$$

$$\dot{z}_0 = -u \sin \theta + v \cos \theta \sin \phi + w \cos \theta \cos \phi$$

$$\dot{\phi} = p + \dot{\psi} \sin \theta$$

$$\dot{\theta} = \frac{q - \dot{\psi} \cos \theta \sin \phi}{\cos \phi}$$

$$\dot{\psi} = \frac{r + \dot{\theta} \sin \phi}{\cos \theta \cos \phi}$$

### A.3 Parametric Linearization

#### I. AXIAL FORCE (SURGE)

$$\begin{aligned}
 (m - \lambda_1)\Delta\dot{u} - m y_G \Delta\dot{r} + m z_G \Delta\dot{q} = & \\
 = \Delta u [2u_0 \{X_{uu} + a_1 + b_1 \eta + c_1 \eta^2 + X_{\delta r \delta r} \delta r^2 + X_{\delta s \delta s} \delta s^2 + & \\
 + X_{\delta b \delta b} \delta b^2 + (\eta_0 - 1)(X_{\delta r \delta r \eta} \delta r^2 + X_{\delta s \delta s \eta} \delta s^2)\}] + & \\
 + \Delta v [2(X_{vv} + (\eta_0 - 1)X_{v\eta})v_0 + (X_{vr} + m)r_0] + & \\
 + \Delta w [2(X_{ww} + (\eta_0 - 1)X_{w\eta})w_0 + (X_{wq} - m)q_0] + & \\
 + \Delta p [-m y_G q_0 - (m z_G - X_{rp})r_0] + & \\
 + \Delta q [(X_{wq} - m)w_0 - m y_G p_0 + 2(m x_G + X_{qq})q_0] + & \\
 + \Delta r [(X_{vr} + m)v_0 + (X_{rp} - m z_G)p_0 + 2(m x_G + X_{rr})r_0] & \\
 - \Delta \theta [(W_{TOT} - B) \cos \theta_0] & \\
 + \Delta \delta s [2(X_{\delta s \delta s} + X_{\delta s \delta s \eta} (\eta_0 - 1))\delta s_0 u_0^2] & \\
 + \Delta \delta b [2X_{\delta b \delta b} u_0^2 \delta b_0] & \\
 + \Delta \delta r [2(X_{\delta r \delta r} + X_{\delta r \delta r \eta} (\eta_0 - 1))\delta r_0 u_0^2] & \\
 + \Delta \eta [u_0^2 (b_1 + 2c_1 \eta_0) + X_{v\eta} v_0^2 + X_{w\eta} w_0^2 & \\
 + (X_{\delta s \delta s \eta} \delta s_0^2 + X_{\delta r \delta r \eta} \delta r_0^2) u_0^2] &
 \end{aligned}$$

## II. LATERAL FORCE

$$\begin{aligned}
 & (m - Y_v) \Delta \dot{v} - (mz_G + Y_p) \Delta \dot{p} + (mx_G - Y_r) \Delta \dot{r} = \\
 & \Delta u \left[ 2u_0 \left\{ Y_u + Y_{\delta r} \delta r + (\eta_0 - 1) Y_{\delta r n} \delta r - \frac{1}{2} \frac{Y_{vw} u_0 v_0 w_0}{(u_0^2 + v_0^2 + w_0^2)^{3/2}} \right\} + \right. \\
 & \quad \left. + v_0 \left\{ Y_v + (\eta_0 - 1) Y_{vn} + \frac{Y_{vw} w_0}{\sqrt{u_0^2 + v_0^2 + w_0^2}} \right\} + Y_p p_0 + \right. \\
 & \quad \left. + r_0 \left\{ (Y_r - m) + Y_{|r|} \delta r \frac{|r_0|}{r_0} \delta r + (\eta_0 - 1) Y_{rn} \right\} + \right. \\
 & \quad \left. + \Delta v \left[ u_0 \left\{ Y_v + \frac{Y_{vw} w_0}{\sqrt{u_0^2 + v_0^2 + w_0^2}} \left( 1 - \frac{v_0^2}{u_0^2 + v_0^2 + w_0^2} \right) + (\eta_0 - 1) Y_{vn} + \right. \right. \right. \\
 & \quad \left. \left. + v_0 \left( \frac{Y_v |r| \frac{|r_0|}{v_0}}{\sqrt{v_0^2 + w_0^2}} + (Y_v |v| + (\eta_0 - 1) Y_v |v| \eta) \cdot \left( 1 + \frac{w_0^2}{v_0^2} + \frac{v_0}{\sqrt{v_0^2 + w_0^2}} \right) v_0 \right) \right. \right. \\
 & \quad \left. \left. + Y_{vq} q_0 + \frac{\partial Y_{CRFW}}{\partial v} \right] \right. \\
 & \quad \left. + \Delta w \left[ u_0 \left\{ \frac{Y_{vw} v_0}{\sqrt{u_0^2 + v_0^2 + w_0^2}} \left( 1 - \frac{w_0^2}{u_0^2 + v_0^2 + w_0^2} \right) \right\} + \right. \right. \\
 & \quad \left. \left. + v_0 \left\{ \frac{w_0}{\sqrt{v_0^2 + w_0^2}} \left( Y_v |r| \frac{|r_0|}{v_0} + Y_v |v| + (\eta_0 - 1) Y_v |v| \eta \right) \right\} \right. \right. \\
 & \quad \left. \left. + p_0 \left\{ Y_{wp} + m \right\} + Y_{wr} r_0 + p_0 m + \frac{\partial Y_{CRFW}}{\partial w} \right] \right. +
 \end{aligned}$$

$$\begin{aligned}
& + \Delta p \left[ u_o Y_p + w_o (Y_{wp} + m) + p_o (2my_G + 2 \frac{|p_o|}{p_o} Y_p |p|) + q_o (Y_{pq} - mx_g) \right] + \\
& + \Delta q \left[ Y_{vq} v_o + p_o (Y_{pq} - mx_g) + r_o (Y_{qr} - mx_g) + \frac{\partial Y_{CRFW}}{\partial q} \right]^* + \\
& + \Delta r \left[ u_o \left\{ (Y_r - m) + 2Y_r \left| \frac{r_o}{r_o} \right| \delta r + Y_{rn} (\eta_o - 1) \right\} + v_o \left\{ Y_v \left| \frac{r_o}{v_o} \right| \right. \right. \\
& \quad \left. \left. + \frac{1}{r_o} \sqrt{v_o^2 + w_o^2} \right\} + Y_{wr} w_o + q_o (Y_{qr} - mx_g) + r_o \cdot 2my_G + \frac{\partial Y_{CRFW}}{\partial r} \right]^* + \\
& + \Delta \phi \left[ (WTOT - B) \cos \theta_o \cos \phi_o \right] \\
& + \Delta \theta \left[ -(WTOT - B) \sin \theta_o \sin \phi_o \right] \\
& + \Delta \delta r \left[ Y_r \left| \delta r u_o \right| r_o + \{ Y_{\delta r} + (\eta_o - 1) Y_{\delta rn} \} u_o^2 \right] \\
& + \Delta \eta \left[ Y_{rn} u_o r_o + Y_{vn} u_o v_o + Y_r \left| v_o \sqrt{v_o^2 + w_o^2} + Y_{\delta rn} u_o^2 \delta r_o \right. \right]
\end{aligned}$$

where:

$$\frac{\partial Y_{CRFW}}{\partial v} \Big|_* = \frac{\rho}{2} \left( -l^2 \frac{z_{ww}}{\int_l D(x) dx} \right) \int_l H(x) \frac{(w_o^2(x) + 2v_o^2(x))}{\sqrt{v_o^2(x) + w_o^2(x)}} dx$$

$$\frac{\partial Y_{CRFW}}{\partial w} \Big|_* = \frac{\rho}{2} \left( -l^2 \frac{z_{ww}}{\int_l D(x) dx} \right) \int_l H(x) \frac{v_o(x) w_o(x)}{\sqrt{v_o^2(x) + w_o^2(x)}} dx$$

$$\frac{\partial Y_{CRFW}}{\partial q} \Big|_* = \frac{\rho}{2} \left( l^2 \frac{z_{ww}}{\int_l D(x) dx} \right) \int_l x \frac{H(x) v_o(x) w_o(x)}{\sqrt{v_o^2(x) + w_o^2(x)}} dx$$

$$\frac{\partial Y_{CRFW}}{\partial r} \Big|_* = \frac{\rho}{2} \left( -l^2 \frac{z_{ww}}{\int_l D(x) dx} \right) \int_l x H(x) \frac{(2v_o^2(x) + w_o^2(x))}{\sqrt{v_o^2(x) + w_o^2(x)}} dx$$

### III. Normal Force (Heave)

$$\begin{aligned}
 & (m - Z_w^*) \Delta \dot{w} + m y_G \Delta \dot{p} - (Z_q^* + m x_G) \Delta \dot{q} \\
 & = \Delta u \left[ 2u_0 \{ z_{\delta s} \delta s + z_{\delta b} \delta b + z_* + (\eta_0 - 1) z_{\delta s \eta} \delta s \} + \right. \\
 & \quad + v_0 \{ (z_{vv} v_0 + z_{vp} p_0 + z_{vr} r_0) \left( \frac{1}{\sqrt{u_0^2 + v_0^2 + w_0^2}} - \frac{u_0^2}{(u_0^2 + v_0^2 + w_0^2)^{3/2}} \right) \} + \\
 & \quad + w_0 \{ z_w + z|w| \frac{|w_0|}{w_0} + (\eta_0 - 1) z_{w \eta} \} + \\
 & \quad + p_0 \{ (z_{pp} p_0 + z_{rp} r_0) \left( \frac{1}{\sqrt{u_0^2 + v_0^2 + w_0^2}} - \frac{u_0^2}{(u_0^2 + v_0^2 + w_0^2)^{3/2}} \right) \} + \\
 & \quad + q_0 \{ z_q + m + z|q| \frac{|q_0|}{q_0} \delta s + (\eta_0 - 1) z_{q \eta} \} + \\
 & \quad + r_0 \{ z_{rr} r_0 \left( \frac{1}{\sqrt{u_0^2 + v_0^2 + w_0^2}} - \frac{u_0^2}{(u_0^2 + v_0^2 + w_0^2)^{3/2}} \right) \} + \\
 & \quad + \Delta v \left[ u_0 \left\{ \frac{(z_{vr} r_0 + z_{vp} p_0 + 2z_{vv} v_0)}{\sqrt{u_0^2 + v_0^2 + w_0^2}} \right. \right. \\
 & \quad \left. \left. - \frac{v_0 (z_{rr} r_0^2 + z_{pp} p_0^2 + z_{vp} r_0 p_0 + z_{vr} v_0 r_0 + z_{vp} v_0 p_0 + z_{vv} v_0^2)}{(u_0^2 + v_0^2 + w_0^2)^{3/2}} \right\} + \right.
 \end{aligned}$$

III. Normal Force (Cont.)

$$\begin{aligned}
 & + \Delta q \left[ u_0 \left\{ z_q + m + z \left| \frac{q}{q_0} \right| \delta s + \frac{q_0}{|q_0|} \delta s + (\eta_0 - 1) z_{q\eta} \right\} + \right. \\
 & \quad \left. + w_0 \left\{ z_w \left| \frac{q}{q_0} \right| \frac{\sqrt{v_0^2 + w_0^2}}{|w_0|} \frac{q_0}{|q_0|} \right\} + q_0^{2m} x_G - r_0^{my} G + \frac{\partial Z_{CRFW}}{\partial q} \right]^* + \\
 & + \Delta r \left[ u_0 \left\{ \frac{1}{\sqrt{u_0^2 + v_0^2 + w_0^2}} (2z_{rr} r_0 + z_{rp} p_0 + z_{vr} v_0) \right\} \right. \\
 & \quad \left. - p_0^{mx} G - q_0^{my} G + \frac{\partial Z_{CRFW}}{\partial r} \right]^* + \\
 & + \Delta \phi \left[ -(WTOT - B) \cos \theta_0 \sin \phi_0 \right] \\
 & + \Delta \theta \left[ -(WTOT - B) \sin \theta_0 \cos \phi_0 \right] \\
 & + \Delta \delta s \left[ (z_{\delta s} + (\eta_0 - 1) z_{\delta s \eta}) u_0^2 + z \left| \frac{q}{q_0} \right| \delta s \left| \frac{u_0}{q_0} \right| \right] + \\
 & + \Delta \delta b \left[ z_{\delta b} u_0^2 \right] + \\
 & + \Delta n \left[ z_{q\eta} u_0 q_0 + z_{w\eta} u_0 w_0 + z_w \left| \frac{q}{q_0} \right| \eta w_0 \frac{\sqrt{v_0^2 + w_0^2}}{|w_0|} + z_{\delta s \eta} u_0^2 \delta s_0 \right]
 \end{aligned}$$

where:

$$\frac{\partial Z_{CRFW}}{\partial v} \Big|^* = \frac{\rho}{2} \left( -l^2 \frac{z_{vw}}{\int_l D(x) dx} \right) \int_l D(x) \frac{w_0(x) v_0(x)}{\sqrt{v_0^2(x) + w_0^2(x)}} dx$$

$$\frac{\partial Z_{CRFW}}{\partial w} \Big|^* = \frac{\rho}{2} \left( -l^2 \frac{z_{ww}}{\int_l D(x) dx} \right) \int_l D(x) \frac{(v_0^2(x) + 2w_0^2(x))}{\sqrt{v_0^2(x) + w_0^2(x)}} dx$$

$$\left. \frac{\partial Z_{CRFW}}{\partial q} \right|_* = \frac{\rho}{2} (l^2 \frac{z_{ww}}{\int_l D(x) dx}) \int_l x D(x) \frac{(v_0^2(x) + 2w_0^2(x))}{\sqrt{v_0^2(x) + w_0^2(x)}} dx$$

$$\left. \frac{\partial Z_{CRFW}}{\partial r} \right|_* = \frac{\rho}{2} (-l^2 \frac{z_{ww}}{\int_l D(x) dx}) \int_l x \frac{D(x) w_0(x) v_0(x)}{\sqrt{v_0^2(x) + w_0^2(x)}} dx$$

#### IV. Rolling Torque

$$\begin{aligned} & -[mz_G + K_v \Delta \dot{v} + my_G \Delta \dot{w} + [I_x - K_p] \Delta \dot{p} - I_{xy} \Delta \dot{q} - [I_{xz} + K_r] \Delta \dot{r} = \\ & \Delta u [2u_0 \{K^* + K_{\delta r} \delta r_0 + (\eta_0 - 1) K_{*n} + \\ & + \beta_{t0}^2 (K_{4t} \sin 4\phi_{t0} + K_{8t} \sin 8\phi_{t0})\} + \\ & + v_0 \{K_v - 2\beta_{t0} \sqrt{\frac{v_{t0}^2}{v_0^2} + \frac{w_{t0}^2}{v_0^2}} \cdot (K_{4t} \sin 4\phi_{t0} + K_{8t} \sin 8\phi_{t0})\} + \\ & + p_0 K_p + q_0 my_G + r_0 mz_G + M_0 z_G + K_r) r_0 \\ & + \Delta v [u_0 \left\{ \frac{2v_0 \beta_{t0}}{\sqrt{v_{t0}^2 + w_{t0}^2}} \cdot (K_{4t} \sin 4\phi_{t0} + K_{8t} \sin 8\phi_{t0}) + \frac{u_0 \beta_{t0}^2 w_{t0}}{v_{t0}^2 + w_{t0}^2} \cdot \right. \\ & \left. (4K_{4t} \sin 4\phi_{t0} + 8K_{8t} \sin \phi_{t0}) + K_v \right\} + v_0 \{K_v |v| \left( \sqrt{1 + \frac{w_0^2}{v_0^2}} + \frac{v_0}{\sqrt{v_0^2 + w_0^2}} \right)\} + \\ & + \beta_{t0}^2 \{ (K_{4t} \sin 4\phi_{t0} + K_{8t} \sin 8\phi_{t0}) 2v_{t0} + \\ & + w_{t0} (4K_{4t} \cos 4\phi_{t0} + K_{8t} 8 \cos \phi_{t0}) \} + \\ & + w_0 K_{uw} - p_0 my_G + K_{vq} q_0] + \end{aligned}$$

IV. Rolling Torque (Cont.)

$$\begin{aligned}
 & + \Delta w \left[ u_0 \left\{ \frac{2w_{t0} \beta_{t0}}{v_{t0}^2 + w_{t0}^2} (K_{4t} \sin 4\phi_{t0} + K_{8t} \sin 8\phi_{t0}) \right. \right. \\
 & \quad \left. \left. - \frac{u_0 \beta_{t0}^2 v_{t0}}{v_{t0}^2 + w_{t0}^2} (4K_{4t} \cos 4\phi_{t0} + 8K_{8t} \cos 8\phi_{t0}) \right\} \right. \\
 & \quad + v_0 \left\{ K_{vw} + \frac{K_v |v| w_0}{\sqrt{v_0^2 + w_0^2}} \right\} + \\
 & \quad + \beta_{t0}^2 \{ 2w_{t0} (K_{4t} \sin 4\phi_{t0} + K_{8t} \sin 8\phi_{t0}) \\
 & \quad - v_{t0} (4K_{4t} \cos 4\phi_{t0} + 8K_{8t} \cos 8\phi_{t0}) \} + \\
 & \quad + p_0 (K_{wp} - m z_G) + r_0 K_{wr} \} + \\
 & + \Delta p \{ u_0 k_p - v_0 m y_G + w_0 \{ k_{wp} - m z_G \} + 2k_p |p| |p_0| + \\
 & \quad + q_0 (I_{yz} + K_{pq}) - r_0 I_{xy} \} + \\
 & + \Delta q \left[ u_0 \{ m y_G - \left( \frac{2w_0 \beta_{t0} x_{t0} v_{t0}}{\sqrt{v_{t0}^2 + w_{t0}^2}} + 2w_{t0} \beta_{t0}^2 \right) \right. \\
 & \quad \left. (K_{4t} \sin 4\phi_{t0} + K_{8t} \sin 8\phi_{t0}) + \right. \\
 & \quad \left. + \frac{4u_0 v_{t0} x_{t0}}{v_{t0}^2 + w_{t0}^2} (K_{4t} \cos 4\phi_{t0} + K_{8t} 2 \cos 8\phi_{t0}) \right\} + \\
 & \quad + v_0 \{ K_{vq} \} + p_0 \{ I_{yz} + K_{pq} \} - q_0 2I_{yz} + r_0 \{ (I_y - I_z) + \\
 & \quad + K_{qr} + 4\beta_{t0}^2 v_{t0} x_{t0} (K_{4t} \cos 4\phi_{t0} + K_{8t} 2 \cos 8\phi_{t0}) \} +
 \end{aligned}$$

IV. Rolling Torque (Cont.)

$$\begin{aligned}
 & + \Delta r \left[ u_0 \left\{ m z_G + K_r + \frac{2\beta v_{t0}^2 x_{t0}}{\sqrt{v_{t0}^2 + w_{t0}^2}} (k_{4t} \sin 4\phi_{t0} + k_{8t} \sin 8\phi_{t0}) + \right. \right. \\
 & \quad + \frac{u_0 \beta^2 v_{t0}^2 x_{t0}}{\sqrt{v_{t0}^2 + w_{t0}^2}} (4K_{4t} \phi_{t0} + 8K_{8t} \cos 8\phi_{t0}) \left. \right\} + w_0 K_{wz} - P_0 I_{xy} + \\
 & \quad + q_0 \left\{ (I_y - I_z) + K_{qr} \right\} - r_0 2I_{yz} + \\
 & \quad + 2v_{t0} x_{t0} \beta^2 (K_{8t} \sin 4\phi_{t0} + K_{8t} \sin 8\phi_{t0}) \\
 & \quad + \beta^2 v_{t0}^2 x_{t0}^2 (4K_{4t} \cos 4\phi_{t0} + 8K_{8t} \cos 8\phi_{t0}) \left. \right] \\
 & + \Delta \phi \left[ -(y_G^{WTOT} - y_B) \cos \theta_0 \sin \phi_0 - (z_G^{WTOT} - z_B) \cos \phi_0 \cos \theta_0 \right] + \\
 & + \Delta \theta \left[ (z_G^{WTOT} - z_B) \sin \theta_0 \sin \phi_0 - (y_G^{WTOT} - y_B) \sin \theta_0 \cos \phi_0 \right] + \\
 & + \Delta \delta r \left[ K_{\delta r} u_0^2 \right] \\
 & + \Delta \eta \left[ K_{\eta} u_0^2 \right]
 \end{aligned}$$

V. Pitching Torque

$$\begin{aligned}
 m\dot{x}_G \Delta \dot{u} - (m\dot{x}_G + M_w) \Delta \dot{w} - I_{xy} \Delta \dot{p} + (I_y - M_q) \Delta \dot{q} - I_{yz} \Delta \dot{r} \\
 = \Delta u [ 2u \{ M^* + M_{\delta s} \delta s_0 + M_{\delta b} \delta b_0 + (\eta_0 - 1) M_{\delta \eta} \delta \eta \} + \\
 + v_0 \{ (M_{vr} r_0 + M_{vp} p_0) + M_{vv} v_0 \} \left\{ \frac{v_0^2 + w_0^2}{u_0^2 + v_0^2 + w_0^2} \right\}^{3/2} \\
 + w_0 \{ M_w + M_w \frac{|w_0|}{w_0} + (\eta_0 - 1) M_{w\eta} \} + \\
 + p_0 \{ M_{pp} p_0 + M_{rp} r_0 \} \left\{ \frac{v_0^2 + w_0^2}{u_0^2 + v_0^2 + w_0^2} \right\}^{3/2} \\
 + q_0 \{ M_q - m\dot{x}_G + M_q \frac{|q_0|}{q_0} \delta s_0 + (\eta_0 - 1) M_{q\eta} \} + \\
 + \frac{r_0 M_{rr} r_0 (v_0^2 + w_0^2)}{(u_0^2 + v_0^2 + w_0^2)^{3/2}} ] \\
 + \Delta v \left[ \frac{u_0}{(u_0^2 + v_0^2 + w_0^2)^{3/2}} \{ M_{vv} (2v_0(u_0^2 + w_0^2) + v_0^3) \right. \\
 - v_0 (M_{rr} r_0^2 + M_{pp} p_0^2 + M_{vr} r_0 v_0 + M_{vp} v_0 p_0 + M_{rp} r_0 p_0) \} + \\
 + \frac{u_0}{\sqrt{u_0^2 + v_0^2 + w_0^2}} (M_{rr} r_0 + M_{vp} p_0 + M_{vr} r_0) + \\
 + \frac{v_0}{\sqrt{v_0^2 + w_0^2}} \{ M_w |q_0| + M_w |w_0| + M_{ww} |w_0| + \\
 \left. + (\eta_0 - 1) M_{w\eta} w_0 \} + p_0 m\dot{x}_G + r_0 m\dot{z}_G + \frac{\partial M_{CRFW}}{\partial v} \right] +
 \end{aligned}$$

V. Pitching Torque (Cont.)

$$\begin{aligned}
 & + \Delta w \left[ u_0 \left\{ \frac{-w_0}{(u_0^2 + v_0^2 + w_0^2)^{3/2}} \cdot \right. \right. \\
 & \quad (M_{pp} p_0^2 + M_{rr} r_0^2 + M_{vr} v_0 r_0 + M_{vp} v_0 p_0 + M_{rp} r_0 p_0 + M_{vv} v_0^2) \\
 & \quad + M_w + M_w \left| \frac{w_0}{|w_0|} \right| + (\eta_0 - 1) M_{wn} \left. \right\} + \frac{w_0}{\sqrt{v_0^2 + w_0^2}} \cdot \\
 & \quad \left\{ M_w \left| \frac{q_0}{|q_0|} \right| + M_w \left| \frac{(2w_0^2 + v_0^2)}{w_0} \right| + M_{ww} \frac{(2w_0^2 + v_0^2)}{|w_0|} + \right. \\
 & \quad \left. + (\eta_0 - 1) M_w \left| \frac{(2w_0^2 + v_0^2)}{w_0} \right| \right\} - m z_G q_0 + \left. \frac{\partial M_{CRFW}}{\partial w} \right] + \\
 & + \Delta p \left[ \frac{u_0}{\sqrt{u_0^2 + v_0^2 + w_0^2}} (2M_{pp} p_0 + M_{vp} v_0 + M_{rp} r_0) + m x_G v_0 \right. \\
 & \quad \left. - 2p_0 I_{zx} - q_0 I_{zy} + (I_z - I_x + M_{rp}) r_0 \right] + \\
 & + \Delta q \left[ u_0 \left\{ M_q - m x_G + (\eta_0 - 1) M_{qn} + M_q \left| \frac{q_0}{|q_0|} \right| \delta_{sq} \right\} + \right. \\
 & \quad + v_0 M_w \left| \frac{q_0}{|q_0|} \right| \sqrt{1 + \frac{w_0^2}{v_0^2}} - m z_G w_0 - I_{yz} p_0 + 2M_q \left| \frac{q_0}{|q_0|} \right| |q_0| + \\
 & \quad \left. + I_{xy} r_0 + \frac{\partial M_{CRFW}}{\partial q} \right] + \\
 & + \Delta r \left[ \frac{u_0}{\sqrt{u_0^2 + v_0^2 + w_0^2}} (M_{vr} v_0 + M_{rp} r_0 + 2M_{rr} r_0) + m z_G v_0 + \right. \\
 & \quad \left. + p_0 (I_z - I_x + M_{rp}) + I_{xy} q_0 + 2I_{xz} r_0 + \frac{\partial M_{CRFW}}{\partial r} \right] +
 \end{aligned}$$

V. Pitching Torque (Cont.)

$$\begin{aligned}
 & + \Delta \phi [-(x_G^{WTOT} - x_B) \cos \theta_0 \sin \phi_0] + \\
 & + \Delta \theta [(x_G^W - x_B) \sin \theta_0 \cos \phi_0 - (z_G^{WTOT} - z_B) \cos \theta_0] + \\
 & + \Delta \delta s [M_{\delta s} + M_{\delta s n} (\eta_0 - 1) u_0^2 + M_{|q|} |\delta s u_0| |q_0|] + \\
 & + \Delta \delta b [M_{\delta b} u_0^2] \\
 & + \Delta \eta [M_{q\eta} u_0 q_0 + M_{w\eta} u_0 w_0 + M_{w|w|} |w_0| \sqrt{v_0^2 + w_0^2} + \\
 & \quad + M_{\delta s n} u_0^2 \delta s_0]
 \end{aligned}$$

$$\text{Where: } \left. \frac{\partial M_{CRFW}}{\partial v} \right|_* = \frac{\rho}{2} \left( l^2 \frac{z_{ww}}{\int_l D(x) dx} \right) \int_l x \frac{D(x) w_0(x) v_0(x)}{\sqrt{v_0^2(x) + w_0^2(x)}} dx$$

$$\left. \frac{\partial M_{CRFW}}{\partial w} \right|_* = \frac{\rho}{2} \left( l^2 \frac{z_{ww}}{\int_l D(x) dx} \right) \int_l x D(x) \frac{(v_0^2(x) + 2w_0^2(x))}{\sqrt{v_0^2(x) + w_0^2(x)}} dx$$

$$\left. \frac{\partial M_{CRFW}}{\partial q} \right|_* = \frac{\rho}{2} \left( -l^2 \frac{z_{ww}}{\int_l D(x) dx} \right) \int_l x^2 D(x) \frac{(v_0^2(x) + 2w_0^2(x))}{\sqrt{v_0^2(x) + w_0^2(x)}} dx$$

$$\left. \frac{\partial M_{CRFW}}{\partial r} \right|_* = \frac{\rho}{2} \left( l^2 \frac{z_{ww}}{\int_l D(x) dx} \right) \int_l x^2 D(x) \frac{w_0(x) v_0(x)}{\sqrt{v_0^2(x) + w_0^2(x)}} dx$$

VI. Yawing Torque.

$$\begin{aligned}
 & -m y_G \Delta \dot{u} + (m x_G - N_v) \Delta \dot{v} - (I_{xx} + N_p) \Delta \dot{p} - I_{yz} \Delta \dot{q} + (I_z - N_r) \Delta \dot{r} \\
 & = \Delta u \left[ 2u_0 \left\{ N^* + (N_{\delta r} + (\eta_0 - 1) N_{\delta_{zn}}) \delta r_0 \right\} + \right. \\
 & + v_0 \left\{ N_v + N_{vw} \frac{w_0 (v_0^2 + w_0^2)}{(u_0^2 + v_0^2 + w_0^2)^{3/2}} + (\eta_0 - 1) N_{vn} \right\} + \\
 & + N_p p_0 + r_0 \left\{ N_r - m x_G + N |r| \delta r \frac{|r_0|}{r_0} \delta r_0 + (\eta_0 - 1) N_{zn} \right\} + \\
 & + \Delta v \left[ u_0 \left\{ N_v + N_{vw} \frac{w_0 (w_0^2 + u_0^2)}{(u_0^2 + v_0^2 + w_0^2)^{3/2}} + (\eta_0 - 1) N_{vn} \right\} \right. \\
 & + \frac{v_0}{\sqrt{v_0^2 + w_0^2}} \left\{ N |v| r r_0 + 2 N_v |v| v_0 + 2(\eta_0 - 1) N_v |v| \eta v_0 \right\} + \\
 & + \frac{w_0}{\sqrt{v_0^2 + w_0^2}} \left\{ N_v |v| w_0 + (\eta_0 - 1) N_v |v| \eta w_0 \right\} + \\
 & + N_{vq} q_0 - m y_G r_0 + \left. \frac{\partial N_{CRFW}}{\partial v} \right] + \\
 & + \Delta w \left[ u_0 N_{vw} \frac{v_0 (u_0^2 + v_0^2)}{(u_0^2 + v_0^2 + w_0^2)^{3/2}} + \frac{v_0}{\sqrt{v_0^2 + w_0^2}} \right. \\
 & \left. \left\{ N_v |v| w_0 + (\eta_0 - 1) N_v |v| \eta w_0 \right\} + \right. \\
 & + r_0 \left\{ N_{wr} + \frac{N |v| r w_0}{\sqrt{v_0^2 + w_0^2}} + m x_G p_0 + N_{wp} p_0 + m y_G q_0 + \left. \frac{\partial N_{CRFW}}{\partial w} \right] + \right.
 \end{aligned}$$

VI. Yawing Torque (Cont.)

$$\begin{aligned}
 & + \Delta p [N_p u_0 + w_0(mx_G + N_{wp}) + 2p_0 I_{xy} + q_0 \cdot \\
 & \quad (N_{pq} + I_x - I_y + my_G + N_{pq}) + I_{yz} r_0] + \\
 & + \Delta q [N_{vq} v_0 + my_G v_0 + (N_{pq} + I_x - I_y) p_0 \\
 & \quad - 2I_{xy} q_0 + r_0(N_{qr} - I_{zx}) + \frac{\partial N_{CRFW}}{\partial q} \Big|_*] + \\
 & + \Delta r [u_0 \{N_r - mx_G + N_{|r|} \delta r \frac{r_0}{|r_0|} \delta r_0 + (n_0 - 1) N_{rn}\} + \\
 & \quad + v_0 \{N_{|v|} \frac{v_0}{|v_0|} \left[ 1 + \frac{w_0^2}{v_0^2} - my_G \right] + N_{vr} w_0 + I_{yz} p_0 + \\
 & \quad + q_0 (N_{qr} - I_{zx}) + 2N_{r|r|} |r_0| + \frac{\partial N_{CRFW}}{\partial r} \Big|_*] \\
 & + \Delta \phi [(x_G^{WTOT} - x_B) \cos \theta_0 \cos \phi_0] + \\
 & + \Delta \theta [y_G^{WTOT} - y_B) \cos \theta_0 - (x_G^W - x_B) \sin \theta_0 \sin \phi_0] + \\
 & + \Delta \delta r [(N_{\delta r} + N_{\delta rn} (n_0 - 1)) u_0^2 + N_{|r|} \delta r u_0 |r_0|] + \\
 & + \Delta n [N_{rn} u_0 r_0 + N_{vn} u_0 v_0 + N_{|v|} \frac{v_0}{|v_0|} \sqrt{v_0^2 + w_0^2} + N_{\delta rn} u_0^2 \delta r_0]
 \end{aligned}$$

where:

$$\frac{\partial N_{CRFW}}{\partial v} \Big|_* = \frac{\rho}{2} (-l^2 \frac{Z_{ww}}{\int_l^l D(x) dx}) \int_l^l x H(x) \frac{(w_0^2(x) + 2v^2(x))}{\sqrt{v_0^2(x) + w_0^2(x)}} dx$$

$$\frac{\partial N_{CRFW}}{\partial w} \Big|_* = \frac{\rho}{2} (-l^2 \frac{Z_{ww}}{\int_l^l D(x) dx}) \int_l^l x H(x) \frac{v_0(x) w_0(x)}{\sqrt{v_0^2(x) + w_0^2(x)}} dx$$

$$\frac{\partial H_{CRFW}}{\partial q} \Big|_* = \frac{\rho}{2} (l^2 \int_l^2 \frac{z_{ww}}{D(x)} dx) \int_l^2 x^2 H(x) \frac{v_0(x) w_0(x)}{\sqrt{v_0^2(x) + w_0^2(x)}} dx$$

$$\frac{\partial H_{CRFW}}{\partial r} \Big|_* = \frac{\rho}{2} (-l^2 \int_l^2 \frac{z_{ww}}{D(x)} dx) \int_l^2 x^2 H(x) \frac{(w_0^2(x) + 2v^2(x))}{\sqrt{v_0^2(x) + w_0^2(x)}} dx$$

APPENDIX B

Table B-1. Nominal design point.

$u_0$ (FT/SEC)	$v_0$ (FT/SEC)	$w_0$ (FT/SEC)
47.380	2.270	0.5319
$P_0$ (RAD/SEC)	$q_0$ (RAD/SEC)	$r_0$ (RAD/SEC)
-.00003	0.00305	-.01829
$\delta s_0$ (DEG)	$\delta b_0$ (DEG)	$\delta r_0$ (DEG)
-.7350	0.0000	2.0000
$\text{PHI}_0$ (DEG)	$\text{THETA}_0$ (DEG)	
-9.4520	-0.08156	
RPS		
2.369		



Table B-4.  $\dot{\psi} - \dot{z}$  compensator matrices.

C MATRIX

0.00000E+00 0.00000E+00 0.00000E+00 -0.16421E+01 0.96642E+01 0.72573E-05 0.26394E-03 0.00000E+00 0.00000E+00 0.00000E+00 0.00000E+00 0.00000E+00  
 0.14213E-04 -0.14213E-02 0.96642E-02 0.00000E+00 0.00000E+00 0.00000E+00 0.23277E-01 -0.47180E+00 0.00000E+00 0.00000E+00 0.00000E+00 0.00000E+00

G MATRIX

-0.34501E-03 -0.35714E-02 -0.27943E-02 -0.10001E+00 -0.35947E+01 0.20793E+01 -0.10366E+00 -0.14267E+01 0.00718E-01 0.00718E-01 -0.79071E-01 0.00000E+00  
 0.21697E-02 0.00000E-02 0.00000E-02 0.10423E+00 0.21705E+01 -0.17743E+02 -0.94908E-01 -0.29333E+00 -0.54687E-01 0.67969E+00 -0.11497E+00 0.14444E+01

H MATRIX

0.63403E+00 0.58740E-01  
 -0.75699E+00 0.50452E-03  
 -0.41087E+00 -0.43310E+00  
 0.30501E-02 -0.39125E-02  
 -0.27912E-02 -0.14745E-02  
 0.74041E-02 -0.18905E-03  
 0.49950E-01 0.15734E-01  
 -0.44762E-02 -0.10222E+00  
 0.14097E-01 0.99366E-02  
 -0.28040E-01 -0.53104E-03  
 2.14433E-01 0.95615E-02  
 -0.27821E-01 -0.26534E-03

APPENDIX C

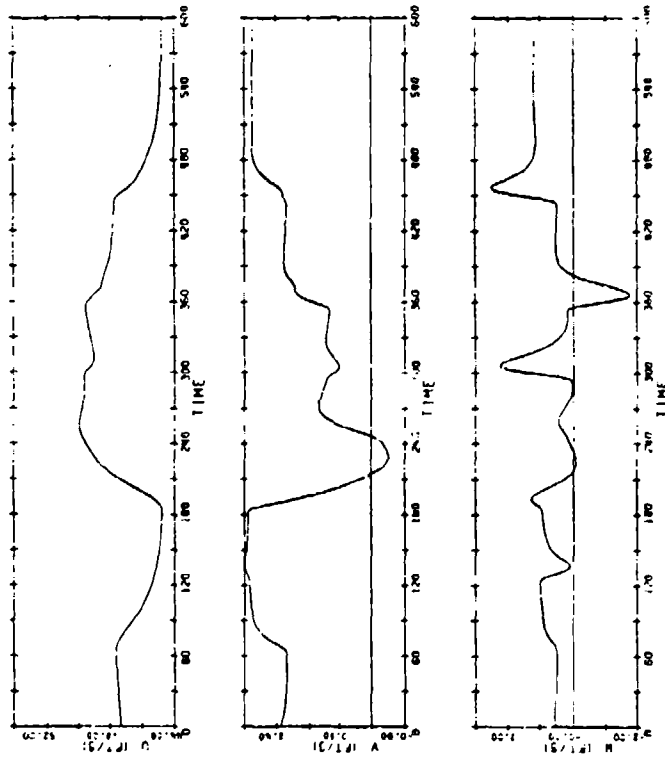
C-1. Nonlinear Simulation of  $\dot{\psi} - \dot{z}$  Compensator for  
Various Commanded Inputs

(The simulation in this appendix is based on the following table of command inputs for heading rate, in units of "tens" of degrees, and depth rate, in units of 0.01 \* feet/s).

Time	PSIDOT	Z DOT
0.	-10.000	0.0
60.	-10.000	0.0
65.	-15.000	0.0
120.	-15.000	0.0
125.	-15.000	0.05
180.	-15.000	0.05
185.	0.000	0.0
240.	0.000	0.0
245.	-5.000	0.0
290.	-5.000	0.0
295.	-5.000	-.1
350.	-5.000	-.1
355.	-10.000	0.0
440.	-10.000	0.0
445.	-15.000	-.1
600.	-15.000	-.1

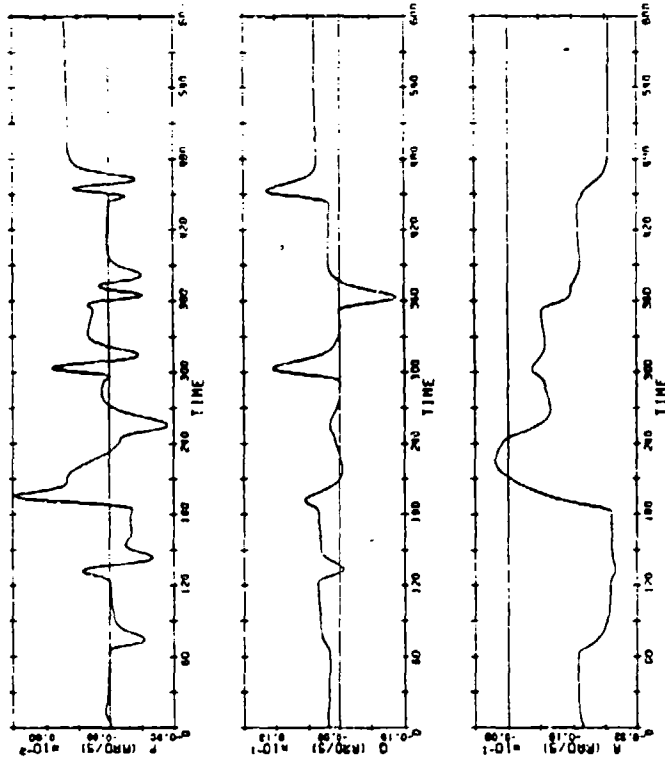
VELOCITIES

NON-LINEAR SIMULATION Z-PSI



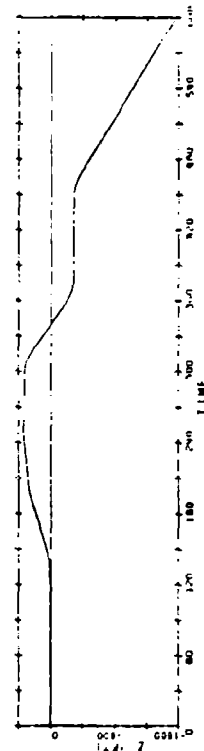
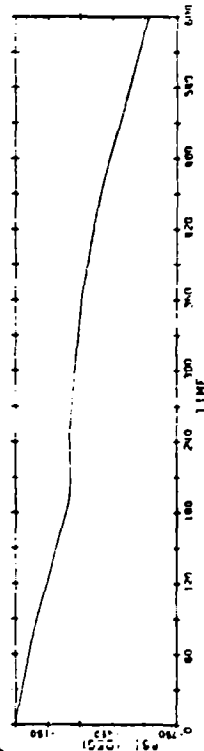
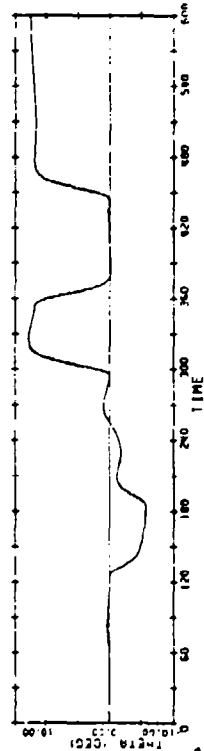
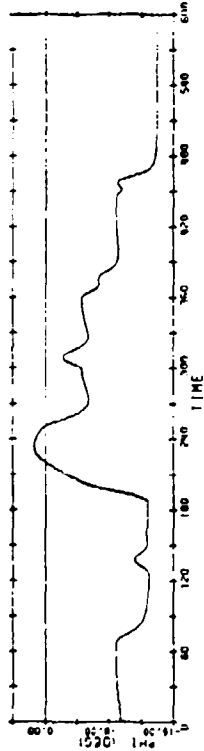
ANGULAR VELOCITIES

NON-LINEAR SIMULATION Z-PSI



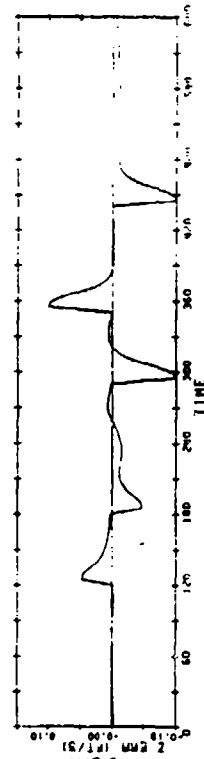
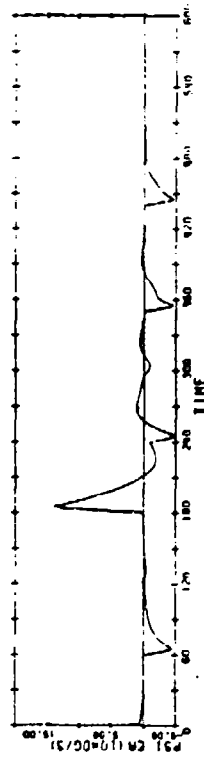
### ATTITUDE AND DEPTH

NON-LINEAR SIMULATION Z-PSI



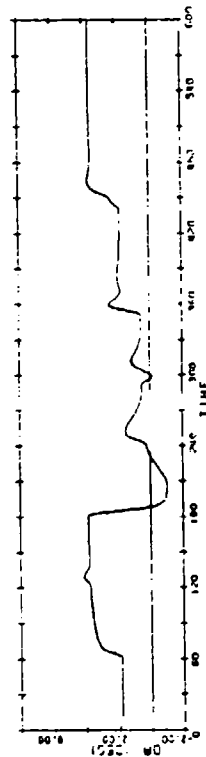
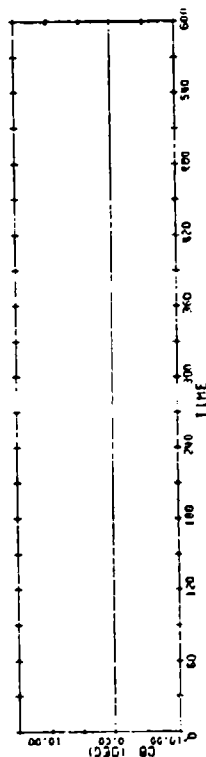
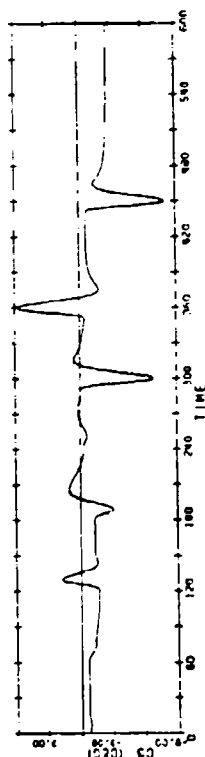
### OUTPUT ERROR

NON-LINEAR SIMULATION Z-PSI



# CONTROL INPUTS

NON-LINEAR SIMULATION Z-PSI



Appendix C (Cont.)